Near wall fibre orientation in flowing suspensions

by

Allan Carlsson

March 2009 Technical Reports from Royal Institute of Technology KTH Mechanics SE - 100 44 Stockholm, Sweden Akademisk avhandling som med tillstånd av Kungliga Tekniska Högskolan i Stockholm framlägges till offentlig granskning för avläggande av teknologie doktorsexamen fredagen den 27 mars 2009 kl 10.15 i E2, Lindstedsvägen 3, KTH, Stockholm.

©Allan Carlsson 2009
Universitetsservice US-AB, Stockholm 2009

Near wall fibre orientation in flowing suspensions

Allan Carlsson 2009

Linné FLOW Centre KTH Mechanics SE - 100 44 Stockholm, Sweden

Abstract

This thesis deals with fibre orientation in wall-bounded shear flows. The primary application in mind is papermaking. The study is mainly experimental, but is complemented with theoretical considerations.

The main part of the thesis concerns the orientation of slowly settling fibres in a wall-bounded viscous shear flow. This is a flow case not dealt with previously even at small Reynolds numbers. Experiments were conducted using dilute suspensions with fibres having aspect ratios of $r_p \approx 7$ and 30. It is found that the wall effect on the orientation is small for distances from the wall where the fibre centre is located farther than half a fibre length from the wall. Far from the wall most fibres were oriented close to the flow direction. Closer to the wall than half a fibre length the orientation distribution first shifted to be more isotropic and in the very proximity of the wall the fibres were oriented close to perpendicular to the flow direction, nearly aligned with the vorticity axis. This was most evident for the shorter fibres with $r_p \approx 7$.

Due to the density difference between the fibres and the fluid there is an increased concentration near the wall. Still, a physical mechanism is required in order for a fibre initially oriented close to the flow direction at about half a fibre length from the wall to change its orientation to aligned with the vorticity axis once it has settled down to the wall. A slender body approach is used in order to estimate the effect of wall reflection and repeated wall contacts on the fibre rotation. It is found that the both a wall reflection, due to settling towards the wall, and contact between the fibre end and the wall are expected to rotate the fibre closer to the vorticity axis. A qualitative agreement with the experimental results is found in a numerical study based on the theoretical estimation.

In addition an experimental study on fibre orientation in the boundary layers of a headbox is reported. The orientation distribution in planes parallel to the wall is studied. The distribution is found to be more anisotropic closer to the wall, *i.e.* the fibres tend to be oriented closer to the flow direction near the wall. This trend is observed sufficiently far upstream in the headbox. Farther downstream no significant change in the orientation distribution could be detected for different distances from the wall.

Descriptors: fluid mechanics, fibre orientation, shear flow, wall effect, fibre suspension, papermaking

Preface

This doctoral thesis in mechanics deals with near wall fibre orientation in flowing suspensions. The primary application in mind is manufacturing of paper, where a fibre suspension flows along solid surfaces in the early stage of the process. The thesis is divided into two parts. Part I provides a brief introduction to papermaking as well as an overview of relevant work performed in the area of fibre orientation. Part II consists of five papers that, for consistency, have been adjusted to the format of the thesis.

February 2009, Stockholm

Allan Carlsson

Contents

Abstract	iii		
Preface	iv		
Part I. Overview and summary			
Chapter 1. Introduction	1		
1.1. Paper manufacturing	1		
1.2. Fibre orientation	2		
Chapter 2. Fibre orientation in flowing suspensions	5		
2.1. Fluid motion	5		
2.2. Fibre suspension flows	6		
Chapter 3. Slowly settling fibres in a wall-bounded shear flow	23		
3.1. Experimental setup and flow situation	23		
3.2. Results & discussion	24		
Chapter 4. Near wall fibre orientation in a headbox	31		
4.1. Experimental procedure and flow situation	31		
4.2. Fibre orientation in boundary layer	32		
Chapter 5. Concluding remarks	35		
Chapter 6. Papers and authors contributions	37		
Appendix A. Formation of fibres in streamwise streaks	39		
Acknowledgements			
References	44		

Part II. Papers

1.	Fiber orientation control related to papermaking	55
2.	Orientation of slowly sedimenting fibers in a flowing suspension near a plane wall	n 83
3.	Orbit drift of a slowly settling fibre in a wall-bounded shear flow	109
4.	Fibre orientation near a wall of a headbox	133
5.	Evaluation of a steerable filter for detection of fibres in flowing suspensions	151

Part I Overview and summary

CHAPTER 1

Introduction

This thesis focuses on near wall orientation of fibres in flowing suspensions. Flowing fibre suspensions are present in various applications. The primary application in mind for this work is paper production. The study is mainly experimental in nature, but is also complemented with theoretical considerations. Below a brief background is given to the process of papermaking and the relevance of fibre orientation. The primary sources for the text in this chapter is Fellers & Norman (1998) and Gavelin (1990).

1.1. Paper manufacturing

The ability to produce paper has its origin in China, where paper was manufactured roughly 2000 years ago. Originally all paper sheets were made by hand in a slow process, whereas today there are machines that produce more than 600,000 tons/year. Although paper as a product has been around for several centuries, many of the physical mechanisms present in the manufacturing process are not well understood. Thus, the prospects of improving the process are still promising.

Paper consists of a network of fibres, where the most commonly used fibres in manufacturing are cellulose fibres from wood. To produce paper the first step is to extract fibres from wood to produce pulp. This is done in a pulping process and can be done in several ways. How the pulp is prepared depends on the desired properties of the final paper. The fibre suspension, that enters the initial part of the paper machine called a headbox, consists of a mixture of water and cellulose fibres. The mass fraction of fibres are usually less than 1% and the suspension can also contain some fine material, so called fillers such as clay or chalk and chemical additives.

The main assignment of the headbox is to transform a pipe flow, with a diameter of about 800 mm, to a uniform free jet around 10 mm thick and up to 10 m wide. The jet leaving the headbox impinges on one or two permeable bands called wires. The headbox, jet and initial drainage of water through the wires are often referred to as the forming section of the paper machine. A schematic of the forming section is shown in figure 1.1. The forming section is followed by large machinery consisting of a press section and a drying section.

1

2 1. INTRODUCTION

The primary aim of the press and drying section is to remove the remainder of water from the suspension to generate the thin network of fibres called paper.

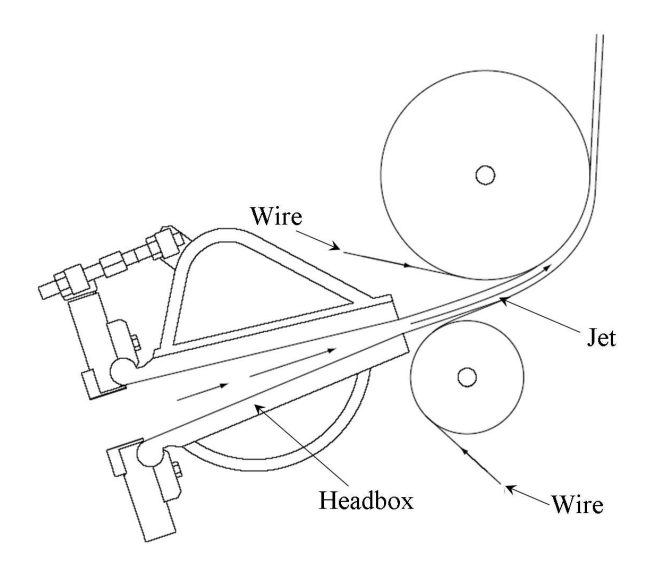


FIGURE 1.1. Schematic of a forming section of a paper machine.

1.2. Fibre orientation

A parameter of relevance for the final properties of a paper sheet is the fibre orientation. The fibres in the final product are to a large extent oriented in the machine direction. This leads to a stronger tensile strength in the machine direction, than in the cross direction. However, the desired orientation distribution varies with the type of paper produced. Generally it is not desired that the orientation distribution changes over the plane of the paper sheet or over the thickness of the paper. When a fibre dries it changes its dimension and shrinks more radially than axially. This leads to internal stresses in the paper that result in deformations and undesired properties of the paper. For instance, if there is a variation in orientation distribution over the thickness of the paper this can make the paper curl or twist which can lead to problems such as paper jams in copy machines and printers. There are also other issues where the fibre orientation is of significance. In a recent overview Odell & Pakarinen (2001) made a more thorough overview on fibre orientation related defects on different scales and their effect on the paper sheet.

The orientation distribution of the final paper sheet is determined in the forming section of the paper. Shortly after the free jet impinges on the wire,

water is drained and the fibre concentration of the suspension is rapidly increased. Quickly, the fibres form a network and as a result they cannot alter their orientation in relation to each other. In order to be able to control the fibre orientation in the final paper sheet it is therefore essential to understand how the fibres interact with the fluid and surroundings in this early part of the paper machine.

As stated earlier the study of near wall fibre orientation in shear flows is the main theme of this thesis. In a headbox nozzle, which may be described as a planar convergent channel, there are often a set of thin flexible flow dividers implemented. The flow dividers will here be referred to as lamellas. A reason for implementing lamellas is that such devices can reduce large scale fluctuations in the flow, which could lead to an uneven mass distribution of fibres in the final paper sheet, i.e. a poor formation. At the interface between the suspension and the solid surfaces of the lamellas the velocity of the fluid is zero. This leads to a formation of thin layers of shear along the surfaces of the lamellas, where the velocity rapidly increases with the distance to the solid surface. The fluid mechanical term for these layers of shear is boundary layers. The boundary layer thickness, i.e. the thickness of the sheared region of fluid, in the headbox is of the order of 1 mm. Recall that the thickness of the jet leaving the headbox is about 10 mm and due to the lamellas there can be several boundary layers in the headbox. Therefore, the lamellas may have a significant impact on the orientation distribution of fibres leaving the headbox in the outgoing jet and also on the orientation distribution in the final paper.

This work mainly deals with a different parameter regime than that operated at in a paper machine. Experiments have been performed in a viscous wall-bounded shear flow, where the inertial effects are expected to be considerably smaller than in the boundary layers of a headbox. This has been done in order to develop an experimental methodology to measure the orientation and velocity of fibres in flowing suspensions. Also, this is a flow case which is still not fully understood even when inertial effects are absent.

4 1. INTRODUCTION

CHAPTER 2

Fibre orientation in flowing suspensions

In this chapter an introduction is given to the field of fibre suspension flows. Extensive work has been performed in this and related areas. Particular emphasis is given to the motion of fibres in shear flows.

2.1. Fluid motion

The motion of an incompressible Newtonian fluid is described by Navier-Stokes equations

$$\frac{\partial \mathbf{u}}{\partial t} + (\mathbf{u} \cdot \nabla)\mathbf{u} = -\frac{1}{\rho}\nabla p + \nu \nabla^2 \mathbf{u} + \mathbf{f}$$
 (2.1)

$$\nabla \cdot \mathbf{u} = 0, \tag{2.2}$$

where ${\bf u}$ is the fluid velocity, t is the time, p is the pressure and ${\bf f}$ is a body force term. The fluid properties, density and kinematic viscosity, is denoted by ρ and ν , respectively. In order to get an indication of the characteristics of a flow a non-dimensional number, referred to as the Reynolds number $Re = UL/\nu$, is often introduced. The parameters U and L correspond to a characteristic velocity and length scale, respectively, for the particular flow. For steady flows where the inertial effects are negligible as compared to effects of viscosity, *i.e.* Re << 1, equation (2.1) is reduced to

$$\frac{1}{\rho}\nabla p = \nu\nabla^2\mathbf{u} + \mathbf{f}.\tag{2.3}$$

Flows that are described by equation (2.3) are generally called Stokes flows or creeping flows. It is worth noticing that equation (2.3) is linear. This implies that Stokes flows have a couple of specific features worth mentioning:

- Stokes flows are reversible. If p, \mathbf{u} form a solution to equation (2.3) then -p, $-\mathbf{u}$ is a also solution, provided that the motion of all boundaries and the body force term are reversed.
- It is possible to apply the principle of linear superposition and superimpose flows that satisfy equation (2.3).

These features are not shared with Navier-Stokes equations since the non-linear term $(\mathbf{u} \cdot \nabla)\mathbf{u}$ in equation (2.1) does not change sign with \mathbf{u} .

2.2. Fibre suspension flows

We will now consider flows where fibres, i.e. rod-like particles, are suspended in a fluid. Although extensive work have been done in the field of fibre suspension flows there are still issues that remain to be solved. This is the case even for fundamental flows such as sedimentation of fibre suspensions, e.g. Koch & Shaqfeh (1989), Mackaplow & Shaqfeh (1998) and Herzhaft & Guazzelli (1999). The origin to the difficulties is partly that the motion of a fibre is orientation dependent. A sedimenting fibre, which is oriented obliquely to gravity, will for instance have a non-zero velocity component in the direction perpendicular to gravity. Another factor contributing to the complexity of fibre suspensions, is that the velocity disturbance of the fluid due to the presence of a fibre decays slowly. Unless the suspension is very dilute, this results in long-range hydrodynamical interactions between multiple fibres.

The main interest here is the fibre motion and orientation in wall-bounded shear flows. It was mentioned in the preceding chapter that the properties of a manufactured paper depends on the fibre orientation. Knowledge about fibre orientation in flowing suspensions is also crucial in order to understand the bulk flow of the suspension. The Navier-Stokes equations mentioned above are only valid for Newtonian fluids where the shear stress of the fluid is linearly proportional to the rate-of-strain. When fibres or other particles are suspended in a fluid this relation is in general not true, for the mixture as a whole, even though the fluid phase is Newtonian. The study of non-Newtonian fluids is termed rheology. The coupling between the fibre orientation and the rheological properties of the suspension will not be considered in this study. There are a number of reviews on the rheology of fibre suspensions, e.g. Powell (1991), Zirnsak, Hur & Boger (1994) and Petrie (1999).

Another restriction in this work is that the effect of Brownian diffusion is considered to be negligible. Brownian motion is particularly significant for suspensions with very small particles. It is convenient to introduce a rotary Péclet number $Pe = G/D_r$ to to determine whether Brownian motion is significant or not, see for instance Brenner (1974). In the expression G is a characteristic rate-of-strain or shear rate of the fluid and D_r is a rotary diffusivity coefficient dependent on the temperature, viscosity and particle parameters. For the flow conditions in a headbox Pe >> 1 and Brownian diffusion is negligible.

2.2.1. Unbounded shear flows

Jeffery (1922) derived the governing equations of motion for an isolated ellipsoid, with a surface defined by $x'^2/a^2 + y'^2/b^2 + z'^2/c^2 = 1$, suspended in a linear flow field. It was assumed that all inertial effects are negligible, that the particle is non-sedimenting and that the fluid is Newtonian. The situation for a shear flow given by $\mathbf{u} = \dot{\gamma} y \mathbf{e_x}$, where $\dot{\gamma}$ is the shear rate is illustrated in figure 2.1. For the case when b = c, *i.e.* a spheroid, the equations for the rotation

rate are

$$\dot{\phi} = -\frac{\dot{\gamma}}{r_e^2 + 1} (r_e^2 \sin^2 \phi + \cos^2 \phi) \tag{2.4}$$

$$\dot{\theta} = \left(\frac{r_e^2 - 1}{r_e^2 + 1}\right) \frac{\dot{\gamma}}{4} \sin 2\phi \sin 2\theta, \tag{2.5}$$

where $r_e = a/b$ is the ellipsoidal aspect ratio, θ is the polar angle between the vorticity axis z and the major axis of the spheroid x' and ϕ is the dihedral angle between the xz-plane and the x'z-plane. In the remainder of this text, when referring to the orientation of a spheroid or another elongated particle, the major axis is implied. Equations (2.4) and (2.5) are valid for both prolate spheroids $(r_e > 1)$ and oblate spheroids $(r_e < 1)$, but since the main focus of this study concerns fibres only the motion of prolate spheroids will be considered.

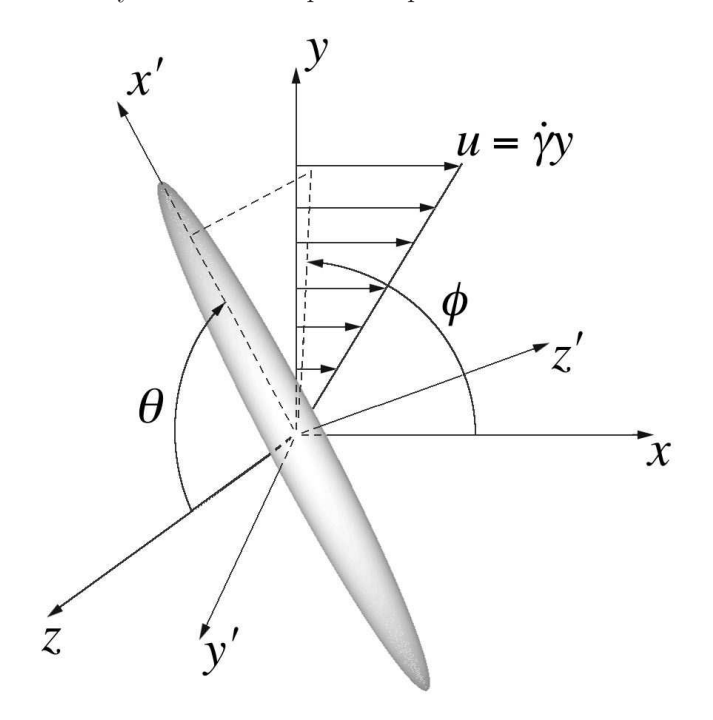


FIGURE 2.1. Coordinate system for elongated particle suspended in a shear flow.

From the equations it is clear that $\dot{\phi}$ and $\dot{\theta}$ are both linearly dependent on $\dot{\gamma}$. The rotation is periodic with a period given by

$$T = \frac{2\pi}{\dot{\gamma}} \left(\frac{r_e^2 + 1}{r_e} \right). \tag{2.6}$$

Equations (2.4) and (2.5) can be integrated with respect to time, which gives that

$$\cot \phi = -r_e \cot \left(\frac{2\pi t}{T} + \phi_0\right) \tag{2.7}$$

$$\cot \phi = -r_e \cot \left(\frac{2\pi t}{T} + \phi_0\right)$$

$$\tan \theta = \frac{Cr_e}{(r_e^2 \sin^2 \phi + \cos^2 \phi)^{1/2}},$$
(2.7)

where C is the orbit constant and ϕ_0 is the phase angle, both determined by the initial conditions. It is worth noticing that ϕ is independent of C. During rotation the end points of the spheroid form closed orbits in space. These are usually referred to as Jeffery orbits. A number of possible orbits, illustrated in the xy-plane, are shown in figure 2.2, for $r_e = 40$. The position of the fibre end point is normalized with the fibre length l.

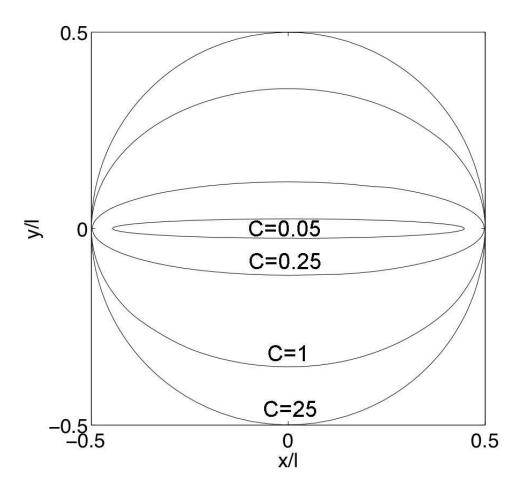


FIGURE 2.2. Different Jeffery orbits formed by the end points of a rotating spheroid with $r_e = 40$.

The fibre will spend most of its time nearly aligned with the xz-plane. With regular intervals of T/2 the spheroid rapidly flips around the vorticity axis. As $C \to \infty$ the spheroid will be oriented in the xy-plane as it undergoes this flipping motion. For $C = O(1/r_e)$ the spheroid still flips, although the angle to the xy-plane is never large during any phase of the orbit. For C=0the spheroid spins around its own major axis aligned with the vorticity axis, with a constant angular velocity $\dot{\gamma}/2$.

Bretherton (1962) extended Jeffery's analysis to be valid for almost any body of revolution, with a fore-aft symmetry. As a result equations (2.4– 2.8) are valid also for fibres of cylindrical shape, provided that an equivalent ellipsoidal axis ratio is found.

A fibre rotating according to Jeffery's equations will stay in the same orbit, defined by C, for an infinite time. In his study Jeffery also computed the average rate of dissipation of energy during the periodic motion. It was suggested that after a sufficiently long time a spheroid should tend to adopt the value of C that results in the minimum average dissipation of energy. For prolate spheroids this value was found to be C=0.

In an attempt to verify Jeffery's minimum energy hypothesis Taylor (1923) was the first to conduct an experimental study on spheroids, in a flow between two concentric cylinders. The spheroids were observed to exhibit the flipping motion found by Jeffery, but no quantitative measurements were done to analyze the orbits. Nevertheless, prolate spheroids with $r_e < 3$ finally aligned with the axis of vorticity as suggested by Jeffery.

In a similar study on a similar experimental setup, Binder (1939) studied the rotation of cylindrical particles with varying aspect ratios $r_p = l/d$, where l is the length of the particle and d is the diamater. For particles with an aspect ratio less than $r_p \approx 15$ the particles reached a final state corresponding to C = 0. However, for longer particles steady orbits of large C were observed, thus clearly not consistent with Jeffery's minimum energy hypothesis. Binder suggested that inertial effects in the experiments could be one reason for the discrepancy.

Trevelyan & Mason (1951) were first to experimentally verify Jeffery's solution quantitatively. Their experiments were performed in a Couette apparatus using cylindrical particles with r_p ranging from 20 to 120. An equivalent aspect ratio was determined by measuring the period of rotation and extract r_e from (2.6).

Later the equations of Jeffery have been verified experimentally in several studies, e.g. Goldsmith & Mason (1962), Anczurowski & Mason (1968), Stover & Cohen (1990). In the study by Goldsmith & Mason the experiments were conducted in a circular Poiseuille flow, i.e. with a velocity governed by

$$u(r) = \frac{2Q}{\pi R^4} (R^2 - r^2), \tag{2.9}$$

where Q is the volume rate of flow, r is the radial distance from the center of the tube and R is the radius of the tube. The motion of the rods was in good agreement with Jeffery's equations, provided that an equivalent aspect ratio was found from the measured period and equation (2.6), with $\dot{\gamma}$ taken at the r-position where the centre of the rod was located.

That fibres will rotate in Jeffery orbits also in parabolic flow was also shown analytically by Chwang (1975). He computed the rotation rate of spheroids in flows governed by $\mathbf{u} = K(y^2 + z^2)\mathbf{e_x}$, where K is a constant of unit [1/ms]. The final solution for the rotation rate is equivalent to the solution of Jeffery if the shear rate is evaluated in the particle centre. However, in these flows the translational velocity of the fibre centre will not be constant during one period

of rotation. This can also be inferred from the results by Pittman & Kasiri (1992) who applied slender body theory on a fibre in a general Stokes flow.

As already mentioned work has been conducted in order to find the equivalent ellipsoidal aspect ratio for cylindrical particles, e.g. Trevelyan & Mason (1951), Goldsmith & Mason (1962), Anczurowski & Mason (1968), Cox (1971) and Harris & Pittman (1975). Anczurowski & Mason measured the periodic orbits of spheroids in a Couette flow. The results were in good agreement with Jeffery's equations. In the same study experiments were conducted on cylindrical particles, primarily in order to determine the point of transition from discs $(r_e < 1)$ to rods $(r_e > 1)$, corresponding to orbits of oblate and prolate spheroids, respectively. The transition was found to take place at a particle aspect ratio of $r_p = 0.86$. A second result from the study was that $r_p = r_e$ when $r_p = 1.68$. Experiments were also carried out on particles of r_p up to 100 and the equivalent r_e was calculated.

One of the key results in the theoretical study by Cox (1971) was an expression relating r_p of cylindrical bodies to an equivalent r_e

$$r_e = \left(\frac{8\pi}{3L}\right)^{1/2} r_p (\ln r_p)^{-1/2},$$
 (2.10)

where L is a constant dependent on the shape of the blunt ends of the body. Cox compared equation (2.10) to the experiments conducted on cylindrical particles by Anczurowski & Mason and concluded that L=5.45 resulted in the best fit. Equation (2.10) is derived for long bodies and is valid only for large r_p . Another expression relating r_p of cylindrical particles to an equivalent r_e was deduced by Harris & Pittman (1975). Experiments were made in a plane Couette flow, which resulted in

$$r_e = 1.14r_p^{0.844}. (2.11)$$

The expression was reported to agree with the measurements of Trevelyan & Mason, within 5%, down to $r_p=1$.

There are several analytical studies on elongated particles in Stokes flows, which are not necessarily restricted to shear flows. For instance Chwang & Wu (1974, 1975) presented a number of exact solutions to Stokes flow problems, including flows past prolate spheroids.

A branch of theoretical studies which is of relevance when studying fibre suspensions is slender body theory. The essence of slender body theory is to approximate the velocity disturbance of the fluid, due to the presence of the fibre, with a line distribution of flow singularities along the axis of the fibre. The singularities are adjusted, in nature and in strength, so that the no-slip condition is fulfilled at the fibre surface. As the name implies the theory make use of the slenderness of fibres. In an outer limit, where the distance δ from the fibre centre $\delta >> d$, the fibre appears as a line with finite length but with zero thickness. In an inner limit, where $\delta << l$ and $\delta = O(d)$, the fibre has a finite

thickness but appears infinitely long. Solutions are found in these two limits and are matched in a region where $d << \delta << l$ in order to form a consistent solution.

There are several studies using slender body theory in Stokes flows, e.g. Batchelor (1970), Cox (1970, 1971), Tillett (1970), Keller & Rubinow (1976), Geer (1976), Johnson (1980). The studies by Cox and Tillett both considered bodies of circular cross-section, where Cox also allowed a curvature of the body. Batchelor studied straight bodies with an arbitrary non-circular cross-section. Keller & Rubinow investigated slender bodies that may twist and dilate and Johnson introduced a more accurate description and accounted for the flow near the fibre ends.

2.2.2. Wall-bounded shear flows

The analysis by Jeffery was made under the assumption that Stokes equations are valid. Apart from this assumption it was also assumed that there were neither particle interactions nor any wall effects. A few studies have been made concerning the motion of elongated particles in the presence of solid boundaries.

Yang & Leal (1984) considered the motion of a slender body near a fluidfluid interface. By setting the viscosity of the nearby fluid to infinity a wall is modeled. It is shown that this causes a small disturbance to Jeffery's solution. The motion is shown to be periodic both for translation and rotation. As in unbounded shear flows the fibre end points form closed orbits. The periodicity of the motion is due to the symmetry of the problem and the reversibility condition of Stokes flows.

Dabros (1985) calculated numerically the motion of a prolate spheroid, with an aspect ratio $r_e=2$, close to a solid boundary. The spheroid was located in the flow-gradient plane, *i.e.* far away from the wall the motion would be described by Jeffery's equations for $C\to\infty$. At large distances from the wall the angular velocity $\dot{\phi}$ of the spheroid coincided with the solution of Jeffery. Near the wall, at a distance of y/a=2.1, where a is the half length of the spheroid and y is the distance from the wall to the particle centre when $\phi=0$, the angular velocity of the spheroid was slightly smaller. This was in particular seen in the phase of the orbit when the spheroid was oriented parallel to the wall, *i.e* when $\phi=0$.

Hsu & Ganatos (1989, 1994) used a boundary integral method to compute the motion of a prolate spheroid in a shear flow, at distances from the wall down to y/a = 1.1. As in the study by Dabros the spheroid was fixed in the flow-gradient plane. The spheroid underwent a periodic tumbling motion similar to the motion described by Jeffery, but also oscillated periodically in the wall normal direction. A similar study with similar results was done by Gavze & Shapiro (1997). Also here a periodic oscillation was found towards and away

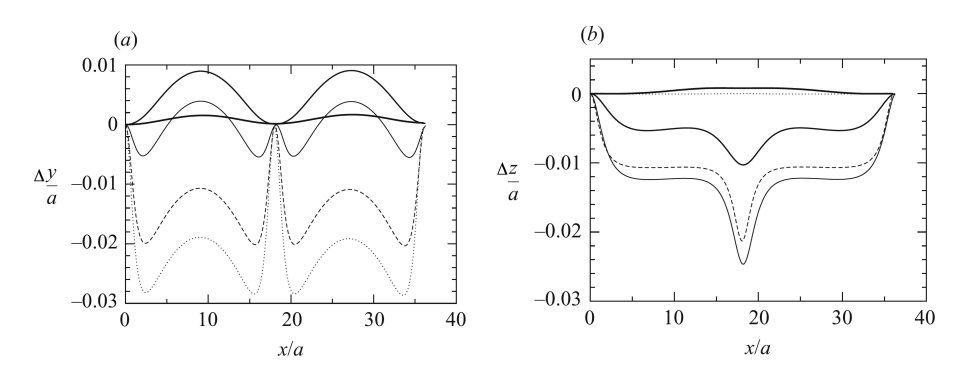


FIGURE 2.3. Projection of the particle centre, of a spheroid with $r_e=4$, in the (a) xy-plane and (b) xz-planes for y/a=1.25. The various lines correspond to an initial angle to the xy-plane of $\Phi_0/\pi=0$ (dotted line), $\Phi_0/\pi=0.125$ (dashed line), $\Phi_0/\pi=0.25$ (solid line), $\Phi_0/\pi=0.375$ (thick solid line) and $\Phi_0/\pi=0.46875$ (bold solid line). From Pozrikidis (2005).

from the wall for small distances to the wall. It was also concluded that the tumbling motion could approximately be described by Jeffery's equations, but with a larger period closer to the wall.

Pozrikidis (2005) made a numerical analysis of the motion of a spheroid near a solid wall. This study, was however not restricted to motions where the particle was fixed in the flow-gradient plane. The initial inclination angle Φ_0 of the spheroid, to the flow-gradient plane, was varied in the computations. The motion of the particle centre is shown in figure 2.3, where Δy and Δz are the displacements in y and z from the initial value at x=0. Also in this study the particle centre moved periodically in the wall normal direction, when located near the wall. A periodical motion parallel to the vorticity axis was also found when the spheroid was not initially oriented in the flow-gradient plane nor directed parallel to the vorticity axis. As expected the end points of the spheroid formed closed orbits during rotation also in the presence of the wall. For all initial conditions under study a longer period than the Jeffery period was found near the wall. For a particle with $r_e=4$ the period increased with approximately 10%, at a distance from the wall of y/a=1.25, for any initial angle to the flow-gradient plane.

The period of the rotation has experimentally been found to agree with Jeffery's solution down to distances from the wall of one fibre length, e.g. Stover & Cohen (1990) and Moses, Advani & Reinhardt (2001). Stover & Cohen made measurements on fibres with $r_p=12$ in a pressure-driven flow between two solid walls. Closer to the wall than one fibre length the motion was still periodic, but with a longer period than predicted by the shear rate and Jeffery's

solution. This trend was seen independent of the value of C. Furthermore, a non-hydrodynamic fibre-wall interaction was observed for fibres with a large value of C located at a distance from the wall smaller than half a fibre length. During the flipping phase of the rotation the leading end was observed to make contact with the wall and the fibre was pushed away from the wall so that its centre ended up close to half a fibre length from the wall. This was referred to as a "pole vaulting" motion. A requirement for Stokes flow reversibility and symmetry of the problem is that the average distance from the wall of the fibre, averaged over a complete period of rotation, should be maintained. The fact that this was not observed shows that the "pole vaulting" interaction with the wall is not a pure Stokes flow interaction.

Holm & Söderberg (2007) made another interesting experimental observation. The fibre orientation was studied in planes parallel to a wall in a fibre suspension flowing down an inclined wall. Experiments were conducted on fibres with aspect ratios in the range between 10 and 40. The fibres had a slightly higher density than the fluid making the fibres sediment slowly. For small aspect ratios a significant amount of the fibres were oriented perpendicular to the flow direction in the near wall region.

Carlsson et al. (2007) made measurements on essentially the same experimental setup on fibres with $r_p \approx 7$. It was found that most fibres were close to aligned with the flow direction down to distances from the wall of y/l=0.5. Closer to the wall the fibres adopted orientations within the reduced set of possible orientation for fibres rotating in Jeffery orbits without hitting the wall. In the very proximity of the wall basically all fibres were oriented close to perpendicular to the flow direction.

The slender body theory, mentioned in the preceding section, can be a useful tool also in wall-bounded flows. The image system of a slender body near a solid wall was studied by Blake (1974). The no-slip condition at the wall was obtained by introducing a distribution of flow singularities along the axis of a mirrored image fibre in addition to a point force distribution along the physical fibre.

The image system of Blake was used by Russel et al. (1977) in order to calculate the motion of a rod falling due to sedimentation near a vertical wall. Two types of interactions with the wall were found. There was one so called glancing interaction for a fibre approaching the wall with a small angle to the wall. In this case the fibre turned its orientation to parallel to the wall and drifted away from the wall with the same fibre end leading. The other type of interaction was called reversing. This was found for fibres with larger angles to the wall. The leading end of the fibre encountered a near wall interaction and turned its orientation so that the opposite end was leading as it drifted away from the wall. These interactions were also observed experimentally in qualitative agreement with the theoretical results.

2.2.3. Fibre-fibre interactions

In fibre suspension flows and other multiphase flows, the particles in general interact through fluid stresses or direct mechanical contact. The velocity disturbance due to a fibre barely decays until the separation from the fibre is about one fibre length. This implies that the volume set into motion by a moving fibre is $O(l^3)$. Therefore it is natural to introduce nl^3 , where n is the number density per unit volume, to denote the concentration of a suspension.

A common procedure to get an indication of the significance of fibre-fibre interactions is to consider different regimes of concentration. Appropriate regimes in linear flow according to Sundararajakumar & Koch (1997) are dilute $(nl^3 << 1)$ where interactions are rare, semi-dilute $(nl^3 >> 1, nl^2d << 1)$ where far-field hydrodynamic interactions are dominating and semi-concentrated $(nl^2d=O(1))$ where near-field interactions as well as mechanical contacts become frequent. In the headbox of a paper machine nl^3 is typically between 5 and 50 and would usually be considered to be in the semi-dilute regime.

It was shown by Harlen, Sundararajakumar & Koch (1999) that mechanical contact between fibres could be of significance also at lower concentrations if the flow is non-linear, *i.e.* if the velocity gradient is not constant over the length of the fibre. Another interesting finding of this work is that lubrication forces will not prevent fibres from contact unless the fibres are nearly aligned.

It is well known that fibre tend to flocculate, *i.e.* that fibres form aggregates or bundles. This results in strong local variations of the fibre concentration. Mason (1954) conducted experiments in a cylindrical Couette apparatus to study fibre interactions in a shear flow. Experiments were done with spheres, cylindrical particles and pulp fibres. Mason concluded that the main mechanism for flocculation of fibres was mechanical interactions between fibres. In a later study by Kerekes & Schell (1992) the crowding factor N was found to be useful to characterize the regimes of fibre flocculation. N is defined as the average number of fibres located in a volume of a sphere with diameter l. It is worth noticing that N only differs from nl^3 by a numerical factor, $N = \pi nl^3/6$.

Some attention has been given to understand how fibre-fibre interactions are expected to affect the fibre dynamics in shear flows. In the dilute regime Jeffery's analysis has been verified numerically and experimentally. However, it turns out that the analysis provides a good approximation also for higher concentrations. Koch & Shaqfeh (1990) derived a correction to the rate of rotation, due to hydrodynamic interaction in a semi-dilute fibre suspension. For a Jeffery rotation rate of $O(\dot{\gamma})$ in a dilute suspension the correction due to hydrodynamic interactions was shown to be $O(\dot{\gamma}/\ln(1/c_v))$ in the semi-dilute regime, where c_v is the volume fraction of fibres.

Sundararajakumar & Koch (1997) made numeric simulations in an attempt to capture the fibre motion in the semi-concentrated regime. Hydrodynamic

interactions were neglected and only interactions due to direct mechanical contact were included. It was concluded that collisions between fibres caused them to flip more frequently.

A number of experimental studies have also been performed in order to investigate how the orientation distribution is modified in shear flows due to interactions. Mason & Manley (1956) studied the motion of cylindrical particles on low concentration suspensions $(nl^3 < 1)$ with r_p in the range between 20 and 120. A drift towards a preferential orientation in the flow direction was seen, for all initially isotropic suspensions. The drift was stronger for larger r_p . Similar experiments were performed by Anczurowski & Mason (1967). The orbit distribution of rods of $r_p = 18.4$ was investigated for concentrations in the range $nl^3 = 0.016$ to 0.52. For $nl^3 < 0.1$ the distribution of orbits was independent of the concentration. About 50% of the fibres rotated in orbits with C < 0.2. Although only low concentrations were investigated a small shift in the direction of orbits corresponding to higher values of C was seen when the concentration was increased.

Stover, Koch & Cohen (1992) carried out experiments on index-of-refraction matched suspensions in order to visualise suspensions in the semi-dilute regime. The experiments were done in a cylindrical Couette apparatus. The fibre aspect ratios were $r_p=16.9$ and 31.9 and the concentrations varied between $nl^3=1$ and 45. The particles were reported to rotate around the vorticity axis similar to Jeffery orbits, also for the highest concentration. At small concentrations lower values of C was favoured, but with an increase of concentration the C-distribution was shifted towards higher values, i.e. towards a distribution more aligned with the flow direction. Thus, the shift towards a more preferential orientation in the flow direction, with increasing concentration, continues also in the semi-dilute regime.

Experiments with fibre suspensions with $r_p \geq 50$ and concentrations between $nl^2d=0.2$ and 3, were conducted by Petrich, Koch & Cohen (2000). In consistency with Sundararajakumar & Koch the period of rotation was shorter than the period predicted by Jeffery. At $nl^2d=0.2$ the period was about 20% shorter than that given by equation (2.6). However, when the concentration was increased the period returned to values close to the dilute result. The fibre orientation was also considered. With an increasing concentration the distribution of orbits shifted slightly towards smaller values of C.

2.2.4. Deformed and flexible fibres

The majority of the mentioned studies so far have only been considering straight and rigid fibres. In industrial applications fibres are generally deformed and flexible to some extent. This is very much the case in papermaking. Methods for measuring the flexibility of wet pulp fibres have been developed by Samuelsson (1963) and Tam Doo & Kerekes (1981, 1982). The flexibility varies

significantly with the different kinds of pulp. Tests by Tam Doo & Kerekes showed that chemical pulps could be up to 30 times more flexible than mechanical pulps from the same wood.

It is convenient to introduce a non-dimensional parameter $\chi=8\pi\mu\dot{\gamma}l^4/EI$, which is a measure of the ratio between hydrodynamic and elastic forces, to estimate whether a fibre is likely to deform, e.g. Tornberg & Shelley (2004). Here μ is the dynamic viscosity of the fluid and EI is the rigidity of the fibre including the Young's modulus E and the area moment of inertia I. From Tam Doo & Kerekes the value of EI is found in the range $(1-200)\cdot 10^{-12}~\mathrm{Nm}^2$ for different kinds of pulp. With fibre lengths between 0.5 and 3 mm and a typical shear rate of around $1000~\mathrm{s}^{-1}$ near the wall of a headbox this results in values of χ between 0.01 and 1000. Thus, the significance of flexibility effects is likely to vary with different kinds of pulp.

Mason (1954) and Arlov, Forgacs & Mason (1958) studied the motion of individual pulp fibres in a cylindric Couette apparatus. A rigid but curved fibre was observed to rotate in a nearly constant orbit, similar to the motion expected for a straight fibre, in over 80 rotations. For flexible fibres the motion was more complex although it was found possible to qualitatively classify the different motions into a limited set of groups. In figure 2.4 the different groups are illustrated.

Further studies on the flexibility of fibres were conducted by Forgacs & Mason (1959a,b). The fibres were analyzed in the flow-gradient plane. For small aspect ratios, *i.e.* in the rigid regime, the period of rotation was found to coincide with Jeffery's theory. At some aspect ratio, where the fibres could no longer be regarded as rigid, the fibres started to move in a motion referred to as a "springy rotation", figure 2.4 (c). The linear relation between the period of rotation and the aspect ratio was no longer valid. Note from equation (2.6) that the period is almost linear for large aspect ratios. As the aspect ratio was increased even further there was a sudden drop in the period of rotation as the fibres started to undergo a "snake turn", figure 2.4 (d). Another finding by Forgacs & Mason was that the rotation of a curved but rigid fibre in the xy-plane could be described as a Jeffery orbit with a smaller effective aspect ratio. This aspect ratio was found to be close to the aspect ratio of a body formed by revolution about a choord joining the ends of the curved fibre.

The different motions of flexible fibres in shear flows found by Mason and co-workers have been qualitatively reproduced in several numerical investigations, e.g. Yamamoto & Matsuoka (1993), Ross & Klingenberg (1997), Skjetne, Ross & Klingenberg (1997), Stockie & Green (1998), Lindström & Uesaka (2007) and Qi (2007). There has also been a number of studies on the tendency of a flexible fibre to adopt preferential orbits, e.g. Skjetne, Ross & Klingenberg (1997), Joung & N. Phan-Thien (2001), Wang, Yu & Zhou (2006). A general conclusion from these studies is that a flexible fibre will tend to end up in an

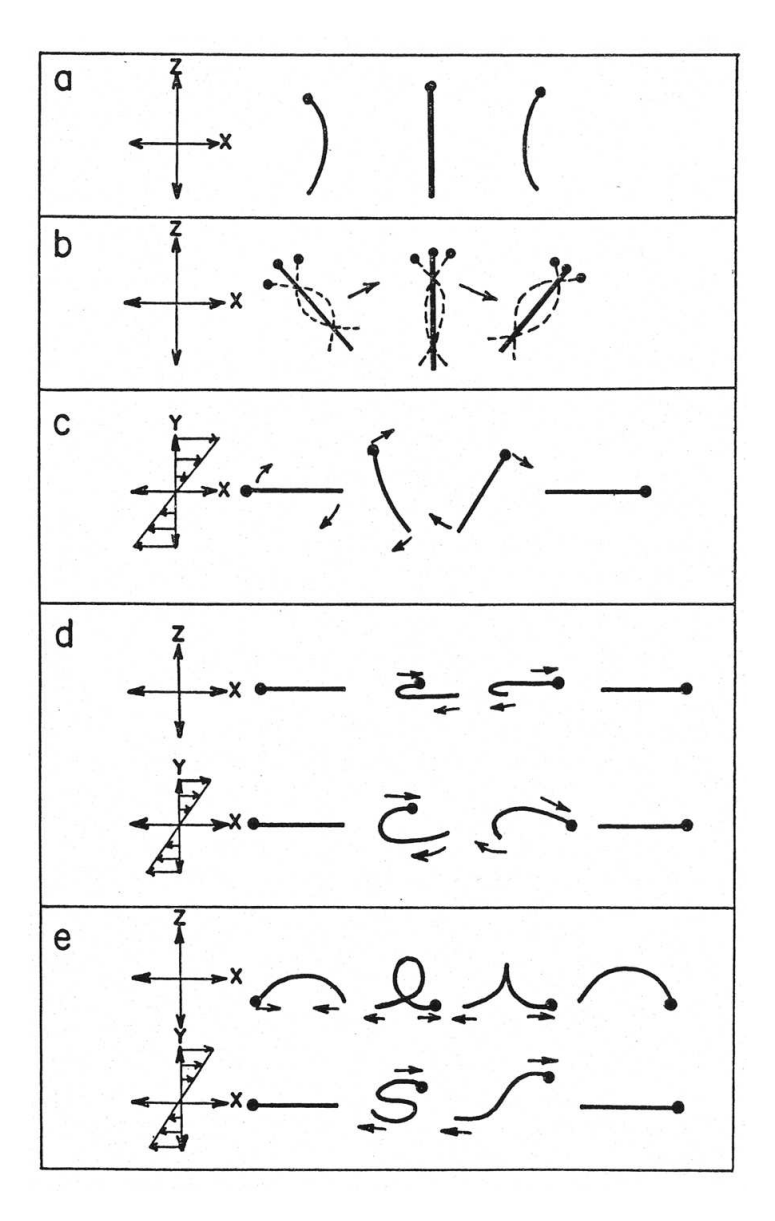


FIGURE 2.4. Typical rotational orbits of flexible fibres. The black dots denote the same end throughout the same type of rotation: (a) flexible spin, (b) flexible spin superimposed on a spherical elliptical orbit, (c) springy rotation, (d) snake turn and (e) s-turn. From Arlov, Forgacs & Mason (1958).

orbit corresponding to C = 0 (flexible spin around the vorticity axis) or $C \to \infty$ (rotation in the xy-plane), depending on its original orientation.

2.2.5. Inertial effects

The Stokes flow model is valid only if all inertial effects can be neglected. A fibre will generally tend to travel with a velocity close to that of the surrounding fluid. Therefore the relative velocity between the fibre and fluid is often small and neglecting inertia is often a meaningful approximation. Nevertheless, if there is a large velocity gradient in the region around the fibre, inertial effects could be significant. In order to determine whether inertial effects are significant or not it is convenient to introduce an appropriate Reynolds number. The most frequent Reynolds number encountered in literature is $Re_l = \dot{\gamma} l^2/\nu$, where $\dot{\gamma} l$ is a characteristic relative velocity. If $Re_l << 1$ neglecting the inertial effects is generally a sensible assumption. However, close to the wall in a headbox Re_l can reach values of about 1000 and inertial effects can certainly not be expected to be negligible.

A theoretical study concerning fluid inertial effects on long slender bodies was performed by Khayat & Cox (1989). In the absence of inertia a sedimenting fibre will maintain its orientation. When inertia is present a sedimenting fibre rotates to an equilibrium horizontal orientation, perpendicular to the direction of gravity.

In shear flows it has been shown that a small Re_l will tend to drift elongated particles to finally be rotating in the xy-plane, e.g. Qi & Luo (2002, 2003) and Subramanian & Koch (2005). It has also been shown that particle inertia will tend to drift a elongated particles to be rotating in this plane, e.g. Subramanian & Koch (2006) and Altenbach $et\ al.$ (2007).

Subramanian & Koch (2005) considered a slender fibre in a simple shear flow and concluded, apart from the drift in orientation, that at a critical Re_l the fibre stops rotating and obtains a final stationary orientation in the xy-plane. The case where both shear and sedimentation were accounted for was also examined. A Reynolds number based on the sedimentation velocity U_{sed} was introduced, $Re_{sed} = U_{sed}l/\nu$. For a sufficiently large Re_{sed} , as compared to Re_l , the orbit constant C will instead drift towards zero and finally align with the vorticity axis.

Aidun, Lu & Ding (1998) and Ding & Aidun (2000) also found that the period of rotation increases to infinity at some critical Reynolds number for elliptical cylinders and oblate spheroids in simple shear flows. It was also found that this critical Reynolds number increased with an increasing solid-fluid density ratio. According to Qi & Luo (2002, 2003) a neutrally buoyant prolate spheroid with $r_e = 2$ increases its period of rotation with Re_l , but the particle never ceases to rotate. For small Re_l there was an orbit drift towards

 $C \to \infty$, but for larger values of Re_l than about 345 the spheroid finally ended up at C = 0.

It can be worth pointing out that the results of Subramanian & Koch (2005) and Qi & Luo (2002, 2003), concerning if the particle continues to rotate or not at larger Re_l , are not necessarily contradicting. Recall that the particle shapes under consideration are very different. Another factor is that the spheroid considered by Qi & Luo was neutrally buoyant and the particle inertia of the spheroid will tend to reduce changes in the angular momentum. It is thereby not inferred that including particle inertia in the study by Subramanian & Koch would have altered their result. As mentioned before, the volume of fluid set into motion by a fibre is $O(l^3)$. This should be compared to the volume of the fibre which is $O(ld^2)$. This implies that, for a neutrally buoyant fibre, the momentum of the fibre induced velocity disturbance is much greater than the momentum of the fibre itself. As a consequence fluid inertia is expected to be more significant than particle inertia for slender bodies. This relation holds as long as Re_l is sufficiently small and the density ratio between the fibre and fluid is not too large. For the case of a spheroid with a small aspect ratio the difference in volumes between the spheroid and the velocity disturbance is not so large and it is therefore not justified to neglect particle inertia.

2.2.6. Flow at large Reynolds numbers in a headbox

The headbox nozzle is basically a planar converging channel. The free jet that exits the headbox, with a velocity of up to $30~\mathrm{m/s}$, is generally about $10~\mathrm{m}$ wide and $10~\mathrm{mm}$ thick. An estimation of the boundary layer thickness and the shear rate along the headbox walls can be found from the similarity solution for laminar flow in a two-dimensional convergent channel, e.g. Schlichting (1979). The velocity is then given by

$$\frac{u}{U_e} = 3 \tanh^2 \left(\frac{\eta}{\sqrt{2}} + 1.146\right) - 2,$$
 (2.12)

where U_e is the velocity of the fluid outside the boundary layer and η is defined as

$$\eta = y' \sqrt{\frac{U_e}{-(x'-x_0')\nu}},$$
(2.13)

where the coordinates are defined in figure 2.5. The boundary layer thickness decreases in the streamwise direction and is typically below 1 mm near the end of the contraction. The shear rate in the boundary layer is typically of the order $1000 \, \mathrm{s}^{-1}$, although this also changes with the streamwise position and distance from the wall.

Due to the high flow rates in a headbox the flow is to a large extent turbulent. However, if a turbulent boundary layer is accelerated by a strong

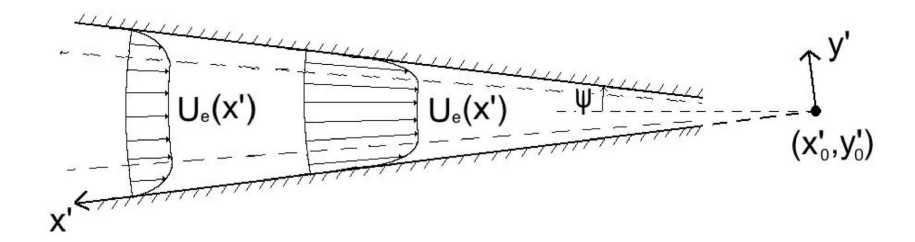


Figure 2.5. Two-dimensional convergent channel.

favourable pressure gradient it can return to a laminar-like state, see for instance Moretti & Kays (1965) or Parsheh (2001). This phenomenon is usually termed relaminarization. Parsheh studied the flow in a 2D convergent channel experimentally, with application to headboxes. It was found that the initially turbulent boundary layer approached the laminar self-similar state near the end of the contraction. A non-dimensional acceleration parameter

$$K = \frac{2\nu \tan \psi}{q} \tag{2.14}$$

is often introduced to quantify the relaminarization process, where ψ is half the contraction angle and q is the flow rate per unit width. If K is above a critical value relaminarization is initiated. This value of K was found to be about $3.5 \cdot 10^{-6}$ by Moretti & Kays and about $3.1 \cdot 10^{-6}$ by Parsheh. In a headbox K is typically between $5 \cdot 10^{-7}$ and $6 \cdot 10^{-6}$. Note that a self-similar mean flow profile is not sufficient to conclude that the boundary layer is purely laminar. Furthermore, it has been shown that turbulent structures can remain in a relaminarized boundary layer, e.g. Warnack & Fernholz (1998) and Talamelli et~al.~(2002).

The fibre orientation distribution in a headbox tends to be highly anisotropic where the majority of the fibres are oriented close to the flow direction near the end of the contraction. The main mechanism for aligning the fibres is the positive streamwise rate-of-strain in the contraction, *i.e.* U_e increases downstream. This orientation is reflected in the orientation distribution in the final paper, where most fibres are oriented in the machine direction (MD).

It is emphasized that the final orientation distribution is not solely determined by the flow in the headbox. Fibres can alter their orientation also in the jet and during the following dewatering process. For instance a jet to wire speed difference has been shown by Nordström (2003b) to have an impact on the orientation in the final paper sheet. Both a positive and negative speed difference has been shown to result in a higher anisotropy, *i.e.* fibres more aligned in MD. Setting the speed difference to zero resulted in a more isotropic distribution. Nordström also found that the orientation distribution is more isotropic at both sheet surfaces than in the core of the paper. A more isotropic

distribution was also found by Asplund & Norman (2004) near the surface of a wall-bounded jet exiting a headbox. In the experiments by Asplund & Norman a lamella was also introduced in the center of the headbox. The orientation distribution was more isotropic in the wake behind the lamella than in the surrounding flow.

Aidun & Kovacs (1995) suggested, guided by their computations, that secondary flows, due to the boundary layers in the headbox, is the main cause for a non-uniform orientation distribution in the cross direction of the paper (CD).

A number of studies have been performed in order to estimate the fibre orientation distribution in a headbox. In a theoretical investigation Olson (2002) neglected all turbulent effects. The main conclusions from this investigation were that the fibre orientation distribution is independent of the flow rate through the headbox and that the fibres were more oriented in the plane of the paper than in the plane of the contraction. Also, it was concluded that the only geometrical factor affecting the fibre orientation is the contraction ratio. According to the derivations the shape of the headbox does not affect the orientation distribution at the end of the headbox.

To account for turbulence, coefficients for translational and angular dispersion can be entered into a convection-dispersion equation, which is usually called the Fokker-Planck equation. Thereby the evolution of the orientation distribution in time and space can be computed, e.g. Krushkal & Gallily (1988) and Olson & Kerekes (1998). This procedure has been implemented to study the orientation in convergent channels, e.g. Olson et al. (2004), Brown (2005), Parsheh, Brown & Aidun (2005, 2006a,b), Hyensjö et al. (2007) and Hyensjö & Dahlkild (2008). In order to validate the computations the experimental results of Ullmar (1998) are frequently used. Ullmar measured the fibre orientation in a laboratory scale headbox and showed that a more anisotropic distribution was obtained by an increased contraction rate. It was also found that altering the flow rate for a given contraction rate had a very small effect on the orientation distribution. This can also be inferred from the study by Nordström (2003a) where the flow rate through the headbox had a small effect on the orientation distribution in the final paper.

CHAPTER 3

Slowly settling fibres in a wall-bounded shear flow

This chapter gives a brief presentation of experimental and theoretical results on slowly settling fibres in a wall-bounded shear flow. For a more thorough presentation of the results the reader is referred to paper 1, 2 & 3 in part II of this thesis.

3.1. Experimental setup and flow situation

The orientation of slowly settling fibres suspended in a shear flow of a Newtonian fluid over a solid surface has been studied experimentally by Carlsson, Lundell & Söderberg (2007, 2009b) (Paper 1 & 2) and theoretically by Carlsson & Koch (2009) (Paper 3). The experiments were conducted on dilute fibre suspensions with $r_p \approx 7$ and 30. The experimental setup is sketched in figure 3.1. A film of the suspension with a thickness of $h \approx 17$ mm flowed down a slightly inclined plane, driven by gravity. The parallel section of the open channel is 1050 mm long and 100 mm wide. At the inlet there is a 150 mm long contraction that tend to make the orientation distribution aligned with the flow direction.

A coordinate system is introduced where x is the downstream position from the inlet of the open channel, y is the wall-normal position and z is the spanwise position. A camera is placed underneath the transparent plane, at x=750 mm (P in figure 3.1), to capture images parallel to the xz-plane. The orientation β is the orientation from the flow direction to the major axis of a fibre in this plane.

The flow is laminar with a velocity u in the x-direction given by the relation

$$u = \frac{g}{2u}y(2h - y)\sin\alpha,\tag{3.1}$$

where g is the constant acceleration of gravity, $\nu \approx 385 \cdot 10^{-6} \text{ m}^2/\text{s}$ is the kinematic viscosity of the fluid and $\alpha \approx 2.6^{\circ}$ is the inclination of the plane with respect to the horizontal. It was shown by Carlsson *et al.* (2007) that equation (3.1) holds quite accurately also for the fibre velocity in the streamwise direction.

The velocity of individual fibres is determined with a particle tracking velocimetry (PTV) algorithm. Combined with equation (3.1) the fibre velocity

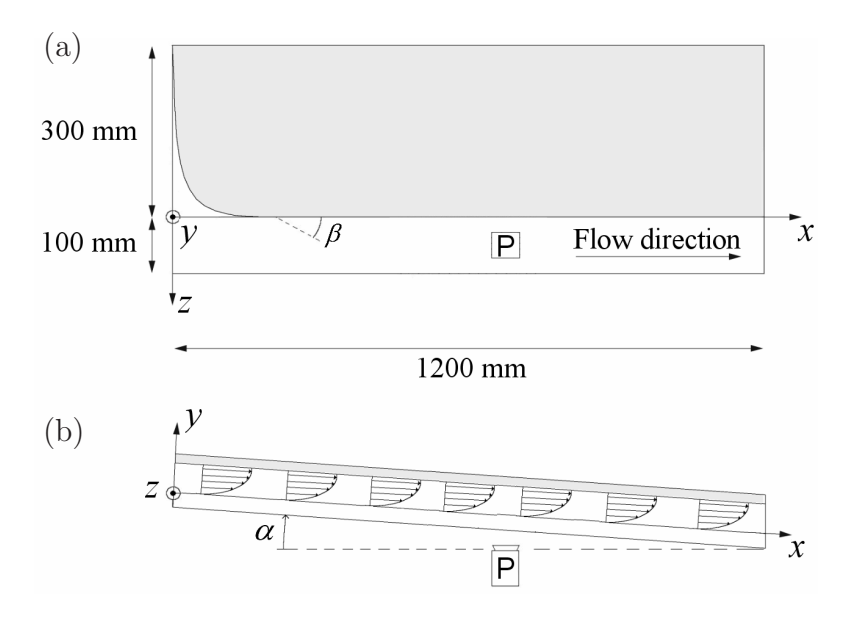


FIGURE 3.1. Schematic figure of the flow section, (a) Top view, (b) Side view. P denotes the camera position for the fibre orientation measurements.

is used to determine the distance from the wall of individual fibres. The orientation β , in the xz-plane, of the fibres is determined with a ridge detector within the class of steerable filters, e.g. Freeman & Adelson (1991). The particular ridge detector used here was derived by Jacob & Unser (2004) and was evaluated for the present purpose by Carlsson et al. (2009a) (Paper 5).

3.2. Results & discussion

Holm & Söderberg (2007) observed that fibres with $r_p \approx 10$ close to the wall were oriented perpendicular to the flow direction. In their experiments, however, the distance to the wall of the fibres was poorly resolved. With the same experimental setup Carlsson et al. (2007) investigated the possibility to influence the results by modifying the surface structure of wall. The smooth surface was replaced by a surface with ridges. A consequence was that fewer fibres settled all the way down to the wall. In addition the y-position of the fibres was now better resolved, than in the study by Holm & Söderberg, and new results were found for the flow over a smooth surface. It was shown that the orientation distribution only changes at distances from the wall closer than about half a fibre length. This is illustrated in figure 3.2 (a), where the orientation distribution, with darkness being proportional to the number density per unit angle, is shown for $r_p \approx 7$ and $nl^3 \approx 0.01$. In order to compensate for the

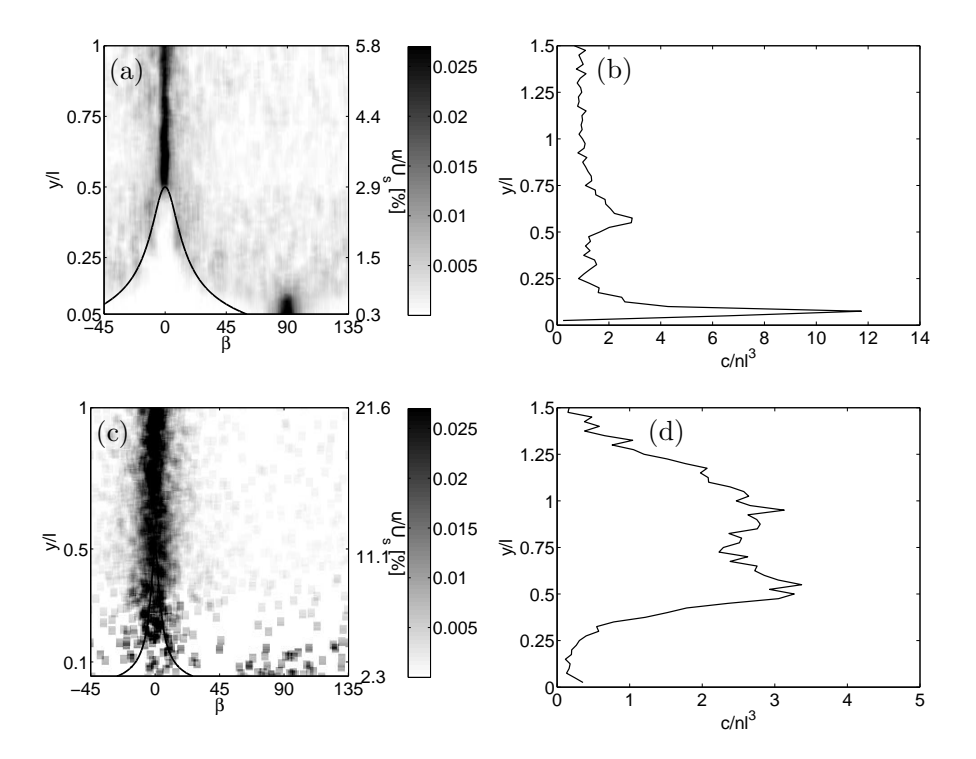


FIGURE 3.2. Orientation distributions and concentration profiles for $r_p \approx 7$ and $nl^3 \approx 0.01$ in (a) & (b) and for $r_p \approx 30$ and $nl^3 \approx 0.25$ in (c) & (d).

variation with y the distribution is normalized at each distance from the wall. The solid line in the figure denotes the minimum distance to the wall a fibre rotating in Jeffery orbits can be located at without touching the wall during the flipping phase of the rotation. It is clear from the figure that the fibres tend to adopt orientations above the solid line where motion in closed Jeffery orbits are possible.

In figure 3.2 (b) the fibre concentration as a function of y is shown for the same case. There is an increased concentration in the very proximity of the wall, where the fibres spin around their major axes aligned with the vorticity axis z. The increased concentration near the wall is due to the density difference between the fibres and the fluid. The fibres sediment with a velocity of about 10^{-6} m/s in the y-direction. For comparison the velocity in the x-direction at y/l = 0.5 is about $5 \cdot 10^{-3}$ m/s. There is another local increase of the concentration slightly above y/l = 0.5. It was noted in Carlsson *et al.* (2009b) that moving the peak to y/l = 0.5 would be within the accuracy of

the measurements. It is likely that this peak is a result from a "pole vaulting" motion near the wall, a motion observed earlier by Stover & Cohen (1990).

In figure 3.2 (c) and (d) the orientation distribution and concentration profile is shown for $r_p \approx 30$ and $nl^3 \approx 0.25$. It is clear from figure 3.2 (d) that there are fewer fibres at the wall for this aspect ratio. This is to some extent expected since the distance from the wall is scaled with the fibre length. This means that the residence time in the channel before reaching a certain x-position, for the longer fibres with $r_p \approx 30$, will only be roughly a quarter of the time it takes for the shorter fibres with $r_p \approx 7$ to reach the same position.

Since the concentration is low near the wall for $r_p \approx 30$ the statistics of the orientation distribution is probably rather inaccurate in figure 3.2 (c) and should therefore be interpreted with care. It was reported in Carlsson *et al.* (2009b) that the fibres below the solid line are all curved or mismatched in the PTV-algorithm.

Concluding, all straight fibres detected tend to adopt orientations above the solid line in figure 3.2 (a) and (c). The fibres located in the proximity of the wall are oriented in the region around $\beta=90^{\circ}$. It is possible that the lack of fibres with $r_p\approx 30$ near the wall could be an inertial effect. Recall that an effect of fluid inertia at small Re_l is to make a fibre migrate across orbits to a final state where the fibre is rotating in the xy-plane, e.g. Subramanian & Koch (2005). The wall reflection due to the settling towards the wall is expected to make the fibre migrate towards lower values of C to a final orientation aligned with the vorticity axis, Carlsson & Koch (2009).

In Carlsson et al. (2009b) the inertial effect was estimated based on the study of Subramanian & Koch and the effect of the fibre settling towards the wall was estimated based on the study by Carlsson & Koch (2009). The particle Reynolds number based on the shear rate near the wall is $Re_l \approx 0.01$ and 0.2 for the fibres with $r_p \approx 7$ and 30, respectively. The inertial drift towards larger C was estimated to be stronger than the wall reflection induced drift towards lower values of C for fibres with $r_p \approx 30$, for most orientations as long as there is no contact with the wall. This could possibly explain the indicative result that there are so few fibres with $r_p \approx 30$ near the wall. For fibres with $r_p \approx 7$ the inertial effects are expected to be small as compared to effects from settling towards the wall.

A slender body approach was used by Carlsson & Koch (2009) in order to estimate the effect of settling towards the wall on the fibre translation and rotation. All inertial effects are neglected and the fluid flow is assumed to be governed by Stokes equations. The shear induced wall reflection perturbs the motion given by Jeffery, but the motion maintains periodic and there is no cumulative orbit drift, e.g. Yang & Leal (1984) and Pozrikidis (2005). Therefore, only the velocity disturbance reflected at the wall due to the fibre settling

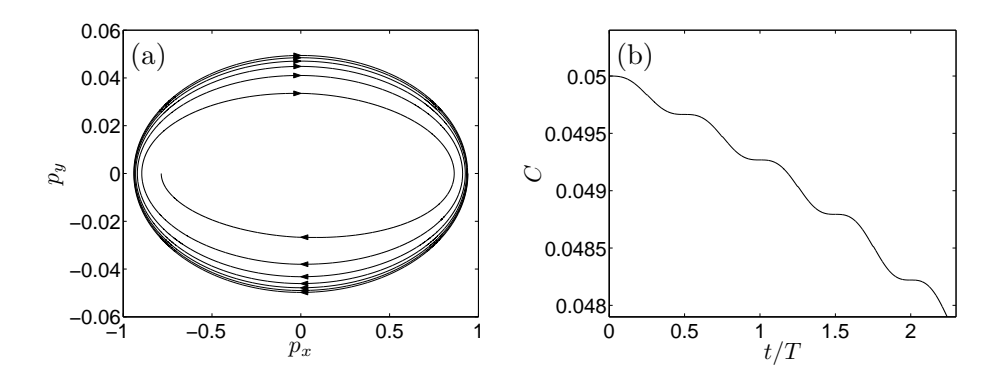


FIGURE 3.3. Orbit drift due to wall reflected velocity disturbance as a fibre settles towards a wall, (a) the evolution of the x and y-component of the unit vector p and (b) the evolution of C with time.

towards the wall and its effect on the fibre rotation is superimposed on Jeffery's equations for the fibre rotation.

The solid body contact is also modeled by introducing a contact force, applied at the fibre end in contact with the wall. No near wall hydrodynamic effects are included before this occurs and the wall reflection is neglected during the phase of the rotation when there is wall contact. This is motivated by assuming that the fibre rotation due to wall reflection is weak in comparison to the shear induced rotation given by Jeffery, which ensures that the wall contact will only take place in a small fraction of the period of rotation. A non-dimensional number $\Gamma = \Delta \rho g d/\mu \dot{\gamma} << 1$ is introduced to quantify the validity of this assumption. In the experiment described above $\Gamma \approx 0.007$. The mathematical details are given in Carlsson & Koch (2009).

The wall reflection due to settling towards the wall will tend to drift the Jeffery orbit towards lower values of C. This can be explained qualitatively by the following argument. Consider a fibre in quiescent fluid settling towards a wall. Independent of the orientation the wall reflection will always tend to rotate the fibre towards alignment with the wall. Since superposition applies, the fibre rotation due to wall reflection can be superimposed to the solution of Jeffery. In all phases of the Jeffery orbit when the fibre is not aligned with the wall the additional rotation rate due to the wall reflection will tend to rotate it towards alignment with the wall. As a result the amplitude in y that the fibre end points form in space during rotation will be smaller and smaller for each rotation.

An illustration of the orbit drift is shown in figure 3.3 (a) and (b). Note that here the fibre is positioned sufficiently far from the wall so that no wall contact

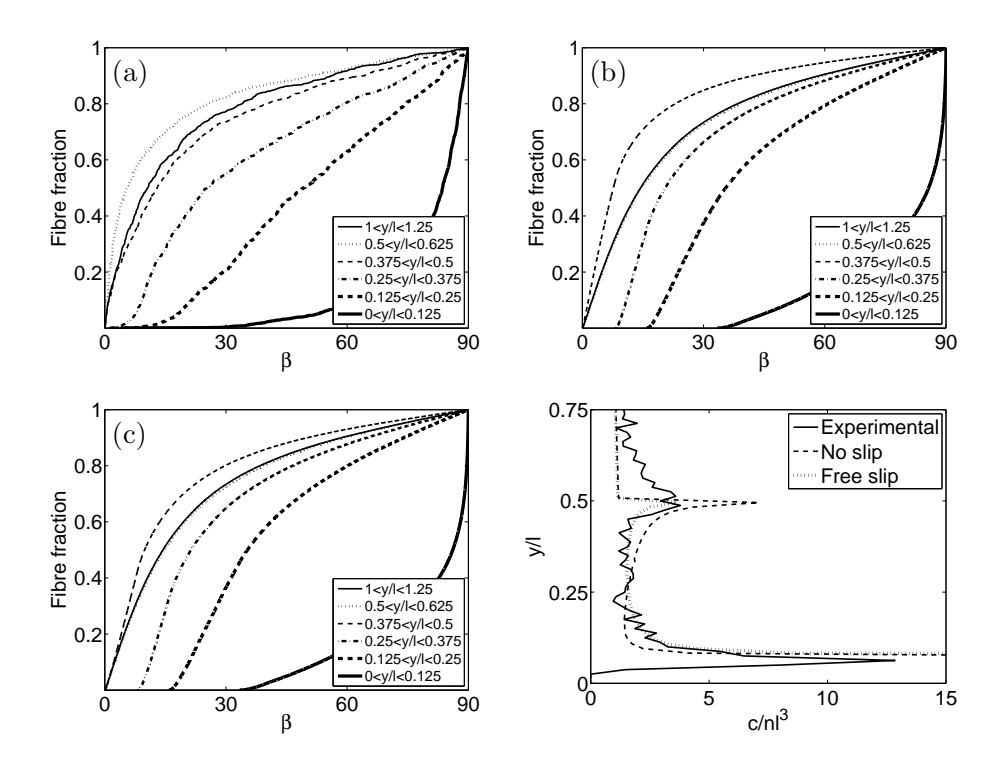


FIGURE 3.4. Experimental cumulative β -distribution in (a) and computational cumulative β -distribution with no slip and free slip wall contact condition in (b) and (c), respectively. Experimental and computational concentration profiles with both no slip and free slip condition shown in (d).

occurs. The drift is also stronger than in the experimental case, $\Gamma=0.07$, in order to better illustrate the effect in a limited number of orbits. In 3.3 (a) the evolution of the x and y-components of the unit vector p directed along the fibre is shown. It is seen that the amplitude of the orbits in y decreases with time. This implies that C decreases with time as shown in 3.3 (b).

Also the wall contact was shown to decrease the value of C. Two different wall contact conditions were implemented; a no slip condition were the fibre end point is not allowed to change its (x, z)-position at the wall and a free slip condition were the tangential components, with respect to the wall, of the wall contact force is equal to zero.

Since there is little data on the fibre orientation near the wall for the experiments with $r_p \approx 30$, due to the low concentration there, a comparison of the model is made only for the case with $r_p \approx 7$. By choosing a large set of

fibres at the inlet of the channel the orientation distribution and concentration can be computed at the x-position downstream corresponding to the position where the camera was located in the experiments. In the computations the initial orientation distribution was estimated by using the following relation for the steady state fibre orientation distribution for dilute and semi-dilute fibre suspensions

$$f(C) = \frac{RC}{\pi (4RC^2 + 1)^{3/2}}. (3.2)$$

Equation (3.2) was found by Rahnama *et al.* (1995) in the limit of large aspect ratio. $R \approx 0.57$ is found to approximately match the experimental β distribution at distances y > l, where the orientation is assumed to be unaffected by the wall. The concentration at the inlet of the channel is assumed to be homogenous in space.

In figure 3.4 (a), (b) and (c) the cumulative β -distributions for different y-positions are shown for the experiments and computations with both wall contact conditions. The general trend is that more fibres tend to adopt higher values of β as the distance from the wall is decreased, *i.e.* lower values of C closer to the wall. This is seen both in the experiments and computations. However, there is a local deviation from this trend. The thin solid line corresponds to the distance farthest away from the wall, 1 < y/l < 1.25. In the computations in (b) and (c) the orientation distribution barely changes, as the distance to the wall is decreased, until y/l < 0.5. It is seen that as the distance to the wall is decreased just below y/l = 0.5 the distribution shifts towards lower values of β . This is so because fibres with orientations close to $\beta = 0$ will make wall contact and begin to pole vault, while fibres with larger values of β continues to settle. This leads to an accumulation of fibres with small β close to y/l = 0.5, which is also seen in the concentration profile in figure 3.4 (d). This explains why the distribution can be shifted towards lower values of β , even when all fibres in the computations individually drift towards higher values of β with time.

A similar shift in the orientation distribution is found also in the experiments in figure 3.4 (a), although here the shift takes place somewhat farther away from the wall. A likely explanation to this can be deduced by returning to the concentration profile in (d). For y/l > 0.5 it should not be possible for the fibres to "pole vault". Still, the fact that the concentration starts to increase above y/l = 0.5, suggests that there are fibres present in the region that have begun to "pole vault". It is likely that the increase of concentration for y/l > 0.5 is primarily due to inaccuracies in measuring the y-position of the fibres. If it is true that some of the fibres in the region just above y/l = 0.5 actually are pole vaulting it is not surprising that there is also shift towards lower β as seen in 3.4 (a).

30 3. SLOWLY SETTLING FIBRES IN A WALL-BOUNDED SHEAR FLOW

Closer to the wall there is a qualitative agreement between the experimental and computational results. At the wall the fibres are nearly aligned with the vorticity axis, perpendicular to the flow direction.

CHAPTER 4

Near wall fibre orientation in a headbox

In this chapter experimental results from measurements on the fibre orientation in a boundary layer of a headbox are presented. A more detailed presentation is given in paper 4 in part II of this thesis.

4.1. Experimental procedure and flow situation

In Carlsson, Söderberg & Lundell (2009c) (Paper 4) experiments were conducted in a laboratory scale headbox. The headbox is illustrated in figure 4.1. It consists of a tube bank and a planar contraction. The width of the contraction in the y-direction is 100 mm, i.e. much less than an industrial headbox, and the other measures of the contraction are provided in the figure. A coordinate system is defined from the outlet of the contraction, where x runs upstream along the upper wall of the contraction and z denotes the normal distance to the upper wall.

A camera was mounted to capture images in planes parallel to the upper wall, *i.e.* planes parallel to the xy-plane. A light sheet, slightly thicker than 1 mm at the centre of the channel in the y-direction, was generated parallel to the upper wall. The light sheet was traversed in order to study the fibre orientation at different distances from the wall. Measurements were done at x = 0.09, 0.25 and 0.45 m and at different z-positions.

A suspension of bleached unbeaten birch fibres was used. The mean fibre length was $l_m \approx 0.7$ mm and the mean width $w_m \approx 18 \ \mu \text{m}$. The concentration was estimated to $nl^3 \approx 0.15$, *i.e.* the suspension is very dilute as compared to an industrial case. The velocity of the outgoing jet was 8.7 m/s.

The fibre velocity profile close to the wall and the boundary layer thickness was measured by tracking the velocity of a limited set of fibres for various z-positions at x=0.25 and 0.45 m. The results are shown in figure 4.2. The solid lines are given by the similarity solution for laminar flow in a 2D planar contraction, see equation (2.12) and (2.13). Each dot shows the measured velocity of an individual fibre and the stars denote the measured mean velocity at a particular z-position. The measured fibre velocities are surprisingly close to the similarity solution. This implies that the boundary layer thickness, defined as the distance from the wall where the velocity is 99% of the free stream velocity, is about 0.6, 1.3, 2.3 mm for x=0.09, 0.25, 0.45 m, respectively. The

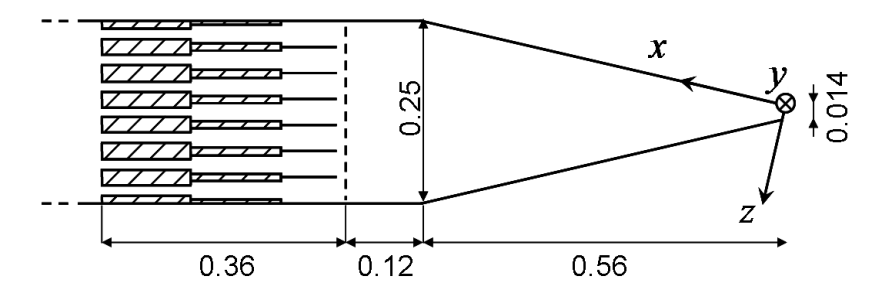


FIGURE 4.1. Schematic of the headbox with a coordinate originating from the outlet of the contraction. The measures are given in m.

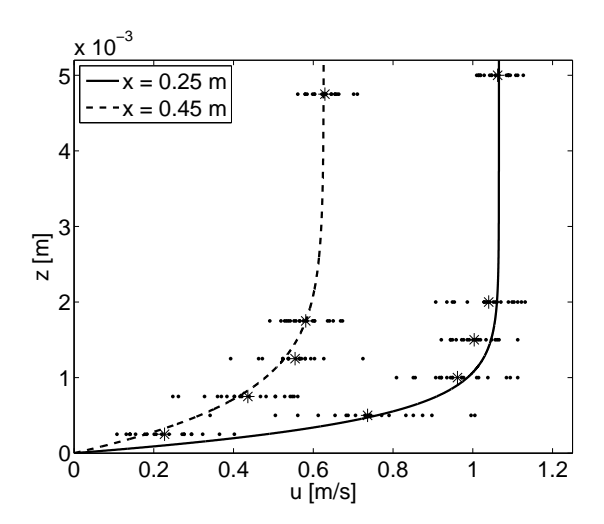


FIGURE 4.2. Velocity profiles at x=0.25 and 0.45 m. Solid lines given by similarity solution for 2D planar converging laminar flow.

shear rates at the same x-positions and $z = l_m$ are estimated to 230, 480 and 350 s⁻¹. Particle Reynolds numbers based on these shear rates and the mean fibre length are $Re_l \approx 110$, 240 and 170, respectively.

4.2. Fibre orientation in boundary layer

The fibre orientation distributions are shown for different (x,z)-positions in figure 4.3. It is noted that the distribution is asymmetric for x=0.45 m in figure 4.3 (a). This is surprising and is most likely due to an asymmetry in upstream flow. Farther downstream this asymmetry is less distinct. Disregarding the asymmetry a distinct trend is observed for x=0.45 and 0.25 m in (a) and

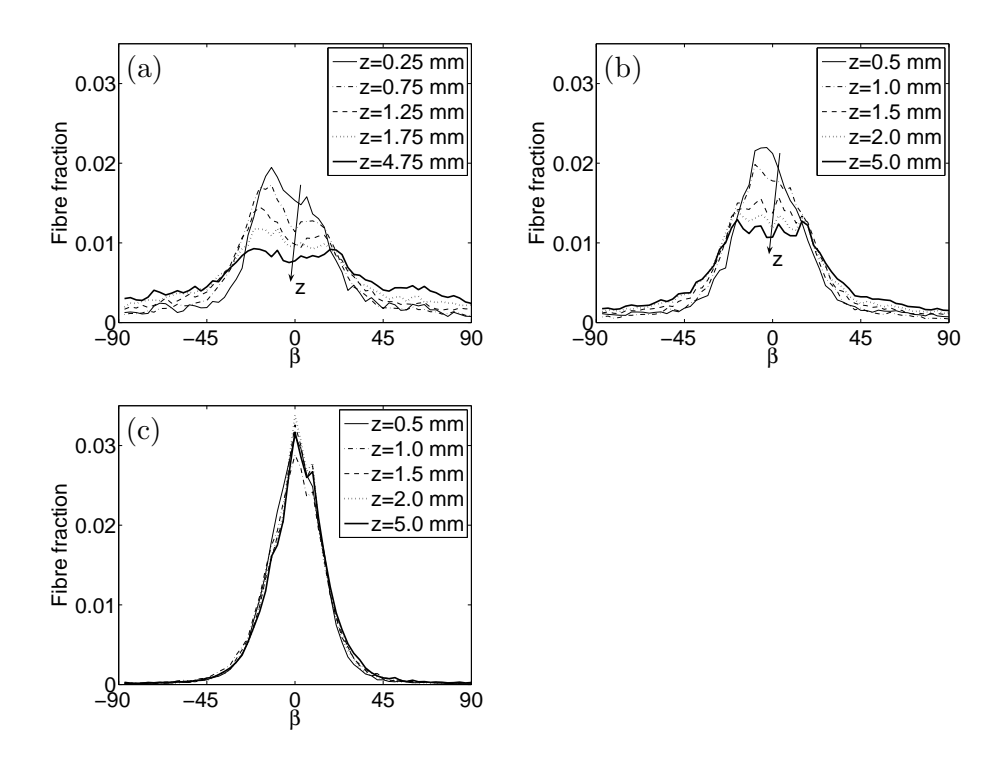


FIGURE 4.3. The orientation distribution of β for different distances from the wall z at (a) x=0.45 m, (b) x=0.25 m and (c) x=0.09 m.

(b). The distribution is more anisotropic near the wall, *i.e.* the fibres are more aligned with the flow at small z. A speculative explanation is that effects of fluid inertia could be more significant near the wall, where the shear rate is strong. Recall that a small but finite Re_l in a shear flow will tend to make a fibre more aligned with the flow direction, e.g. Subramanian & Koch (2005). Another possible explanation is that there are stronger fluctuations in the flow farther from the wall than near the wall in the relaminarizing boundary layer (as it appears from figure 4.2). Fluctuations are likely to make the fibre orientation distribution less anisotropic. However, here it should be recalled that a relaminarized boundary layer does not mean that the boundary layer is truly laminar, e.g. Warnack & Fernholz (1998) and Talamelli et al. (2002).

Farther downstream at x = 0.09 m in figure 4.3 (c) the z-dependency seen in (a) and (b) is not observed. The orientation distributions for different z more or less coincide at this x-position. As mentioned in section 2.2.6 concerning headbox flows, the positive streamwise rate-of-strain in the headbox is the main

34 4. NEAR WALL FIBRE ORIENTATION IN A HEADBOX

mechanism, far from the walls, for fibre alignment with the flow. The mean streamwise rate-of-strain increases in the downstream direction. Possibly the rate-of-strain has grown sufficiently strong in order to become the dominating mechanism influencing the fibre orientation also near the wall at $x=0.09~\mathrm{m}$.

CHAPTER 5

Concluding remarks

The main part of this study deals with settling fibres in a wall-bounded shear flow. This is a phenomena not dealt with previously even at small Reynolds numbers. A methodology has been developed in order to measure the fibre orientation in planes parallel to the wall and simultaneously measure the velocity of individual fibres. The velocity of a fibre indicates how far from the wall it is located. Thereby it is possible to obtain and investigate orientation distributions at different distances from the wall.

In the experiments the fibres enter a contraction far upstream from the point of measure. The contraction tends to align the fibres with the flow direction. It is shown that slowly settling fibres in a viscous shear flow finally end up very close to the wall aligned with the vorticity axis. The wall effect on the orientation is found to be weak for fibres located farther form the wall than half a fibre length from the wall.

A likely explanation for why the fibres end up aligned with the vorticity axis is the wall reflection of the velocity disturbance that is generated by the settling fibre in combination with repeated wall contacts during rotation. A fibre sedimenting towards a wall will tend to rotate toward a plane parallel to the wall. Superimposed on the shear induced rotation given by Jeffery (1922) this yields a slow migration toward lower values of C. This can be realized by considering a fibre with a rotation rate close to the equations of Jeffery. In every phase of the rotation where the fibre is not perfectly aligned with the flow-vorticity plane the wall reflection, due to settling toward the wall, will tend to rotate the fibre toward this plane. This leads to a spiraling motion toward the vorticity axis. The contact between the fibre end and the wall in each flip of the rotation will enhance the drift toward lower values of C.

In an experimental study in a boundary layer of a headbox the fibre orientation distribution and velocity was investigated. The study was carried out with pulp fibres with a flow rate smaller, although comparable, to the flow rates in an industrial headbox.

The velocity profiles in the boundary layers coincided surprisingly well with the similarity solution for laminar flow in a 2D convergent channel. The orientation distribution in a plane parallel to the wall was found to be more aligned near the flow direction with a decreasing distance to the wall. This trend was

36 5. CONCLUDING REMARKS

observed far upstream in the headbox. Farther down at the measurement station closest to the end of the contraction the orientation distribution appears to be independent of the distance from the wall. At least no difference can be detected within the accuracy of the measurements.

CHAPTER 6

Papers and authors contributions

The authors' contributions to the scientific papers and where the results have been presented are listed.

Paper 1

Fiber orientation control related to papermaking.

A. Carlsson (AC), F. Lundell (FL) & L. D. Söderberg (LDS). *Journal of Fluids Engineering*, Vol. 129 (4), 457-465 (2007). Corrigendum: Accepted for publication in J. *Fluids Eng.*.

AC performed the experiments and analysis under supervision of FL and LDS. AC, FL and LDS wrote the paper jointly. Parts of the results have been presented at (i) Nordic Rheology Conference, Royal Institute of Technology, Stockholm 2006, (ii) Euromech Fluids Mechanics Conference 6, Royal Institute of Technology, Stockholm 2006 and (iii) ASME Joint U.S.-European Fluids Engineering Summer Meeting, Miami, Fl, USA 2006.

A corrigendum is accepted for publication in *Journal of Fluids Engineering*. The corrigendum has been incorporated in the text.

Paper 2

Orientation of slowly sedimenting fibers in a flowing suspension near a plane wall.

A. Carlsson, F. Lundell & L. D. Söderberg.

Experiments, analysis and writing were performed by AC under supervision of LDS and FL. Parts of the results have been presented at (i) Svenska Mekanikdagarna, Luleå 2007 and (ii) 60th Annual Division of Fluid Dynamics Meeting of the American Physical Society, Salt Lake City, UT, USA 2008.

Paper 3

Orbit drift of a slowly settling fibre in a wall-bounded shear flow. A. Carlsson & D. L. Koch (DLK).

38 6. PAPERS AND AUTHORS CONTRIBUTIONS

AC and DLK performed theoretical derivations jointly. Numerical computations and writing were performed by AC under supervision of DLK.

Paper 4

Fibre orientation near a wall of a headbox. A. Carlsson, L. D. Söderberg & F. Lundell.

Experiments, analysis and writing were performed by AC with input from LDS and FL. Parts of the results have been presented at PaperCon '08 - TAPPI/PIMA/Coating Conference, Dallas, TX, USA 2008.

Paper 5

Evaluation of a steerable filter for detection of fibres in flowing suspensions. A. Carlsson, F. Lundell & L. D. Söderberg.

AC performed experiments and analysis under supervision of FL and LDS. AC, FL and LDS wrote the paper jointly.

APPENDIX A

Formation of fibres in streamwise streaks

Historically "turbulence" has been considered to be useful in fibre suspension flows in order to break up fibre aggregates and make the fibre concentration more homogenous, e.g. Norman & Söderberg (2001). It is well known that particles in turbulent flows can tend to concentrate in certain regions associated to the turbulent motion. A review on preferential concentration of particles in turbulent flows is given by Eaton & Fessler (1994). Here, it will be shown that a turbulent flow can also make fibres aggregate in streaks.

Measurements on a fibre suspension film flowing down a slightly inclined glass plate have been made. The setup is illustrated schematically in figure A.1 and is similar to the one used by Holm & Söderberg (2007) and Carlsson, Lundell & Söderberg (2007, 2009b). A CCD-camera was mounted below the glass plate in order to visualize the fibres in a plane parallel to the wall.

The fibre supension considered here consisted of cellulose acetate fibres with $r_p \approx 10$ suspended into tap water. The Reynolds number, based on the film thickness $h \approx 8$ mm and a free surface velocity $u_s \approx 0.5$ m/s, was about 4000. The flow was considered to be turbulent. The density of the fibres was approximately 1300 kg/m³.

A typical image is shown in figure A.2. Due to the relatively large density difference between the fibres and the fluid, a large amount of the fibres settled to the wall. At the wall the fibres moved slowly down the plate, mainly in the streamwise direction x, with a time-dependent velocity.

An interesting observation from the experiments was that the fibres tended to aggregate in streamwise streaks on the wall. In an attempt to quantify the streakiness the fibre density for each spanwise position z in the images was computed. This was done by a summation of all rows (x) in the image at each column (z). If the fibre density at a certain z-position exceeded a threshold value this indicated that there was a streak at this z. This also made it possible to study the evolution of the streaks as a function of time. In figure A.3 the white regions show where the fibre density is high and the black regions where there are few fibres. It is clear that the streaks are not stationary. The streaks drift in the spanwise direction and are observed to merge with each other and also to separate into more streaks. Further details can be found in Fjellgren (2007).

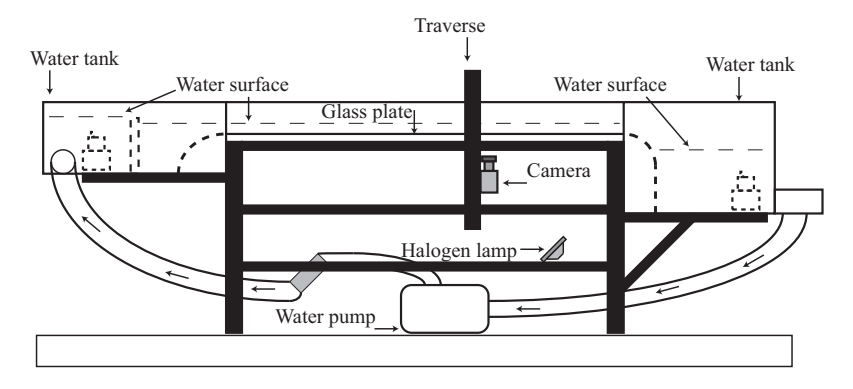


Figure A.1. Schematic of the experimental setup. From Fjellgren (2007).

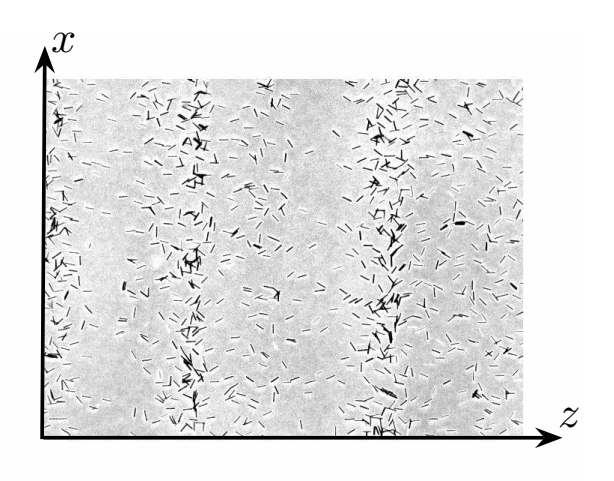


FIGURE A.2. Image illustrating that fibres form streamwise streaks.

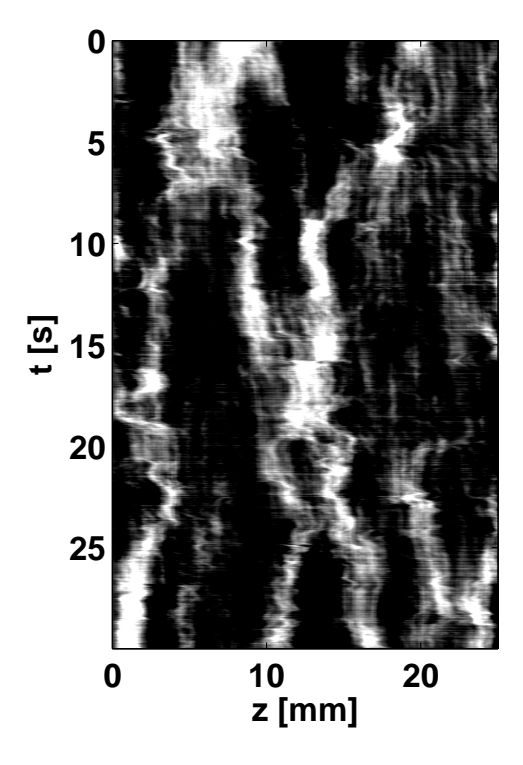


FIGURE A.3. The evolution of fibre streaks with time t. From Fjellgren (2007).

Acknowledgements

The EU-funded research project ECOTARGET is greatly acknowledged for funding this work. Bengt Ingeströms Stipendiefond and Erik Petersohns Minne are also acknowledged for funding international conference visits.

I would like to thank my supervisor Prof. Daniel Söderberg and my co-supervisor Dr. Fredrik Lundell for their guidance and support throughout the work. Prof. Henrik Alfredsson is acknowledged for first accepting me as a PhD-student at KTH Mechanics.

I would like to express my gratitude to Prof. Donald Koch for helping me with the theoretical part of this work and for, in my opinion, acting as an additional supervisor this last year. I have also received valuable comments on my work by Prof. Fritz Bark. Prof. Bo Norman is acknowledged for teaching me a little bit about papermaking, a field where my knowledge is still very limited. I am also thankful to Dr. Richard Holm for helping me out in the beginning of this work and for giving me a good start.

There are a number of people who have assisted me with practical issues necessary in order to get my experiments to work. Among these I would especially like to thank Börje Svensson, Christian Andersson, Lars Granlöf, Lennart Hermansson, Marcus Gällstedt, Sune Karlsson, Timmy Sigfrids and Ulf Landén.

Apart from the people already mentioned there are numerous people who I have discussed my work with over the years. I would especially like to acknowledge my friends and colleagues at STFI-Packforsk and KTH Mechanics. My intention was to mention you by name, but I realize that I will not be able to recall everybody that has meant something to me.

I would also like to mention the people I do not meet at work, but who have still meant a lot to me.

Throughout these last and earlier years I have received the most consistent support from my family. I would also like to thank all my friends. This includes

my corridor mates who have often been able to raise my spirit when I get home from work.

It is not my intention to leave anyone out of my acknowledgements. If you, the reader, feel that you have done something for me, I am sure you have.

Thank you!

February 2009, Stockholm

Allan Carlsson

References

- AIDUN, C. K. & KOVACS, A. E. 1995 Hydrodynamics of the forming section: the origin of nonuniform fiber orientation. *Tappi J.* **78** (11), 97–106.
- AIDUN, C. K., Lu, Y. & DING, E.-J. 1998 Direct analysis of particulate suspensions with inertia using the discrete Boltzmann equation. *J. Fluid Mech.* **373**, 287–311.
- ALTENBACH, H., NAUMENKO, K., PYLYPENKO, S. & RENNER, B. 2007 Influence of rotary inertia on the fiber dynamics in homogenous creeping flows. *Z. Angew. Math. Mech* 87 (2), 81–93.
- Anczurowski, E. & Mason, S. G. 1967 The kinetics of flowing dispersions. III. Equilibrium orientations of rods and discs (experimental). *J. Colloid Interface Sci.* 23, 533–546.
- ANCZUROWSKI, E. & MASON, S. G. 1968 Particle motions in sheared suspensions. XXIV. Rotation of rigid spheroids and cylinders. *Trans. Soc. Rheology* **12** (2), 209–215.
- Arlov, A. P., Forgacs, O. L. & Mason, S. G. 1958 Particle motions in sheared suspensions. IV General behaviour of wood pulp fibres. *Svensk Papperstidn*. **61** (3), 61–67.
- ASPLUND, G. & NORMAN, B. 2004 Fibre orientation anisotropy profile over the thickness of a headbox jet. *J. Pulp Paper Sci.* **30** (8), 217–221.
- Batchelor, G. K. 1970 Slender-body theory for particles of arbitrary cross-section in Stokes flow. *J. Fluid Mech.* 44, 419–440.
- BINDER, R. C. 1939 The motion of cylindrical particles in viscous flow. J. Appl. Phys. 10, 711–713.
- BLAKE, J. R. 1974 Singularities of viscous flow. Part II: Applications to slender body theory. J. Eng. Math. 8 (2), 113–124.
- Brenner, H. 1974 Rheology of a dilute suspension of axisymmetric Brownian particles. *Int. J. Multiphase Flow* 1, 195–341.
- Bretherton, F. P. 1962 The motion of rigid particles in a shear flow at low Reynolds number. *J. Fluid Mech.* **14**, 284–304.
- Brown, M. L. 2005 Dynamics of rigid fibres in a planar converging channel. PhD thesis, Georgia Institute of Technology, Atlanta.
- Carlsson, A. & Koch, D. L. 2009 Orbit drift of a slowly settling fiber in a wall-bounded shear flow. Manuscript in preparation.

- Carlsson, A., Lundell, F. & Söderberg, L. D. 2007 Fiber orientation control related to papermaking. *J. Fluids Eng.* **129** (4), 457–465.
- Carlsson, A., Lundell, F. & Söderberg, L. D. 2009a Evaluation of steerable filter for detection of fibres in flowing suspensions. Manuscript in preparation.
- Carlsson, A., Lundell, F. & Söderberg, L. D. 2009b Orientation of slowly sedimenting fibers in a flowing suspension near a plane wall. Manuscript in preparation.
- Carlsson, A., Söderberg, L. D. & Lundell, F. 2009c Fibre orientation near a wall of a headbox. Manuscript in preparation .
- Chwang, A. T. 1975 Hydrodynamics of low-Reynolds-number flow. Part 3. Motion of a spheroidal particle in quadratic flows. *J. Fluid Mech.* **72**, 17–34.
- Chwang, A. T. & Wu, T. Y.-T. 1974 Hydrodynamics of low-Reynolds-number flow. Part 1. Rotation of axisymmetric prolate bodies. *J. Fluid Mech.* **63** (3), 607–622.
- Chwang, A. T. & Wu, T. Y.-T. 1975 Hydrodynamics of low-Reynolds-number flow. Part 2. Singularity method for Stokes flows. *J. Fluid Mech.* **67**, 787–815.
- Cox, R. G. 1970 The motion of a long slender body in a viscous fluid. Part 1. General theory. J. Fluid Mech. 44, 791–810.
- Cox, R. G. 1971 The motion of a long slender body in a viscous fluid. Part 2. Shear flow. J. Fluid Mech. 45, 625–657.
- Dabros, T. 1985 A singularity method for calculating hydrodynamic forces and particle velocities in low-Reynolds-number flows. *J. Fluid Mech.* **156**, 1–21.
- DING, E.-J. & AIDUN, C. K. 2000 The dynamics and scaling law for particles suspended in shear flow with inertia. *J. Fluid Mech.* **423**, 317–344.
- EATON, J. K. & FESSLER, J. R. 1994 Preferential concentration of particles by turbulence. *Int. J. Multiphase Flow* **20**, 169–209.
- Fellers, C. & Norman, B. 1998 *Pappersteknik* (in Swedish). Royal Institute of Technology, Stockholm, Sweden.
- FJELLGREN, J. 2007 Fibre orientation in shear flows. Master thesis, Royal Institute of Technology, Stockholm, Sweden.
- FORGACS, O. L. & MASON, S. G. 1959a Particle motions in sheared suspensions. IX Spin and deformation of threadlike particles. J. Colloid Sci. 14, 457 472.
- FORGACS, O. L. & MASON, S. G. 1959b Particle motions in sheared suspensions. X Orbits of flexible threadlike particles. J. Colloid Sci. 14, 457 472.
- FREEMAN, W. T. & ADELSON, E. H. 1991 The design and use of steerable filters. *IEEE T. Pattern Anal.* **13** (9), 891–906.
- GAVELIN, G. 1990 Papperstillverkning (in Swedish). Sveriges Skogsindustriförbund.
- Gavze, E. & Shapiro, M. 1997 Particles in a shear flow near a solid wall: Effect of nonspherity on forces and velocities. *Int. J. Multiphase Flow* **23** (1), 155–182.
- GEER, J. 1976 Stokes flow past a slender body of revolution. J. Fluid Mech. $\mathbf{78}$ (3), 577–600.
- Goldsmith, H. L. & Mason, S. G. 1962 The flow of suspension through tubes. I. Single spheres, rods and discs. *J. Colloid Sci.* 17, 448–476.
- Harlen, O. G., Sundararajakumar, R. R. & Koch, D. L. 1999 Numerical simulations of a sphere settling through a suspension of neutrally buoyant fibres. J. Fluid Mech. **388**, 355–388.

- HARRIS, J. B. & PITTMAN, J. F. T. 1975 Equivalent ellipsoidal axis ratios of slender rod-like particles. *J. Coll. Interf. Sci.* **50** (2), 280–282.
- HERZHAFT, B. & GUAZZELLI, E. 1999 Experimental study of the sedimentation of dilute and semi-dilute suspensions of fibres. *J. Fluid Mech.* **384**, 133–158.
- Holm, R. & Söderberg, D. 2007 Shear influence on fibre orientation. *Rheol. Acta* 46, 721-729.
- HSU, R. & GANATOS, P. 1989 The motion of a rigid body in viscous fluid bounded by a plane wall. *J. Fluid Mech.* **207**, 29–72.
- HSU, R. & GANATOS, P. 1994 Gravitational and zero-drag motion of a spheroid adjacent to an inclined plane at low Reynolds number. J. Fluid Mech. 268, 267–292.
- Hyensjö, M. & Dahlkild, A. 2008 Study of the rotational diffusivity coefficient of fibres in planar contracting flows with varying turbulence levels. *Int. J. Multiphase Flow* **34**, 814–903.
- Hyensjö, M., Dahlkild, A., Krochak, P., Olson, J. & Hämäläinen, J. 2007 Modelling the effect of shear flow on fibre orientation anisotropy in a planar contraction. *Nordic Pulp Paper Res. J.* **22** (3), 376–383.
- JACOB, M. & UNSER, M. 2004 Design of steerable filters for feature detection using Canny-like criteria. IEEE T. Pattern Anal. 26 (8), 1007–1019.
- JEFFERY, G. B. 1922 The motion of ellipsoidal particles immersed in a viscous fluid. *Proc. Roy. Soc. London A* **102** (715), 161–179.
- JOHNSON, R. E. 1980 An improved slender-body theory for Stokes flows. J. Fluid Mech. 99, 411–431.
- JOUNG, C. G. & N. PHAN-THIEN, X. J. F. 2001 Direct simulation of flexible fibers. J. Non-Newtonian Fluid Mech. 99, 1–36.
- Keller, J. B. & Rubinow, S. I. 1976 Slender-body theory for slow viscous flow. J. Fluid Mech. 75, 705–714.
- Kerekes, R. J. & Schell, C. J. 1992 Characterization of fibre flocculation regimes by a crowding factor. *J. Pulp and Paper Sci.* **18** (1), J32–J38.
- Khayat, R. E. & Cox, R. G. 1989 Inertia effect on the motion of long slender bodies. J. Fluid Mech. 209, 435–462.
- KOCH, D. L. & SHAQFEH, E. S. G. 1989 The instability of a dispersion of sedimenting spheroids. *J. Fluid Mech.* **209**, 521–542.
- KOCH, D. L. & SHAQFEH, E. S. G. 1990 The average rotation rate of a fibre in the linear flow of a semidilute suspension. *Phys. Fluids A* **2**, 2093–2102.
- KRUSHKAL, E. M. & GALLILY, I. 1988 On the orientation distribution function of non-spherical aerosol particles in a general shear flow II. The turbulent case. *J. Aerosol Sci.* **19** (2), 197–211.
- LINDSTRÖM, S. B. & UESAKA, T. 2007 Simulation of the motion of flexible fibers in viscous fluid flow. *Phys. Fluids* **19** (113307), 1–16.
- Mackaplow, M. B. & Shaqfeh, E. S. G. 1998 A numerical study of the sedimentation of fibre suspensions. *J. Fluid Mech.* **376**, 149–182.
- MASON, S. G. 1954 Fibre motions and floccation. *Pulp Paper Mag. Can.* **55** (13), 96–101.
- MASON, S. G. & MANLEY, R. S. J. 1956 Particle motions in sheared suspensions:

- Orientation and interaction of rigid rods. *Proc. Roy. Soc. London A* **238** (1212), 117–131.
- MORETTI, P. M. & KAYS, W. M. 1965 Heat transfer to a turbulent boundary layer with varying free-stream velocity and varying surface temperature An experimental study. *Int. J. Heat Mass Transfer* 8, 1187–1202.
- Moses, K. B., Advani, S. G. & Reinhardt, A. 2001 Investigation of fiber motion near solid boundaries in simple shear flow. *Rheol. Acta* 40, 296–306.
- NORDSTRÖM, B. 2003a Effects of headbox tube design and flow rate on formation and other sheet properties in twin-wire roll forming. *Nordic Pulp Paper Res. J.* 18 (3), 296–302.
- NORDSTRÖM, B. 2003b Effects of pulp type and headbox design on anisotropy and other sheet properties in twin-wire forming. Nordic Pulp Paper Res. J. 18 (3), 288–295.
- NORMAN, B. & SÖDERBERG, D. 2001 Overview of forming literature 1990-2000. In Transactions of the 12th Fundamental Research Symposium, Oxford, Great Britain pp. 431–558.
- ODELL, M. H. & PAKARINEN, P. 2001 The complete fibre orientation control and effects on diverse paper properties. In *Tappi Papermakers Conference, Cincinnati.*
- Olson, J. 2002 Analytic estimate of the fibre orientation distribution in a headbox flow. *Nordic Pulp Paper Res. J.* 17 (3), 302–306.
- Olson, J., Frigaard, I., Chan, C. & Hämäläinen, J. P. 2004 Modeling a turbulent fibre suspension flowing in a planar contraction: The one-dimensional headbox. *Int. J. Multiphase Flow* **30**, 51–66.
- Olson, J. & Kerekes, R. 1998 The motion of fibres in turbulent flow. J. Fluid Mech. 17, 47–64.
- Parsheh, M. 2001 Flow in contractions with application to headboxes. PhD thesis, Royal Institute of Technology, Stockholm, Sweden.
- Parsheh, M., Brown, M. L. & Aidun, C. K. 2005 On the orientation of stiff fibres suspended in turbulent flow in a planar contraction. *J. Fluid Mech.* **545**, 245–269.
- Parsheh, M., Brown, M. L. & Aidun, C. K. 2006a Investigation of closure approximations for fiber orientation distribution in contracting turbulent flow. J. Non-Newtonian Fluid Mech. 136, 38–49.
- Parsheh, M., Brown, M. L. & Aidun, C. K. 2006b Variation of fiber orientation in turbulent flow inside a planar contraction with different shapes. *Int. J. Multiphase Flow* **32**, 1354–1369.
- Petrich, M. P., Koch, D. L. & Cohen, C. 2000 An experimental determination of the stress-microstructure relationship in semi-concentrated fiber suspensions. J. Non-Newtonian Fluid Mech. 96, 101–133.
- Petrie, C. J. S. 1999 The rheology of fibre suspensions. *J. Non-Newtonian Fluid Mech.* 87, 369–402.
- PITTMAN, J. F. T. & KASIRI, N. 1992 The motion of rigid rod-like particles suspended in non-homogeneous flow fields. *Int. J. Multiphase Flow* **18** (6), 1077–1091.

- Powell, R. L. 1991 Rheology of suspensions of rodlike particles. J. Stat. Phys. 62, 1073–1094.
- Pozrikidis, C. 2005 Orbiting motion of a freely suspended spheroid near a plane wall. J. Fluid Mech. **541**, 105–114.
- QI, D. 2007 A new method for direct simulations of flexible filament suspensions in non-zero Reynolds number flows. *Int. J. Numer. Meth. Fluids* **54**, 103–118.
- QI, D. & Luo, L. S. 2002 Transitions in rotations of a nonspherical particle in a threedimensional moderate Reynolds number Couette flow. Phys. Fluids 14 (12), 4440–4443.
- QI, D. & Luo, L. S. 2003 Rotational and orientational behaviour of threedimensional spheroidal particles in Couette flows. J. Fluid Mech. 477, 201–213.
- RAHNAMA, M., KOCH, D. L. & SHAQFEH, E. S. G. 1995 The effect of hydrodynamic interaction on the orientation distribution in a fiber suspension subject to simple shear flow. *Phys. Fluids* **7**, 487–506.
- Ross, R. F. & KLINGENBERG, D. J. 1997 Dynamic simulation of flexible fibers composed of linked rigid bodies. *J. Chem. Phys.* **106** (7).
- Russel, W. B., Hinch, E. J., Leal, L. G. & Tiefenbruck, G. 1977 Rods falling near a vertical wall. *J. Fluid Mech.* 83, 273–287.
- Samuelsson, L. G. 1963 Measurement of the stiffness of fibres. *Svensk Papperstid*. **66** (8), 541–546.
- Schlichting, H. 1979 Boundary layer theory, 7th edn, 166–168. McGraw-Hill.
- SKJETNE, P., ROSS, R. F. & KLINGENBERG, D. J. 1997 Simulation of single fiber dynamics. J. Chem. Phys. 107 (6).
- STOCKIE, J. M. & GREEN, S. I. 1998 Simulating the motion of flexible pulp fibres using the immersed boundary method. *J. Comp. Phys.* **147**, 147–165.
- Stover, C. A. & Cohen, C. 1990 The motion of rodlike particles in the pressure-driven flow between flat plates. *Rheol. Acta* 29, 192–203.
- Stover, C. A., Koch, D. L. & Cohen, C. 1992 Observations of fibre orientation in simple shear flow of semi-dilute suspensions. *J. Fluid Mech.* 238, 277–296.
- Subramanian, G. & Koch, D. L. 2005 Inertial effects on fibre motion in simple shear flow. *J. Fluid Mech.* **535**, 383–414.
- Subramanian, G. & Koch, D. L. 2006 Inertial effects on the orientation of nearly spherical particles in simple shear flow. *J. Fluid Mech.* **557**, 257–296.
- Sundararajakumar, R. R. & Koch, D. L. 1997 Structure and properties of sheared fiber suspensions with mechanical contacts. *J. Non-Newtonian Fluid Mech.* **73**, 205–239.
- Talamelli, A., Fornaciari, N., Westin, K. J. A. & Alfredsson, P. H. 2002 Experimental investigation of streaky structures in a relaminarizing boundary layer. J. Turbulence 3 (018).
- Tam Doo, P. A. & Kerekes, R. J. 1981 A method to measure fiber flexibility. *Tappi* **64** (3), 113–116.
- Tam Doo, P. A. & Kerekes, R. J. 1982 The flexibility of wet pulp fibres. *Pulp Paper Can* 83 (2), 37–41.
- Taylor, G. I. 1923 The motion of ellipsoidal particles in a viscous fluid. *Proc. Roy. Soc. London A* $\bf 103$, 58–61.

- TILLETT, J. P. K. 1970 Axial and transverse Stokes flow past slender axisymmetric bodies. J. Fluid Mech. 44, 401–417.
- TORNBERG, A. K. & SHELLEY, M. J. 2004 Simulating the dynamics and interactions of flexible fibers in Stokes flows. *J. Comp. Phys.* **196**, 8–40.
- TREVELYAN, J. & MASON, S. G. 1951 Particle motions in sheared suspensions I. Rotations. J. Colloid Sci. 6, 354–367.
- Ullmar, M. 1998 On fibre alignment mechanisms in a headbox nozzle. Licentiate thesis, Royal Institute of Technology, Stockholm, Sweden.
- Wang, G., Yu, W. & Zhou, C. 2006 Optimization of the rod chain model to simulate the motions of a long flexible fiber in simple shear flow. *Eur. J. Mech. B Fluids* **25**, 337–347.
- Warnack, D. & Fernholz, H. H. 1998 The effects of a favourable pressure gradient and of the Reynolds number on an incompressible axisymmetric turbulent boundary layer. Part 2. The boundary layer with relaminarization. *J. Fluid Mech.* 359, 357–381.
- Yamamoto, S. & Matsuoka, T. 1993 A method for dynamic simulation of rigid and flexible fibers in a flow field. J. Chem. Phys. 98 (1).
- Yang, S.-M. & Leal, L. G. 1984 Particle motion in Stokes flow near a plane fluid-fluid interface. Part 2. Linear shear and axisymmetric straining flows. *J. Fluid Mech.* 149, 275–304.
- ZIRNSAK, M. A., Hur, D. U. & Boger, D. V. 1994 Normal stresses in fibre suspensions. J. Non-Newtonian Fluid Mech. 54, 153–193.

Part II

Papers

Paper 1

Fiber orientation control related to papermaking

By Allan Carlsson[†], Fredrik Lundell[†] & L. Daniel Söderberg[†], [‡]

 $^\dagger Linné$ Flow Centre, KTH Mechanics, SE - 100 44 Stockholm, Sweden $^\dagger STFI\text{-Packforsk AB, SE}$ - 114 86 Stockholm, Sweden

Published in Journal of Fluids Engineering, 2007, Vol. 129 (4), 457-465. Corrigendum is accepted for publication in J. Fluids Eng. and is incorporated into this text.

The orientation of fibers suspended in a shear flow flowing over a solid wall has been studied experimentally. The possibility to control this orientation with physical surface modifications, ridges, has also been studied. The fiber suspension was driven by gravity down a slightly inclined glass plate and a CCD-camera was used to capture images of the fibers in the flow. Image analysis based on the concept of steerable filters extracted the position and orientation of the fibers in the plane of the image. From these data, the velocity of the fibers was determined. When viewing the flow from the side, the velocity of the fibers at different heights was measured and found to agree with the theoretical solution for Newtonian flow down an inclined plate. Moving the camera so that the flow was filmed from below, the orientation and velocity of fibers in the plane parallel to the solid surface was determined. The known relationship between the velocity and the wall normal position of the fibers made it possible to determine the height above the plate for each identified fiber. Far away from the wall, the fibers were aligned with the flow direction in both cases. In a region close to the smooth plate surface the fibers oriented themselves perpendicular to the flow direction. This change in orientation did not occur when the surface structure was modified with ridges.

1. Introduction

The present work is part of a larger undertaking aimed at understanding and controlling the flow physics involved in papermaking. When paper is produced, a fiber suspension consisting of cellulose fibers suspended in water is used. The suspension, with a mass concentration typically below 1%, enters a nozzle, usually called a headbox, through a pipe with a diameter of approximately 800 mm, Fellers & Norman (1998). The main purpose of the headbox is to

distribute the suspension evenly across one or between two permeable bands called wires. To do this the pipe-flow entering the headbox is transformed to a jet with an approximate height of 10 mm and a width of about 10 m. The mechanical properties of the produced paper sheet are strongly coupled to the fiber orientation. Due to the contraction of the headbox, fibers tend to align in the flow direction. This orientation anisotropy is also reflected in the final product.

In order to damp out large-scale velocity fluctuations in the headbox, which can result in a bad formation of the paper, i.e. a variation in local mass distribution or basis weight, flexible flow dividers are often implemented in the headbox. These are fixed at the entrance to the nozzle contraction and allowed to adjust according to the flow field. The width of these flow dividers are the same as the width of the nozzle. The flow dividers will henceforth be called lamellas. At the surfaces of the lamellas the no-slip condition is valid, i.e. the velocity of the fluid relative to the surfaces is zero. As a result thin shear layers of fluid, i.e. boundary layers, will form along the lamella surfaces, where the velocity goes from zero at the surfaces to the velocity of the main stream further out. The aim of the present study is to investigate the physics controlling fiber orientation in a boundary layer close to a solid wall, aiming at understanding how the lamellas influence the fiber orientation and ultimately the properties of the final paper product. It is also of interest to investigate the possibility to use the lamellas as means of controlling the fiber orientation by modifying the structure of the lamella surfaces.

In order to interpret the results of the present study, the concept of Jeffery orbits will be used, i.e. the motion of a solitary ellipsoid suspended in a laminar simple shear flow. The equations of motion for the ellipsoid has been solved theoretically by Jeffery (1922) and the resulting expressions, frequently referred to as Jeffery's equations, are

$$\dot{\phi} = -\frac{\dot{\gamma}}{r_e^2 + 1} (r_e^2 \sin^2 \phi + \cos^2 \phi) \tag{1}$$

$$\dot{\theta} = \left(\frac{r_e^2 - 1}{r_e^2 + 1}\right) \frac{\dot{\gamma}}{4} \sin 2\phi \sin 2\theta,\tag{2}$$

where ϕ is the angle of the particle projection in the flow-gradient plane with respect to the streamwise direction, figure 1. The angle of the particle with respect to the vorticity axis is defined as θ . The aspect ratio, *i.e.* the length to diameter ratio of the ellipsoid, is denoted r_e and $\dot{\gamma}$ is the shear rate. The dots over the two angles ϕ and θ , represent differentiation with respect to time. The ellipsoid will remain in its initial orbit, which is defined by the initial conditions. The motion is periodic with a period

$$T = \frac{2\pi}{\dot{\gamma}} \left(\frac{r_e^2 + 1}{r_e} \right). \tag{3}$$

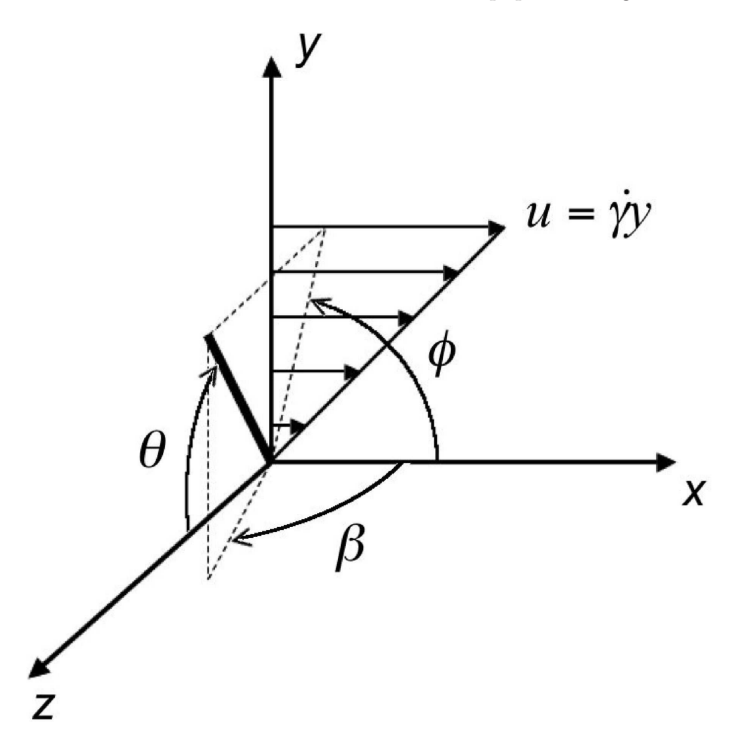


Figure 1. Coordinate system.

Integration of equations (1) and (2) with respect to time yields

$$\tan \phi = \frac{1}{r_e} \tan \left(-\dot{\gamma} t \frac{r_e}{r_e^2 + 1} + \tan^{-1} (r_e \tan \phi_0) \right)$$

$$\tan \theta = \frac{C r_e}{(r_e^2 \sin^2 \phi + \cos^2 \phi)^{1/2}},$$
(5)

$$\tan \theta = \frac{Cr_e}{(r_e^2 \sin^2 \phi + \cos^2 \phi)^{1/2}},\tag{5}$$

where C is the so called orbit constant and ϕ_0 is the initial value of ϕ .

Even though the original derivation of Jeffery's equations relied on the assumption of ellipsoidal particles, it has been shown that it is possible to extend Jeffery's equations to be valid for any body with a fore-aft symmetry, provided that an equivalent aspect ratio is used, Bretherton (1962). In particular, the equivalent aspect ratio for a cylindrical fiber is

$$r_e = 1.24r_p(\ln r_p)^{-1/2},$$
 (6)

where r_p is the aspect ratio of the cylindrical fiber and r_e is the equivalent aspect ratio to be used in Jeffery's equations, see Cox (1971) .

Some examples of Jeffery orbits are shown in figure 2. The orbits are calculated for an equivalent aspect ratio $r_e = 8.17$, which corresponds to a

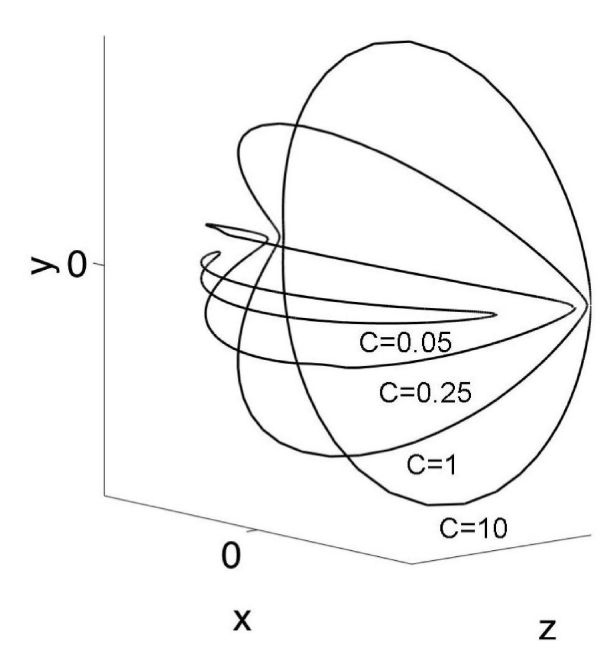


FIGURE 2. Jeffery orbits for different values of the orbit constant C and $r_e=8.17$.

cylindrical fiber with aspect ratio 10 as used in the present study. The flow is in the x-direction and the shear is in the y-direction. Four different orbits are shown in figure 2. The orbits are shown as the path of a fiber end-point. For high values of C the fiber spend most of its time oriented close to the flow direction. Periodically, with a period of T/2, it flips over 180 degrees around the vorticity axis. As the value of C is lowered the amplitude of the motion in the y-direction decreases. For very low values of C the fiber is almost parallel to the xz-plane, oriented perpendicular to the flow direction.

Jeffery's equations have been verified by several researchers, including Moses, Advani & Reinhardt (2001), Taylor (1923) and Binder (1939), but do not account for fiber-fiber interactions or wall effects. The wall effect has been investigated both experimentally by Moses $et\ al.$ and theoretically by Pozrikidis (2005). For elongated particles, a good agreement of Jeffery's equations was found, in the study by Moses $et\ al.$, for distances from the wall larger than one fiber-length, whereas an increased rate of rotation was found closer to the wall. The spatial orbit was not considerably changed.

At higher concentrations, it has been shown by Koch & Shaqfeh (1990) that the correction to the $O(\dot{\gamma})$ rotation rate is $O(\dot{\gamma}/\ln(1/c_v))$ where c_v is the

volume fraction of the fibers. For a concentration of 1% this correction is O(20%).

Initially in this paper, the experimental setup and evaluation methods are described followed by a discussion regarding why the present experiments, performed at low velocities in a highly viscous fluid, are relevant for papermaking. Thereafter the results are presented and discussed followed by conclusions. In the paper we present measurements of the previously discarded fiber orientation in the xz-plane, and in particular the effect of a wall including the possibility to manipulate the orientation by modifying the surface structure of the wall.

2. Experimental setup & analyzing techniques

To create a well-defined shear flow a fiber suspension was allowed to flow down a slightly inclined glass plate. To visualise the flow a charge-coupled device (CCD)-camera has been used, and by analyzing the captured images the velocity and orientation of the fibers in the shear flow can be obtained. Below, the flow loop, liquid and fibers are described. Thereafter the image analysis methodology is introduced, which is performed in two steps: (i) detection of the position and orientation of fibers in an image and (ii) determination of the velocity from a triplet of consecutive images. The flow in the apparatus is verified by comparing measured velocity profiles of the fibers with the theoretical profile.

2.1. Experimental setup

The experimental setup, illustrated in figure 3, consists of a $(1200 \times 400) \text{ mm}^2$ glass plate with a thickness of 6 mm. A pivoting acrylic frame with for-aft reservoirs, not shown in the figure, supports the plate. A membrane pump (Dominator P30-ANN) is used to transfer the fluid between the reservoirs. By placing an insert on the glass plate the flow is given an inlet contraction followed by a parallel section of length 1050 mm and width 100 mm. The contraction stretches over a length of 150 mm and has a contraction ratio of four. Due to the acceleration in the contraction the fibers align themselves with the flow direction.

Experiments have been performed using two different surfaces. The first is a smooth surface and the second is a structured surface with ridges oriented 30 degrees counter-clockwise to the flow direction. The ridges were machined in four (100 x 100) mm² acrylic plates of height 6 mm. These plates covered the region from x=400 mm to x=800 mm. The position and structure of the ridges is illustrated in figure 4, where H=0.5 mm. In the case of the smooth surface a (1200 x 100) mm² acrylic plate of height 6 mm is placed in the flow section on top of the glass plate in order to ensure that the flow situation was similar to the case with ridges.

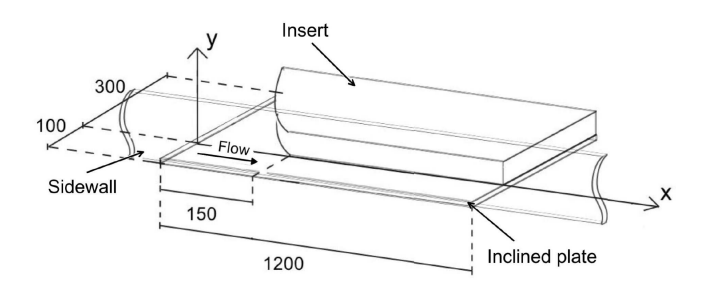


FIGURE 3. Schematic figure of the test section. All lengths are given in mm.

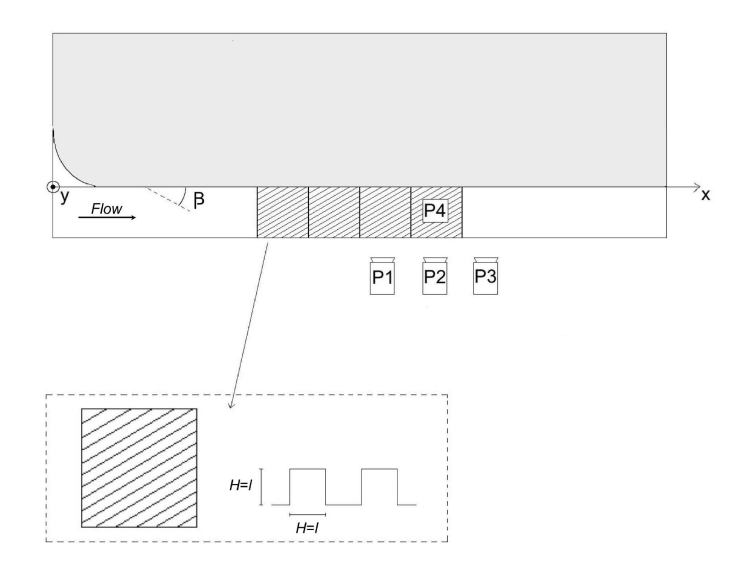


FIGURE 4. Schematic figure illustrating the camera positions for the velocity profile measurements (P1, P2 and P3) and for the fiber orientation studies P4.

2.2. Flow situation

The theoretical velocity profile for a Newtonian fluid flowing down an inclined plate is given by

$$u = \frac{g}{2\nu}y(2h - y)\sin\alpha,\tag{7}$$

where g is the gravitational constant, ν is the kinematic viscosity of the fluid, h is the fluid film thickness and α is the inclination of the plate with respect to

the horizontal, see for instance Acheson (1990). The distance from the wall, y in equation (7), stretches from y=0 at the wall to the surface of the liquid film y=h. Equation (7) is thus a parabolic expression where the velocity is zero at the wall to gradually increase with the distance to the wall. The highest velocity is found at y=h, where $u=U_s$.

In the experiments a tilt angle of $\alpha=2.60\pm0.1^\circ$ caused the suspension to form a liquid film along the plate with a thickness of 17.0 ± 0.2 mm. The film thickness was measured to be constant throughout the section between x=650 mm and x=850 mm. It can thus be established that there was no global acceleration in the flow. The Reynolds number, based on the film thickness and the velocity at the surface of the film, is defined as

$$Re = \frac{U_s h}{\nu}.$$
 (8)

For the highly viscous flow in the experiments Re ≈ 8 .

2.3. Fiber suspension

The liquid containing the fibers was a mixture of glycerine and polyethylenegly-col (PEG-400). The temperature of the suspension was 295.5 ± 0.5 K throughout the measurements. For this temperature the kinematic viscosity of the liquid was measured to $\nu = (383 \pm 10) \cdot 10^{-6}$ m²/s and the density to $\rho_f = 1210 \pm 15$ kg/m³.

Cellulose acetate fibers were suspended in the liquid. The length of the fibers was l=0.5 mm and the diameter was approximately $d\approx 70~\mu\mathrm{m}$. The density of the fibers was approximately $\rho_p=1300~\mathrm{kg/m^3}$. Since the density of the fibers is higher than the density of the liquid, the fibers will sediment slowly when suspended in the liquid. The suspension was dilute with a volume fraction of fibers $c_v=0.004$. This concentration can be expressed as $nl^3\approx 0.25$, which is the number of fibers within a volume l^3 (n is the number density of fibers).

The index of refraction (IR) of the liquid was approximately matched to that of the fibers and the IR of the liquid was measured to $n=1.466\pm0.002$. IR matching is a frequently used tool in multiphase flows and has been used in several previous studies of fiber suspensions, see Iso, Koch & Cohen (1995), Petrich, Koch & Cohen (2000), Holm (2005) and Herzhaft & Guazzelli (1999). In order to visualise the fibers 4% were dyed black.

2.4. Measuring and analyzing method

In order to investigate the behaviour of the suspended fibers, the fibers are visualized with a CCD-camera, which captures images from underneath the flow. Image analysis is used to find the orientation and the velocity of the fibers. Furthermore the velocity profile of the fibers is measured and found to coincide well with the theoretical velocity profile defined in equation (7), which

makes it possible to determine the distance from the wall of individual fibers based on their velocity.

2.4a. Visualization. The CCD-camera (SONY DFW-X700, 1024x768 pixels) visualising the fibers was mounted underneath the flow at x=750 mm (camera position P4 in figure 5) in order to capture images for orientation studies. To find the velocity profile of the fibers the camera was also mounted at the side of the flow, camera position P1–P3 in figure 5. A stroboscope (Drelloscop 200) was synchronized to the CCD-camera in order to illuminate the field of view. A typical image captured by the camera is shown in figure 6.

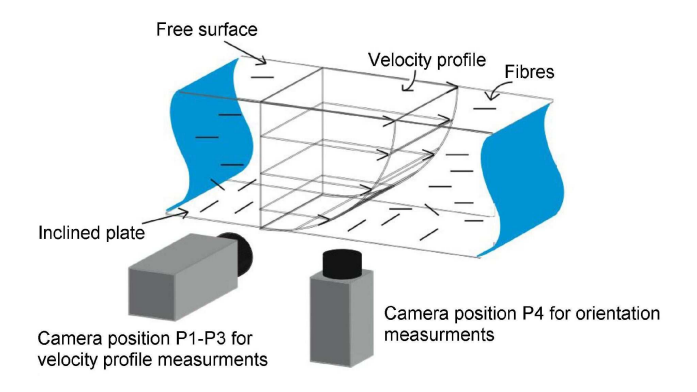


FIGURE 5. Schematic figure illustrating the flow situation with the camera positions P1–P3 and P4.

2.4b. Image analysis. To find the position and orientation of the individual fibers in the captured images a second order ridge detector is used Jacob & Unser (2004). The correlation between a captured image and the filter in figure 7, is calculated. A high value of the correlation at a certain position in an image indicates that there is a local similarity of the fiber and the filter at that position. The filter is within the class of steerable filters, which means that the correlation of the filter, rotated to a certain angle, with the image can be found through a linear combination of a limited amount of correlations of filters with the image. Thus, it is not necessary to perform correlations for a large number of rotated versions of the filter with the image. For the particular filter used, only three correlations are performed in order to find the angle of the filter that will result in the highest correlation of the filter for each position in the image.

2.4c. Particle tracking velocimetry. To find the velocity of the fibers at a certain time, three consecutive images were captured with a frequency of $f = \frac{1}{2}$

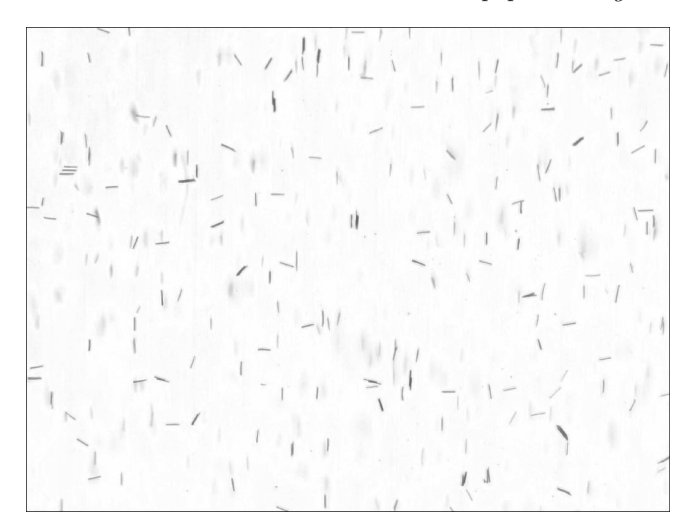


FIGURE 6. Image captured underneath of the flow for orientation studies (camera position P4).

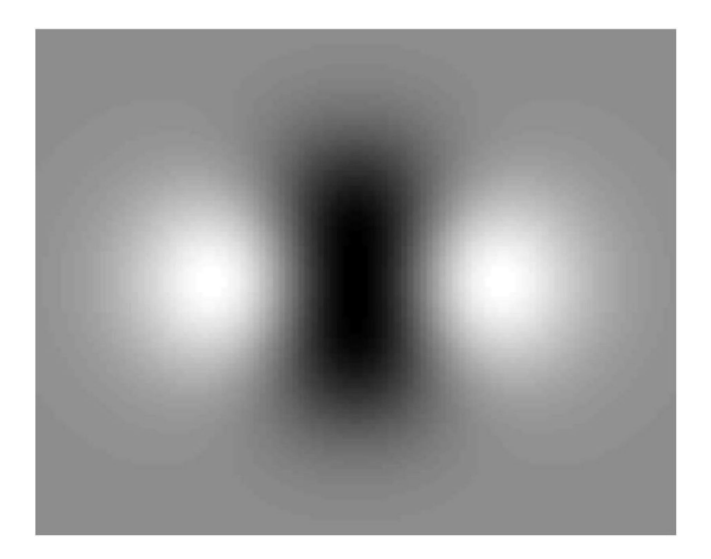


FIGURE 7. Filter used to find the orientation of the fibers.

 5.13 ± 0.05 Hz. Between every set of three images a delay of $T_s = 12~s$ was implemented. This will give the majority of the fibers an opportunity to pass the field of view, which means that the following triplet of images will be statistically independent. This aspect will be returned to below. Each measuring series lasted for approximately one hour, resulting in 900 images to analyze.

Based on the position of the fibers in the images the velocity can be found through a Particle Tracking Velocimetry (PTV) algorithm that locates the individual fibers in subsequent images. The principal idea of the algorithm is to start from the position of a fiber in an image and search for fibers in the flow direction in a narrow region downstream of this position in the following (second) image. The velocity is calculated for all the candidate fibers found in the prescribed region of the second image.

Based on the calculated velocities, the positions in the narrow region in the third image, where the fibers would be located if they continued with the same velocity, are calculated. If a fiber is located at any of the proposed positions in the third image it is considered to be the same fiber as the original fiber in the first image. This method is not flawless since it is possible for three different fibers, all travelling with different velocities, to result in a match in the algorithm. Analyzing longer image sequences could reduce this problem. This would however decrease the maximum velocity that can be detected. Decreasing the width of the region where the fibers have to be found in the second image, as well as decreasing the area where the fiber has to be found in the third image, can also reduce the error. In the studies performed here, only three images have been used to track the fibers and incorrect matches do appear occasionally, as will be seen in the velocity profile measurements.

2.4d. Permissible regions for PTV. In order to ensure statistically independent samples of the orientation and velocity of fibers, it is necessary that each fiber is sampled only once. This is achieved by limiting the region where the fibers have to be found in the first image. The permissible region is shown in figure 8 where a typical image is shown in (a) and the region where fibers have to be found for different velocities is shown in (b). This region is defined so that (i) detection in two subsequent sets of three images is avoided (for low velocities) and (ii) the fiber is still located in the field of view when the third image is captured. In order for a fiber to be detected it has to be located below the solid line. For fibers travelling at velocities lower than $\Delta X/T_s$, where ΔX is the physical length of the image in the flow direction, the slope of the solid line is defined by the period T_s . Fibers located in this region travel too slow to pass the field of view in the period T_s . Thus, if a fiber is located above the solid line, it should have been found in the preceding set of three images. Hence, fibers with velocities smaller than $\Delta X/T_s$, located above the solid line, are not considered.

The second effect that has to be taken into account is that the region where a fiber can be detected decreases with an increased velocity of the fibers. The largest detectable velocity of a fiber is $\Delta X f/2$. For a fiber travelling with this velocity to be detected it has to be located sufficiently far upstream in the first image, so that it can be found in the two subsequent images. For fibers travelling at velocities larger than $\Delta X/T_s$, the slope of the solid line in figure

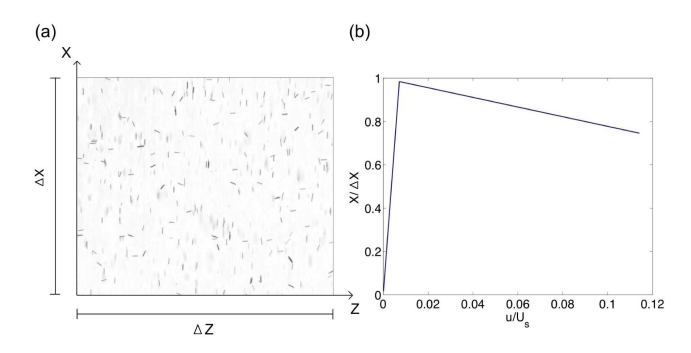


FIGURE 8. Region in image where fibers can be detected.

8(b) is thus defined by the period 2/f. Fibers located above the solid line in the first image will leave the field of view, before the third image is captured. This effect is also present at velocities smaller than $\Delta X/T_s$, although since $2/f << T_s$, the slope of the solid line does not change substantially.

2.5. Velocity profile of fibers

To verify that there was no acceleration in the flow and that the velocity profile was fully developed, the camera was mounted at the side of the flow, camera positions P1-P3 (x = 650, 750 and 850 mm), see figure 4 and 5. The measurements in this configuration were performed on the smooth surface at an early stage of this work in order to validate the setup and therefore, the fiber suspension was not identical to the suspension used for the orientation studies. The length and diameter of the fibers was l=2 mm and $d\approx 70~\mu \text{m}$ respectively and the concentration of fibers was $nl^3 \approx 0.15$. The liquid mixture was essentially the same as mentioned earlier. The results from these measurements are shown in figure 9, where the velocities of individual fibers are marked with dots. The solid line in the figure is the theoretical velocity profile, defined by equation (7). The velocity has been normalized with the surface velocity of the liquid film U_s and the distance from the wall is normalized with the film thickness h. The velocities of most of the fibers found coincide very well with the theoretical profile. However, a few of the dots deviate substantially from the theoretical profile, although the amount of these dots is very small compared to the amount of fibers coinciding with the profile. It is believed that the deviating dots are a result of incorrect matches in the particle-tracking algorithm. If the deviating dots are disregarded it can be concluded that there is a strong correlation between the velocity and the distance from the wall of the fibers. This makes it possible to convert the determined velocity of the fibers to a distance from the wall.

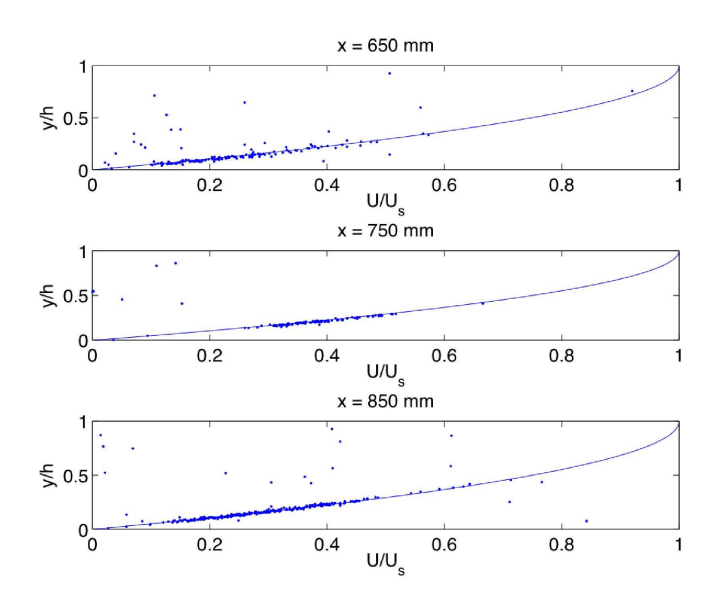


FIGURE 9. Velocity profiles measured at three different position along the x-axis (camera position P1–P3).

3. Relevance for paper manufacturing

In a paper machine, the jet leaving the headbox can reach velocities of more than 30 m/s. A natural question that arises is whether the fiber dynamics in the present experiments has any relevance for the fibers flowing over the lamellas in a headbox. The experiments are performed at a 400 times higher viscosity and 1/200 of the velocity as compared to the situation in the headbox. This issue will be discussed in terms of boundary layers and the forces exerted on a fiber in the headbox flow and turbulent/laminar retransition.

3.1. Fibers in the headbox boundary layers

Below, a rough estimation of the force exerted on a fiber in the headbox boundary layer will be compared with the torque in the present experiments. An estimation of the velocity profiles along the lamellas in the headbox is given by the similarity solution for flow in a two-dimensional convergent channel, see Schlichting (1979). The velocity u is given by

$$\frac{u}{U_e} = 3 \tanh^2 \left(\frac{\eta}{\sqrt{2}} + 1.146\right) - 2,$$
 (9)

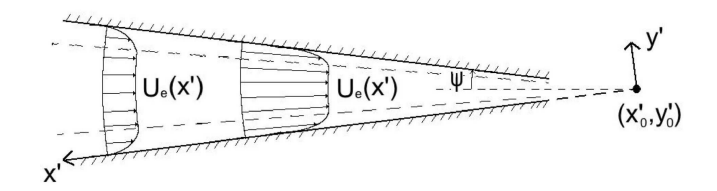


FIGURE 10. Two-dimensional convergent channel.

where U_e is the velocity of the fluid outside the boundary layer and η is defined as

$$\eta = y' \sqrt{\frac{U_e}{-(x' - x_0')\nu}}. (10)$$

The definitions of the coordinates x' and y' are shown in figure 10.

 U_e will grow as the fluid travels downstream due to the contraction. The acceleration will also force the boundary layer thickness to decrease in the downstream direction. Lamellas implemented in a headbox typically ends about 100 mm upstream from the outlet of the headbox. At this position the boundary layer thickness will be of the order of 1 mm. At a distance from the solid surface of 0.5 mm, *i.e.* one fiber length, the shear rate is about 1000 s⁻¹. For comparison, the shear rate at the same distance from the surface in the experiments is about 20 s⁻¹.

The torque on the fibers is estimated under the assumption that they are standing still, straight up from the wall. This assumptions is very rough and the following analysis should only be seen as an order of magnitude analysis. If one wants to compare the motions of free fibers, careful analysis at the correct particle Reynolds numbers has to be performed. Attempts in this direction are reported in the literature, Subramanian & Koch (2005), and show that a fairly small Reynolds number can have a substantial effect on the fiber motion, but the complete description is yet to be established.

The force on a fiber standing straight up is estimated as follows. The velocity of the fluid surrounding the fiber is assumed to be linear with a shear rate $\dot{\gamma}$ and thus forms a linear velocity field $U=(a+0.5)\dot{\gamma}l$ along the fiber. The coordinate a has its origin in the center of mass of the fiber and is directed along the fiber with value -0.5 and 0.5 at the fiber center points, respectively.

This velocity field gives rise to a force distribution on the fiber which can be estimated by integrating the local force per unit length on the fiber from one end to the other.

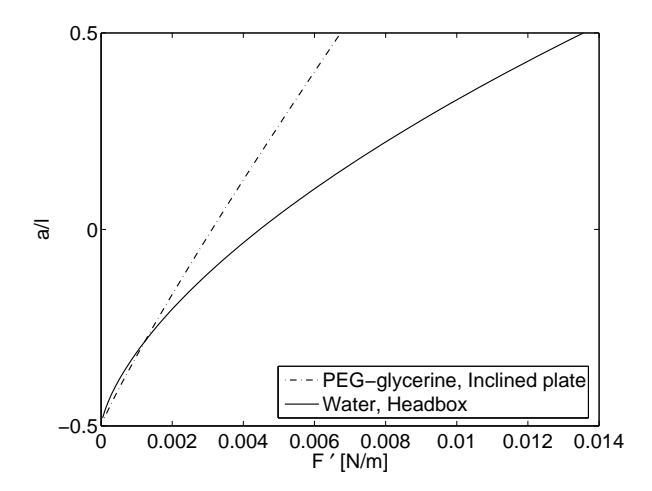


FIGURE 11. Estimated force distribution along fibers standing straight up from the wall in the experiments $(-\cdot -)$ and in a headbox (-).

In the experimental configuration the maximum Re_d is 0.001. For $\text{Re}_d = Ud/\nu$ up to approximately 1, the force is given by White (1991)

$$F' = \frac{\rho U^2}{2} \frac{8\pi d}{\text{Re}_d(0.5 - \Gamma + \ln(8/\text{Re}_d))},$$
(11)

where F' is the force per unit length and $\Gamma=0.57722...$ is the Euler-Mascheroni constant. In the headbox the largest Re_d is about 25 and the force distribution is estimated by

$$F' = \frac{\rho U^2}{2} dC_d \tag{12}$$

where C_d is given by $C_d = 1 + 10.0/(\text{Re}_d^{2/3})$, a correlation valid up to $\text{Re}_d \approx 250000$, see White.

The particle Reynolds numbers, $\dot{\gamma}l^2/\nu$, are typically 0.01 and 250 in the present experiments and a paper machine, respectively. Thus, inertial effects are considerable in the industrial application and the fibers cannot be expected to perform Jeffery orbits. Nevertheless, it will be shown below that the forces acting on a fiber during rotation can be expected to be of the same order.

By using equations (11) and (12) and letting Re_d and U vary along the fiber, the force per unit length along the fiber can be calculated. The resulting force distribution for the present setup and in a paper machine is presented in figure 11. The lines are based on a velocity of the outgoing jet of 15 m/s, jet height of 10 mm and a half contraction angle $\psi = 7^{\circ}$ (see figure 10). In spite of

the large differences in the shear rate and the viscosity between the performed experiments and the situation in the headbox, the torque that the fibers will be subjected to, based on the assumption that the fiber is held fixed in the gradient direction, will only differ by a factor of 2.

3.2. Turbulence in headbox

The flow in a headbox is normally considered to be turbulent. However, a turbulent boundary layer can return to laminar-like conditions if it is subjected to a strong acceleration. The acceleration is usually measured by the non-dimensional acceleration parameter

$$K = \frac{2\nu \tan \psi}{q},\tag{13}$$

where q is the total flow rate per unit width in the convergent channel. Experiments performed on a turbulent boundary layer for various rates of the freestream acceleration show that an apparent re-transition to a laminar boundary layer was found by Moretti & Kays (1965) for $K > 3.5 \cdot 10^{-6}$. Another experimental study, by Parsheh (2001), of a flat-plate fully turbulent boundary layer subjected to an acceleration in a two-dimensional contraction showed that at $K \approx 3.1 \cdot 10^{-6}$, the velocity profile approached a self-similar laminar state at the end of the contraction. As seen in equation (13) K will depend on the flow rate in the headbox as well as the contraction ratio, defined by the angle ψ . In a papermachine, K is typically between $5 \cdot 10^{-7}$ and $6 \cdot 10^{-6}$. It is thus possible that the boundary layers will be re-laminarized towards the end of the nozzle for some configurations. To the authors knowledge, all studies performed concerning the re-laminarization of boundary layers are performed on one-phase flows, i.e. no particles have been suspended in the fluid.

4. Results & Discussion

Close to a solid surface it is not possible for fibers to perform all the Jeffery orbits illustrated in figure 2, since they would hit the wall when doing so if they are to close to the solid surface. For the case of $\beta = 0$ ($C \to \infty$), *i.e.* fibers aligned with the flow, it has been shown that fibers can interact irreversibly with the wall and "pole-vault" up to a position where the Jeffery orbit is possible to perform, Stover & Cohen (1990).

In the following, the restraint given by the Jeffery orbit will be examined further. This will be followed up with experimental data of the orientation of fibers in the xz-plane. In addition to the orientation of the fibers, their velocities are determined. The velocity of the fibers, together with the known velocity profile, can then be used to determine the distance from the wall to the fiber. A strong effect on the orientation is found for the smooth surface but not for the one with ridges. The coordinate system used in the presentation of the results is defined in figure 3 and 4.

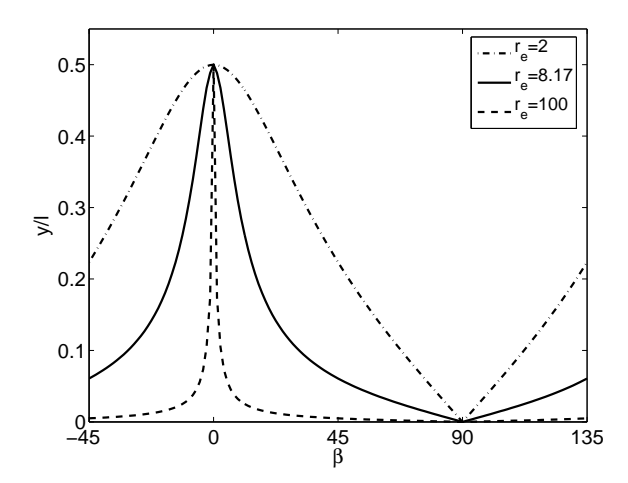


FIGURE 12. Minimum distance from the wall where fibers performing Jeffery orbits can occur for different orientations and aspect ratios of the fibers.

4.1. Jeffery orbits close to the wall

For distances more than half a fiber length away from the wall small effects of the presence of the wall have been seen. In this region most of the fibers keep their initial orientation, i.e. aligned with the flow. It was observed that fibers spend most of their time aligned with the flow and occasionally flip 180 degrees around the vorticity axis. Although no measurements have been carried out in order to determine the periodicity of the motion, it appears as the fibers perform a motion similar to Jeffery orbits with a high value of C, as shown in figure 2. When $C \to \infty$ the amplitude of the orbit, in the y-direction is l/2. For distances from the wall closer than l/2 it is not possible for the fibers to perform this orbit without hitting the wall. As the distance to the wall decreases, the set of possible Jeffery orbits a fiber could perform is reduced. The only orbit that would be possible at the wall is the orbit given by C=0. The possible values of β for fibers performing Jeffery orbits in the near wall region are shown in figure 12. It is not possible for a fiber to perform a Jeffery orbit without hitting the wall if its combination of orientation and distance from the wall lies within the region below the solid line. It should be emphasized that this is only the case if the fibers are actually performing Jeffery orbits. As mentioned before, this assumption is reasonable for fibers close to the wall Pozrikidis (2005) and also at semi-dilute concentrations Koch & Shaqfeh (1990).

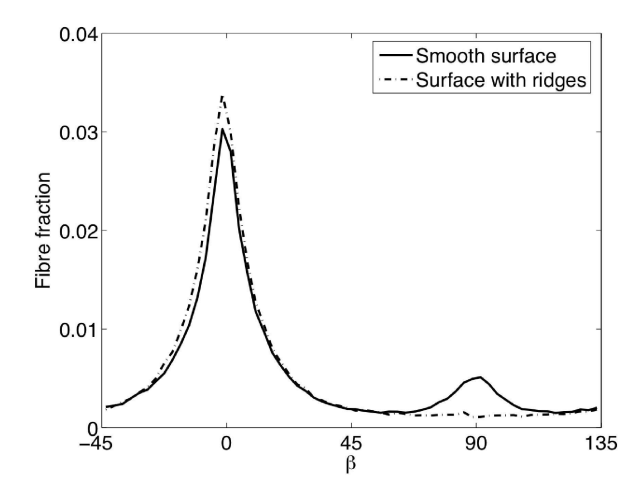


FIGURE 13. Angular distribution of fibers before particle-tracking analysis (camera position P4).

If a fiber would be located in the region below the line, the motion of the fiber could not possibly be described by equations (1–5).

4.2. Fiber orientation

4.2a. Angular distribution prior to particle-tracking analysis. In figure 13, the normalized distributions of orientations found in the images are shown. Data is shown for fibers flowing over the smooth (solid) and structured (dash-dot) surface. The distributions are determined based on 99760 fibers detected over the smooth surface and 100483 over the ridges. Since these values differ less than one percent, it is reasonable to conclude that the fiber orientation detection algorithm described above works as it should also in the case with the structured surface. The two distributions in figure 13 are fairly similar where the main part of the fibers appear at $\beta=0$, i.e. aligned with the flow. There is however one major difference, over the smooth surface, there is a considerable amount of fibers aligned across the flow direction, at $\beta=90^{\circ}$, which can be seen as a bump in the distribution function.

The data presented in figure 13 is based on images captured with the focus of the camera set at y=0, *i.e.* at the wall. The depth of focus, measured as the region were almost all fibers are detected by the algorithm, was approximately 1 mm. Thus, the distribution functions in figure 13 are integrated over this region.

4.2b. Wall-normal concentration distribution. In order to obtain a more detailed knowledge of how the wall influences the fiber orientation, the velocity

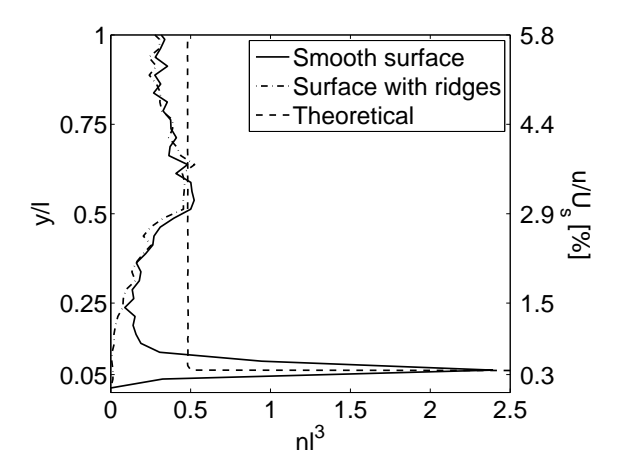


FIGURE 14. Variations in concentration as a function of the distance from the wall (camera position P4).

of individual fibers, given by the particle tracking algorithm, will be used. For the smooth surface, the known velocity profile gives a one-to-one relation between the velocity and distance to the wall of a fiber (assuming that the fibers follow the flow). Over the structured surface, this relation is less straightforward due to the complex and three-dimensional flow field that will appear close to the surface. This is reflected in the number of fibers which fulfils the conditions for having the velocity determined, as described previously. Over the smooth surface, the velocity of 12164 fibers is determined whereas only 10530 remain after the particle tracking algorithm for the case over the structured surface. When comparing these numbers with the 100 000 fibers found in total, it has to be remembered that three consecutive images are used to determine one velocity value and that some parts of the images are not used in order to ensure statistically independent samples. Nevertheless, a considerable amount of fibers seem to be lost over the structured surface. Therefore, the results below have to be interpreted with care for this case.

Based on the velocities and the known velocity profile (equation (7)), concentration profiles can be determined. Such profiles are shown in figure 14 for the two cases (solid and dash-dot as in previous graph) together with a profile calculated based on the (very low but still significant) sedimentation velocities of the fibers (dash). The data will be discussed below, but first the origin of the theoretical curve has to be explained.

The theoretical line is calculated based on three assumptions:

- That the fibers are evenly distributed at the inlet of the test section (x = 0);
- That the streamwise velocity of the fibers is given by the local flow velocity given by equation (7) and the wall-normal velocity by the sedimentation speed of a fiber oriented normal to gravity (this assumption is valid since the inclination of the plate is quite small and the fibers spend most of the time with this orientation to gravity); and
- That fibers stay very close to the wall once they have fallen down to this region.

This simplified analysis, which neither includes the wall effect on the sedimentation speed nor other aspects of the situation, is only used in order to get a qualitative understanding of the phenomena.

The sedimentation velocity is calculated based on the sedimentation velocity of the fibers, which is given as

$$v_s = \frac{(\rho_p - \rho_f)d^2}{16\nu\rho_f} \left(\ln(2r) + 0.193 + O(\ln(2r)^{-1})\right)g,\tag{14}$$

where r is the aspect ratio of the fibers and g is the acceleration due to gravity, see Herzhaft & Guazzelli (1999) and Batchelor (1970).

The experimental data from the flow over the smooth surface in Fig. 14 (solid) show a high concentration close to the wall (i.e. a lot of slow fibers), followed by a decrease and then an increase up to $nl^3 \approx 0.5$ at $y/l \approx 0.6$. Above $y/l \approx 0.6$, the number of fibers found in the images decreases.

For the flow over the structured surface, the concentration profile in Fig. 14 looks different and does not have the sharp peak close to the wall. This difference has to be interpreted in the light of the complex flow field over the structured surface. For a complete understanding, the flow over the ridges would have to be studied in detail, but it can be assumed that the ridges induce wall normal movements and (at least locally over the ditches) higher velocities close to the wall. These features of the liquid flow could explain the smaller amount of slow fibers.

As will be seen below, the sharp peak in the concentration profile close to the wall (or at small velocities) over the smooth surface in figure 14 is related to the bump in the orientation distribution at $\beta = 90^{\circ}$ in figure 13.

The fact that a large number of fibers are present very close to the wall is in conflict with the mechanism of "pole-vaulting" previously proposed by Stover & Cohen (1990). This discrepancy will be elaborated further on.

4.2c. Orientation at various distances from the wall. Finally, it is possible to look at the distribution at various distances (i.e. for fibers of different velocities) from the wall. These results are shown in figure 15 (smooth surface) and 16 (surface with ridges). In these figures, the orientation distributions for each distance from the wall are normalized in order to compensate for the varying

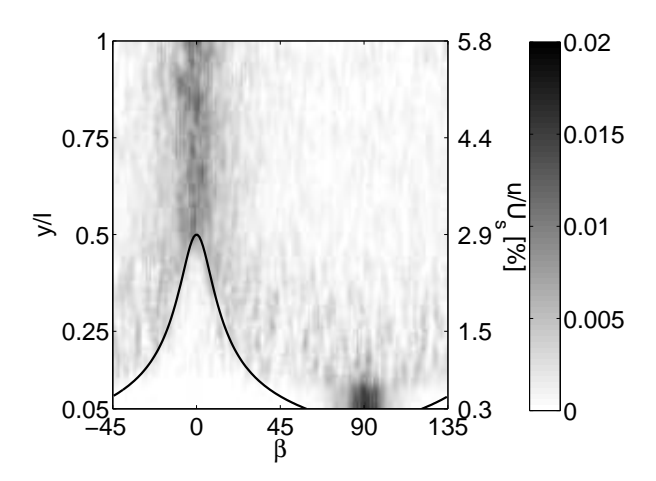


FIGURE 15. Fiber fraction as a function of β for different distances from the wall. Measurements performed on smooth surface (camera position P4).

concentration. The line defining the region in which Jeffery orbits can be performed (see figure 12) is shown as a solid line.

Starting with the smooth surface, it is seen that almost all of the fibers that have collected at the wall are oriented normal to the flow direction. Thus, the bump in the orientation distribution in figure 13 originates from fibers positioned close to the wall.

This is somewhat surprising, since there are a lot of orientations which are allowed according to the Jeffery orbit. A possible explanation for this could be that close to the surface, where the velocity is very low, the fibers have performed a large number of orbits. Since the period is 2–3 s, the distance 750 mm and the velocity < 3 mm/s, the number of orbits performed are in the order of 100. It is thus possible that instead of performing the pole vault previously observed by Stover & Cohen, the fibers are interacting with the wall through lubrication or direct contact and transfer to orbits with lower and lower C values (see figure 2) for each period. Finally, C would be close to 0 and the orientation is consequently close to $\beta = 90^{\circ}$. The fact that this, or any other mechanism that leads to $\beta = 90^{\circ}$ occurs, implies that the previously observed mechanism for wall interaction is not the only possible one.

Farther out from the wall, the fibers illustrated in figure 15 seem to be more evenly distributed over the orientations from y/l=0.2–0.5 and concentrated around $\beta=0$ further out.

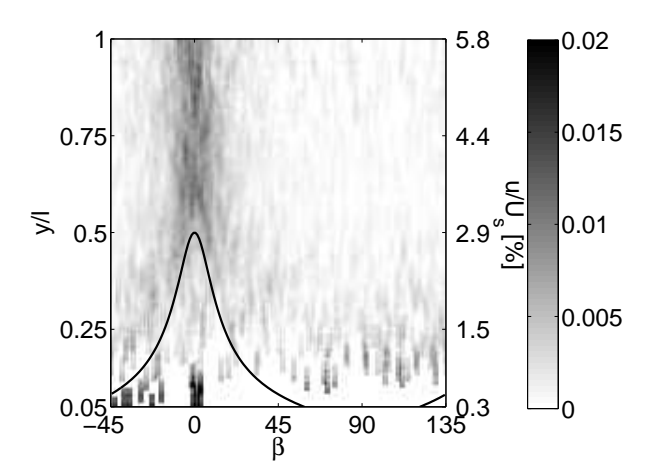


FIGURE 16. Fiber fraction as a function of β for different distances from the wall. Measurements performed on surface with ridges (camera position P4).

It is now time to take a closer look at the data from the flow over the structured surface. Before doing so, it is appropriate to remind the reader that the correlation between fiber velocity and distance from the wall is not valid in this case. It is therefore more appropriate to talk about fast and slow fibers. The orientation distribution for different fiber velocities is shown in figure 16 (the corresponding distance from the wall over the smooth surface is also shown). For fibers with a velocity down to that corresponding to y > 0.2l, the data is very similar to the smooth surface case. For y/l > 0.5, most of the fibers are oriented in the flow direction, in the region 0.2 < y/l < 0.5 the distribution is more homogeneous. The (very few, compare figure 14) slow fibers are oriented in the streamwise direction.

There are two possible reasons why there is only a small amount of fibers with low velocities detected over the structured surface. The first is that the detection algorithm (which relies on that the fibers move straight downstream) fails. The second is that there are fewer slow fibers. These two effects are probably combined. During the experiments it was observed that fibers were trapped in the ridges and followed the ridges for a while before continuing downstream. As mentioned above, the complex flowfield over the surfaces with ridges, with transversal, wall-normal and streamwise velocity fluctuations might also allow the fibers to travel faster, even though they are closer to the surface. Nevertheless, figure 13 clearly shows that there is no large portion of fibers with $\beta \approx 90^\circ$ over the structured surface even before the particle tracking algorithm. It has thus been shown that the smooth surface gives the

fibers collecting at the wall an orientation $\beta=90^\circ$ and that this effect is not present over the surface with ridges.

5. Conclusions

An experimental study has been performed on the subject of how fibers orient themselves in a shear flow close to a solid wall. A fiber suspension was allowed to flow down an inclined plate, thus forming a well-defined shear layer. As a visualization tool a CCD-camera was mounted underneath the flow in order to find the orientation of the fibers in the plane parallel to the wall. Experiments were performed with two different surface structures of the plate to explore the possibility of influencing the orientation of the fibers by modifying the structure of the wall. The first structure used was a plain smooth surface, while the other surface used was a surface with ridges oriented -30 degrees to the direction of the flow. For distances from the wall larger than one fiber length basically all fibers stayed aligned with the flow, for both surfaces. The fibers located in this region seemed to perform orbits similar to those described by Jeffery's mathematical analysis. For distances from the wall closer than one fiber length a difference could be seen between the experiments performed on different surfaces.

For the smooth surface the majority of the fibers no longer oriented themselves in the flow direction. Very close to the wall, less than about an eighth of a fiber length, nearly all of the fibers were oriented close to perpendicular to the flow direction.

Concerning the experiments performed on the surface with ridges, it is concluded that the particle-tracking algorithm used to follow the fibers, fails to do this in a satisfactorily manner. The reason for this is probably the disordered motion occurring close to the structured surface, where some of the fibers change direction as they flow down the plate. It is thus not perfectly clear what happens close to the surface with ridges. Nevertheless, it has been possible to show that the effect found close to the smooth surface, where many fibers orient themselves perpendicular to the flow, is not present for the structured surface with ridges.

The insights of the present study give two main directions for future work, the first is to study the selection between the "pole-vault" mechanism of fibers close to the wall identified earlier by Stover & Cohen and other mechanisms, leading to $\beta=90^\circ$. The second direction, which is critical for industrial applicability, is to study the orientation at higher velocities/lower viscosities in order to study the effects of inertia and turbulence.

Acknowledgments

Thanks go to Dr. Richard Holm for performing initial experiments and providing valuable input in the startup of the project. Dr. Söderberg has been

funded through the Biofibre Materials Centre (BiMaC) at KTH, Mr. Carlsson and Dr. Lundell has been funded by the European Commission under contract number 500345 (NMP2-CT-2004-500345). Dr. Lundell has also been funded by the Swedish Research Council (VR).

References

- ACHESON, D. J. 1990 Elementary Fluid Dynamics, 38-40. Oxford University Press.
- BATCHELOR, G. K. 1970 Slender-body theory for particles of arbitrary cross-section in Stokes flow. J. Fluid Mech. 44, 419–440.
- BINDER, R. C. 1939 The motion of cylindrical particles in viscous flow. *J. Appl. Phys.* **10**, 711–713.
- Bretherton, F. P. 1962 The motion of rigid particles in a shear flow at low Reynolds number. *J. Fluid Mech.* 14, 284–304.
- Cox, R. G. 1971 The motion of a long slender body in a viscous fluid. Part 2. Shear flow. J. Fluid Mech. 45, 625–657.
- Fellers, C. & Norman, B. 1998 Pappersteknik (in Swedish). KTH, Stockholm, Sweden.
- HERZHAFT, B. & GUAZZELLI, E. 1999 Experimental study of the sedimentation of dilute and semi-dilute suspensions of fibres. *J. Fluid Mech.* **384**, 133–158.
- Holm, R. 2005 Fluid mechanics of fibre suspensions related to papermaking. PhD thesis, Royal Institute of Technology, Stockholm, Sweden.
- ISO, Y., KOCH, D. L. & COHEN, C. 1995 Orientation in simple shear flow of semidilute fiber suspensions. 1. weakly elastic fluids. J. Non-Newtonian Fluid Mech. 62, 115–134.
- Jacob, M. & Unser, M. 2004 Design of steerable filters for feature detection using Canny-like criteria. *IEEE T. Pattern Anal.* **26** (8), 1007–1019.
- JEFFERY, G. B. 1922 The motion of ellipsoidal particles immersed in a viscous fluid. Proc. Roy. Soc. London A 102 (715), 161–179.
- KOCH, D. L. & SHAQFEH, E. S. G. 1990 The average rotation rate of a fibre in the linear flow of a semidilute suspension. *Phys. Fluids A* 2, 2093–2102.
- MORETTI, P. M. & KAYS, W. M. 1965 Heat transfer to a turbulent boundary layer with varying free-stream velocity and varying surface temperature an experimental study. *Int. J. Heat Mass Transfer* 8, 1187–1202.
- Moses, K. B., Advani, S. G. & Reinhardt, A. 2001 Investigation of fiber motion near solid boundaries in simple shear flow. *Rheol. Acta* 40, 296–306.
- Parsheh, M. 2001 Flow in contractions with application to headboxes. PhD thesis, Royal Institute of Technology, Stockholm, Sweden.
- Petrich, M. P., Koch, D. L. & Cohen, C. 2000 An experimental determination

- of the stress-microstructure relationship in semi-concentrated fiber suspensions. $J.\ Non-Newtonian\ Fluid\ Mech.\ 96,\ 101-133.$
- POZRIKIDIS, C. 2005 Orbiting motion of a freely suspended spheroid near a plane wall. J. Fluid Mech. **541**, 105–114.
- Schlichting, H. 1979 Boundary layer theory, 7th edn, 166–168. McGraw-Hill.
- Stover, C. A. & Cohen, C. 1990 The motion of rodlike particles in the pressuredriven flow between flat plates. *Rheol. Acta* 29, 192–203.
- Subramanian, G. & Koch, D. L. 2005 Inertial effects on fibre motion in simple shear flow. *J. Fluid Mech.* **535**, 383–414.
- Taylor, G. I. 1923 The motion of ellipsoidal particles in a viscous fluid. *Proc. Roy. Soc. London A* $\bf 103$, 58–61.
- White, F. M. 1991 $\it Viscous fluid flow, 2nd edn. McGraw-Hill.$

Paper 2

Orientation of slowly sedimenting fibers in a flowing suspension near a plane wall

By Allan Carlsson † , Fredrik Lundell † & L. Daniel Söderberg † , ‡

[†]Linné Flow Centre, KTH Mechanics, SE - 100 44 Stockholm, Sweden [‡]STFI-Packforsk AB, SE - 114 86 Stockholm, Sweden

The effect of a wall on the orientation of slowly sedimenting fibers suspended in a shear flow has been studied experimentally. Experiments were performed at two concentrations with two aspect ratios, $r_p \approx 7$ and $r_p \approx 30$, where r_p is defined as the fiber length divided by the diameter. For all cases the majority of the fibers were oriented close to parallel to the flow direction for distances farther away from the wall than half a fiber length. As the distance from the wall decreased a change in orientation was observed. At distances from the wall closer than about an eighth of a fiber length a significant amount of the fibers were oriented close to perpendicular to the flow. This was particularly clear for the shorter fibers. Due to the density difference between the fibers and the surrounding fluid the fiber concentration was increased in the near wall region. An increased concentration was found in a limited region close to half a fiber length from the wall. For the shorter fibers a large number of fibers was also detected in the very proximity of the wall.

1. Introduction

Suspensions of fibers are encountered in several engineering applications such as pharmaceutical applications, food processing, waste water treatment, composite processing and paper manufacturing. The final orientation distribution in the latter example is highly dependent on the suspension flow at an early stage of the process. As fibers travel with a suspension they will interact with the fluid, with each other and with the boundaries of the flow. This experimental study focuses on how fibers are oriented when they flow close to a solid wall.

A single fiber suspended in a linear shear flow will rotate due to the fluid motion. The flow situation is illustrated in figure 1. In this figure, the coordinates (x,y,z), the angles ϕ and θ defining the orientation of the fiber and the linear shear flow $\mathbf{u} = \dot{\gamma} y \mathbf{e}_x$ are defined. The angle β from the flow direction to the projection of the major axis of the fiber in the xz-plane is also shown.

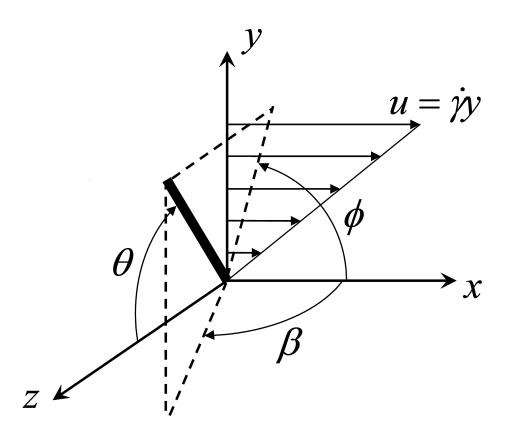


FIGURE 1. Coordinate system, velocity field and definitions of θ and ϕ used in Jeffery's analysis and β used for evaluation of the present data. The major axis of the fiber or spheroid is indicated with a thick line.

Jeffery (1922) derived the equations of motion for a spheroid suspended in a simple shear flow, assuming that inertia, both of the liquid and the spheroid, can be neglected. Under these assumptions, the rotation of the spheroid is described by

$$\dot{\phi} = -\frac{\dot{\gamma}}{r_e^2 + 1} \left(r_e^2 \sin^2 \phi + \cos^2 \phi \right) \tag{1}$$

$$\dot{\theta} = \left(\frac{r_e^2 - 1}{r_e^2 + 1}\right) \frac{\dot{\gamma}}{4} \sin 2\phi \sin 2\theta,\tag{2}$$

where r_e is the spheroidal aspect ratio of the particle, *i.e.* the ratio between the major and minor axes. The period of the rotation is given by

$$T_J = \frac{2\pi}{\dot{\gamma}} \left(\frac{r_e^2 + 1}{r_e} \right). \tag{3}$$

Integration of equations (1) and (2) with respect to time t yields

$$\cot \phi = -r_e \cot \left(\frac{2\pi t}{T_J} + \phi_0\right) \tag{4}$$

$$\tan \theta = \frac{Cr_e}{(r_e^2 \sin^2 \phi + \cos^2 \phi)^{1/2}},\tag{5}$$

where the orbit constant C and the phase shift ϕ_0 are constants determined by the initial conditions. It has been shown experimentally that Jeffery's analysis form a good approximation for the motion of fibers suspended in viscous shear flows, e.g. Taylor (1923); Binder (1939); Trevelyan & Mason (1951); Anczurowski & Mason (1968). Thus, equations (1–5) are valid also for cylindrical

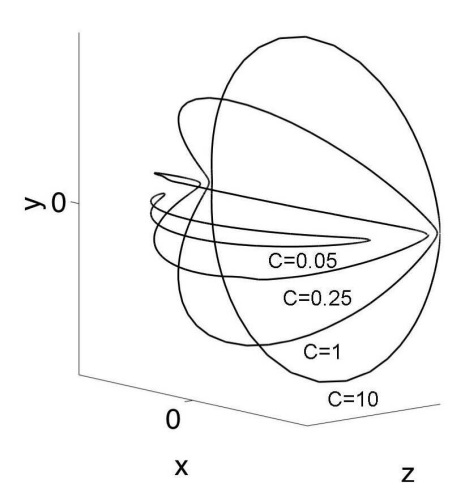


FIGURE 2. The path of a fiber end point for $r_e = 8$ and different C-values in Jeffery's equation.

fibers. This has also been shown analytically by Bretherton (1962). Furthermore, the equations are also valid in a paraboloidal flow if the shear rate is evaluated at the center of the particle, see Chwang (1975).

In order to use Jeffery's equations for cylindrical particles an equivalent spheroidal aspect ratio has to be used. The equivalent aspect ratio can be computed using the relation by Harris & Pittman (1975)

$$r_e = 1.14r_p^{0.844}. (6)$$

The geometrical aspect ratio is here denoted by $r_p = l/d$, where l and d are the full length and diameter of the fiber, respectively.

In figure 2 Jeffery orbits are shown for various values of C and $r_e=8$. The curves show the orbit of a fiber end point for the indicated values of C. At the limit of zero inertia, a fiber will rotate in closed orbits around its center of mass and will stay in the same orbit for an indefinite time, i.e. dC/dt=0. For C=0 the major axis of the fiber is aligned with the vorticity axis, i.e. $\beta=90$. The fiber spins around this axis, with the angular velocity $\dot{\gamma}/2$. For large values of C the fiber is oriented close to the flow direction most of the time, i.e. $\beta=0$. Every half period there is a rapid increase in $\dot{\phi}$, which results in a quick 180 degrees flip around the vorticity axis.

Jeffery's orbits are often used as a starting point for phenomenological explanations of the motion of fibers in a suspension. However, fiber-fiber and fiber-wall interactions are not taken into account. The wall effect has been studied both experimentally by e.g. Stover & Cohen (1990); Moses, Advani &

Reinhardt (2001); Holm & Söderberg (2007); Carlsson, Lundell & Söderberg (2007) and numerically by e.g. Dabros (1985); Hsu & Ganatos (1989, 1994); Gavze & Shapiro (1997, 1998); Pozrikidis (2005). A general conclusion is that Jeffery's equations still form a good approximation, although with an increasing period of rotation closer to the wall.

Fibers with values of β close to 0, located closer to the wall than half a fiber length, have been observed by Stover & Cohen (1990) to interact with the wall in what is referred to as a pole vaulting motion. When performing this motion, a fiber end point hits the wall due to its rotation. This results in a movement away from the wall, to a point where the fiber center is located approximately half a fiber length from the wall. The orientation of the fiber is kept close to $\beta=0$.

Holm & Söderberg (2007) and Carlsson et al. (2007) have studied the fiber orientation β close to a solid surface, where it has been observed that a considerable portion of the fibers tend to orient themselves perpendicular to the flow direction. For fibers rotating in Jeffery orbits the amplitude in the y-direction increases with increasing values of C, see figure 2. As a consequence the domain of possible Jeffery orbits, in the region y < l/2, is reduced. It was proposed by Carlsson et al. (2007) that the fibers move in Jeffery-like orbits also in the region near the wall and tend to adopt an orbit within the reduced domain. In the study it was also shown to be possible to influence the fiber motion near the wall by modifying the wall surface structure.

In the present study experimental measurements on flowing fiber suspensions with varying aspect ratios and concentrations will be presented. The fiber orientation β and concentration in planes parallel to a solid surface are analyzed. Compared to the earlier study by Holm & Söderberg the method for determining the wall normal position has been refined. Consequently, the orientation distribution near the wall is now better resolved. In addition, the concentration variation near the wall is now measured. The experimental apparatus and measurement techniques are described in section 2. This is followed by results and discussion in section 3. Finally the conclusions are given in section 4.

2. Experimental apparatus & technique

A CCD camera was used in order to visualize flowing fibers, in the proximity of a solid surface. Image analysis made it possible to find the velocity and orientation of the fibers in planes parallel to the solid surface. The velocity of the fibers and the wall normal velocity profile are used to determine their distance from the wall.

$r_p = l/d$		$\nu [\mathrm{m^2/s}]$	$\rho_f [\mathrm{kg/m^3}]$
7	295.5 ± 0.5	$(383 \pm 10) \cdot 10^{-6}$	1210 ± 15
30	295.5 ± 0.5	$(387 \pm 10) \cdot 10^{-6}$	1209 ± 15

TABLE 1. Temperature, kinematic viscosity and density of the liquid mixture in which the fibers were suspended.

2.1. Fiber suspension

The fiber suspension consisted of cellulose acetate fibers suspended in a viscous liquid. The density of the cellulose acetate fibers was $\rho_p \approx 1300 \text{ kg/m}^3$. Experiments were conducted using two different aspect ratios, $r_p \approx 7$ and $r_p \approx 30$, where the diameter of the fibers was $d \approx 70~\mu\text{m}$ and the length l of the fibers was cut to 0.5 and 2 mm, respectively. For each aspect ratio of the fibers two different concentrations were used. Expressed as the number of fibers to be found in a volume of l^3 these were $nl^3 \approx 0.01$ and 0.25 for $r_p \approx 7$ (cases A & B) and $nl^3 \approx 0.25$ and 2 for $r_p \approx 30$ (cases C & D).

The index of refraction of the fibers was approximately matched to that of the liquid. In order to visualize the fibers 100% of the fibers were dyed black for the low concentration cases (cases A & C). For the cases of higher concentration (cases B & D) only about 4% and 16% respectively of the fibers were dyed black.

The fibers do not deform in the present flow, but are to some extent permanently deformed. An analysis was made finding the tangents of the fiber end points on a set of fibers for both fiber lengths. From this analysis it is found that the curvature is smaller than 10 degrees for about 85% and 55% of the shorter and longer fibers, respectively.

The liquid phase was a mixture of polyethylene-glycol (PEG-400) and glycerine. The properties of the mixture for the two different aspect ratios are summarized in table 1. Note that the density of the liquid is lower than that of the fibers. The fibers will thus sediment slowly when suspended in the liquid.

2.2. Flow apparatus

In the experiments a film of the fiber suspension was flowing down an inclined glass plate. The thickness of the film was $h=17.0\pm0.2$ mm for the cases when $r_p\approx 7$ and $h=17.5\pm0.2$ mm when $r_p\approx 30$. A schematic figure of the test section is shown in figure 3. It is the same flow apparatus as the one used by Carlsson et al. (2007). The length of the channel was 1200 mm and the width was defined by an insert (the large gray area in figure 3), placed on the glass plate. From x=0 mm to x=150 mm there was a gradual change in the width, from 400 mm to 100 mm. For x>150 mm the width was constant and equal to 100 mm. The coordinates are defined in figure 3.

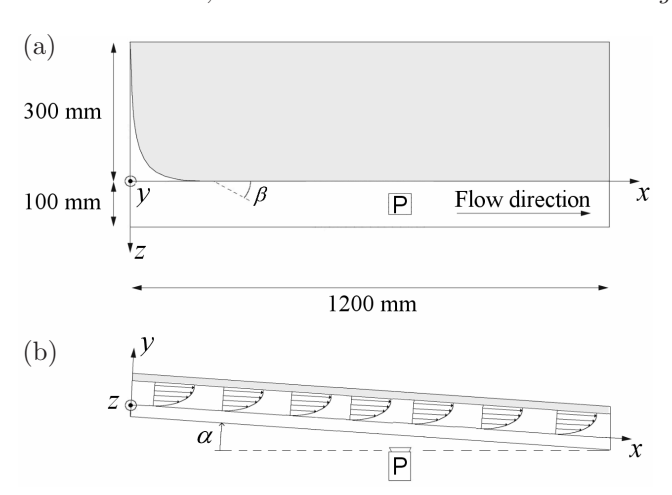


FIGURE 3. Schematic figure of the flow section, (a) Top view, (b) Side view. The camera position for orientation measurements is denoted by P.

The velocity in the x-direction of a Newtonian fluid film flowing down an inclined plane is given by

$$u = \frac{g}{2\nu}y(2h - y)\sin\alpha,\tag{7}$$

where g is the constant acceleration of gravity, ν is the kinematic viscosity of the fluid and y is the wall normal position, where y=0 at the wall and y=h at the free surface of the film. Furthermore α is the angle of inclination of the plane with respect to horizontal. In the present experiments $\alpha=2.60\pm0.1$ degrees. Equation (7) can for instance be found in Acheson (1990).

It was shown previously by Carlsson et al. (2007) that the flow is fully developed and that there is no acceleration present in the flow. Typical velocity profiles are shown in figure 4. The velocity u and wall normal position y is normalized with the free surface velocity U_s and liquid sheet thickness h, respectively. The measurements were conducted on fibers with $r_p \approx 30$ at $nl^3 \approx 0.15$ and each dot represents the velocity and position of one fiber tracked through three consecutive images. The solid line is given by equation (7). The dashed lines denotes the minimum and maximum velocity based on the accuracies in measuring h, α and ν .

It is noted that there is some scatter in the data. A small fraction of the detected fibers have unphysical velocities which are due to mismatches in the particle tracking velocimetry algorithm, which will be explained briefly in the following section. For x=650 mm in figure 4 (a) the fraction of erroneous velocities is as high as 14%, whereas for x=750 and 850 mm in (b) and (c)

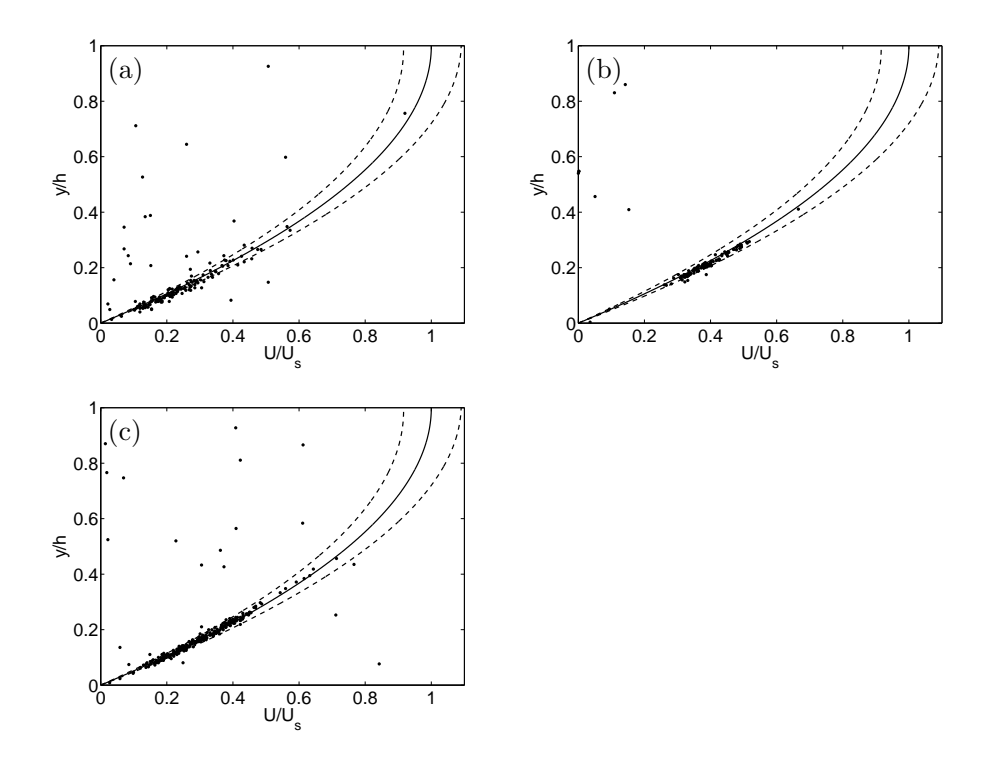


FIGURE 4. Velocity profile in the flow apparatus at x = 650, 750 and 850 mm in (a), (b) and (c), respectively.

the fraction is about 6%. Similar errors will be present also in the orientation measurements although less frequently. The reason for this is that the image quality is poorer in the velocity profile measurements, since the plane of focus of the camera is located about 5 cm into the suspension in comparison to only a couple of millimeters for the orientation measurements.

Disregarding the scattering, the measured velocities coincide well with the profile given by equation (7). This fact will be used to determine the distance to the wall of individual fibers in the orientation measurements.

$2.3.\ Measurement\ \&\ analysis\ procedure$

2.3a. Image capturing. For the orientation studies the CCD camera was mounted underneath the glass plate at x=750 mm (position P in figure 3). Images were captured, three at a time, with a frequency of $f=5.13\pm0.05$ Hz when $r_p\approx7$ and $f=10.27\pm0.05$ Hz when $r_p\approx30$. There was a delay of $T_s\approx12$ s between every set of three images. The delay was implemented in order for the fibers to pass out of the field of view before the next set of three images was

captured. Therefore the exact length of T_s is not crucial. A total of 300 images per set of three images were captured for each fiber length and concentration. The field of view of the images was $X \times Z = 15 \times 20 \text{ mm}^2$ for $r_p \approx 7$ and $X \times Z = 12 \times 17 \text{ mm}^2$ for $r_p \approx 30$, where X and Z are the sizes of the image in the x- and z-directions, respectively.

2.3b. Determination of fiber orientation. The angle β is defined as the angle in the xz-plane taken clockwise from the flow direction (when viewed from above), figure 3. To determine the orientation β of the fibers a second order ridge detector within the class of steerable filters derived by Jacob & Unser (2004) was used. The filter has been evaluated for fiber detection in flowing suspensions by Carlsson, Lundell & Söderberg (2009).

2.3c. Determination of fiber velocity. In order to find the velocity of the fibers a particle tracking velocimetry (PTV) algorithm was used. The PTV-algorithm uses information concerning the location of individual fibers in three subsequent images. In order to indentify a particular fiber in the second image a rectangular area is generated with a chosen width and a length starting from the original fiber position to the end of the image in the streamwise direction. All fibers inside the rectangular area in the second image are considered as candidates of being the same as the original fiber. The distance from the original position to a candidate position is used to compute a position where the fiber should be in the third image if it is assumed to travel with the same velocity. If a fiber is detected sufficiently close to the computed position, for the candidate fiber, in the third and last image it is considered to be the same fiber as the original fiber.

Threshold values have to be set on the sizes of the areas in which fibers are searched for in the second and third image of the set. The width of the areas in the z-direction are 0.4l and 0.2l for the short and long fibers, respectively. The length in the streamwise direction x in the third image is of the same order of magnitude, but also varies with the velocity so that the length is increasing with the velocity. This is done in an attempt to reduce an under-representation of faster fibers.

Fibers found in a set of three images, with a velocity higher than X/T_s , will leave the field of view before the subsequent set of images are captured, independently on their location in the images. The velocity X/T_s corresponds to a distance from the wall of $y \approx d$. To ensure statistically independent data the x-position where the fibers has to be found in the images is set to be a function of the fiber velocity u_{fib} . If X_0 is the x-position farthest upstream in the images, the fiber has to be found in the region between X_0 and $X_0 + u_{fib}T_s$. In this manner the possibility of finding a fiber with a velocity lower than X/T_s , more than once, is eliminated. For further details, see Carlsson et al. (2007).

Case	$r_p = l/d$	nl^3	N
A	7	0.01	5933
В	7	0.25	5427
$^{\mathrm{C}}$	30	0.25	4825
D	30	2.0	6277

Table 2. Aspect ratio, concentration and number of detected fibers N for cases A-D.

2.3d. Determination of fiber concentration. The concentration of fibers at y is determined by the number of fibers N that is detected inside of the volume $V = \Delta X \Delta Y \Delta Z$. The concentration at $y = y_k$ can then be expressed as

$$c(y_k) = \frac{N(x \in [0, \Delta X], y \in [y_k - \Delta Y/2, y_k + \Delta Y/2], z \in [-\Delta Z/2, \Delta Z/2])}{V}.$$
(8)

Here $\Delta Z=Z$ and ΔY can be chosen arbitrarily, with the help of equation (7), based on the desired resolution in the y-direction. The distance $\Delta X=X-2u_{fib}/f$ is however a function of the fiber velocity, see Carlsson et al. (2007). This is due to the fact that the fibers have to be found in three subsequent images and that the fibers will travel a distance within the period it takes to capture these images. Hence, it is not possible to detect fibers of $u_{fib}>Xf/2$ since these fibers will have left the field of view, before the third of the three images is captured, independent on their location in the first image. In practise, this limits the maximum value of y where a fiber can be detected. It is also worth mentioning that the absolute value of the computed concentration is uncertain, mainly since it is strongly coupled to the threshold values set in the PTV.

3. Results & Discussion

Measurements from four cases (A, B, C & D) will be presented. The aspect ratios and concentrations of the cases are shown in table 2 together with the total number of fibers N for which the velocity and orientation have been determined in the region 0 < y/l < 1.5. In the presented results the computed angular distribution at different distances from the wall is reported. The wall normal distribution of fibers is also shown.

3.1. Period of rotation in near wall region

The period of rotation close to the wall is measured manually for a small set of 23 individual fibers. This is done in order to validate that the fibers are rotating with a period in reasonable agreement with Jeffery's equations. A separate set of images were captured with the frequency $f=5.13\pm0.05$ Hz for $r_p\approx7$ and

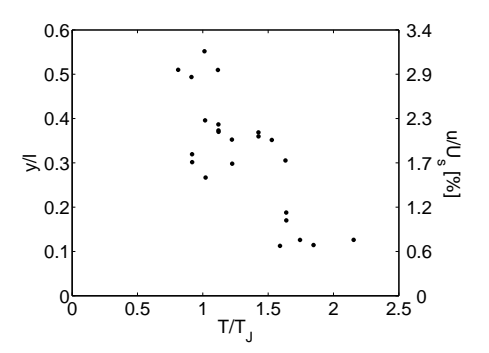


FIGURE 5. Period of rotation of individual fibers with $r_p \approx 7$ as a function of y.

 $nl \approx 0.01$. The images are captured in the xz-plane. In order to measure the period of rotation it is necessary to detect a change in orientation of the fibers in the sequence of images. Therefore the period was only measured on fibers that have a minimum value of β between 30 and 60 degrees during its complete rotation. There are few longer fibers fulfilling this restriction why the period was only measured on short fibers. The velocity of the fibers was measured simultaneously in order to estimate the fiber's distance from the wall.

The results of the rotation period are shown in figure 5. Each dot in the figure denotes the measured period of rotation, normalized with the Jeffery period, of an individual fiber. The maximum error of T/T_J for a fiber is estimated to be about ± 0.4 . The reason for the large error is partly due to the low frame rate of camera which can cause an error in the measured rotation. There is also a width distribution of the fibers that affects the Jeffery period used for normalization. Nevertheless, a trend can be seen. For distances from the wall about $y/l \approx 0.5$ the period is around the period given by Jeffery, which is reasonable. Closer to the wall the period increases to values large enough so that a fiber could not possibly rotate with the Jeffery period even with the relatively large error of T/T_J taken into account. An increased period of rotation near the wall is also consistent with earlier studies, e.g. Dabros (1985); Stover & Cohen (1990); Gavze & Shapiro (1997) and Pozrikidis (2005).

3.2. Concentration variations in the wall-normal direction

As mentioned previously the concentrations investigated were $nl^3 \approx 0.01$ and 0.25 for $r_p \approx 7$ (cases A & B) and $nl^3 \approx 0.25$ and 2 for $r_p \approx 30$ (cases C & D). These are the initial concentrations that one would expect to find if the fibers were homogenously distributed across the shear layer. In figure 6 the concentration c(y), defined in equation (8), is shown. The concentrations

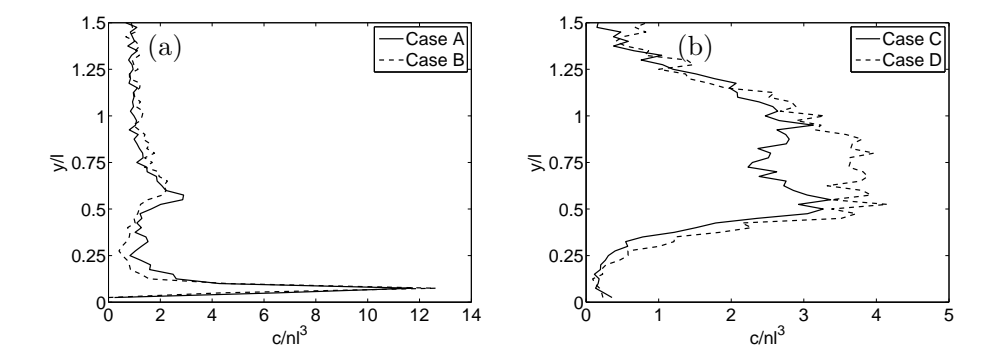


FIGURE 6. Variations in concentration as a function of the distance from the solid surface for fibers with $r_p \approx 7$ in (a) and $r_p \approx 30$ in (b).

have been normalized with their respective initial concentration, which is only approximative. Also, the obtained concentration level is partly coupled to threshold values set in the PTV-algorithm. Therefore the absolute values in figure 6 should be interpreted with some care. Nevertheless, the distribution of the fibers is similar for different threshold values. This is shown in figure 7 where the threshold values has been modified for cases B & C. The solid lines correspond to the original threshold values in the PTV-algorithm, upon which the results presented are based. The other two lines, the dot-dashed and the dashed, correspond to lower and higher threshold values, respectively. The new threshold values are set so that the areas, in which fibers are searched for in the PTV-algorithm, is roughly half or twice the areas of the original threshold values. The result is roughly 10-20% more or less detected fibers as compared to the original threshold values. The relative distribution of fibers is not highly dependent of the threshold values. Thus, conclusions can be drawn concerning the different characteristics of the concentration profiles seen for $r_p \approx 7$ and $r_p \approx 30.$

Returning to figure 6 it is seen that for all cases there is an increase in concentration near y/l=0.5. It is likely that fibers sufficiently close to the wall will undergo a pole vaulting motion similar to the motion previously observed by Stover & Cohen. This should result in an increased concentration at about half a fiber length from the wall. From figure 6 it is clear that there is an increase in concentration for all cases near y/l=0.5.

The accuracy of the velocity measurements is based on measurements of ν , α and h. Taking this into account there could be a small offset, constant for each respective case, in the determination of y. The distance from the peak of

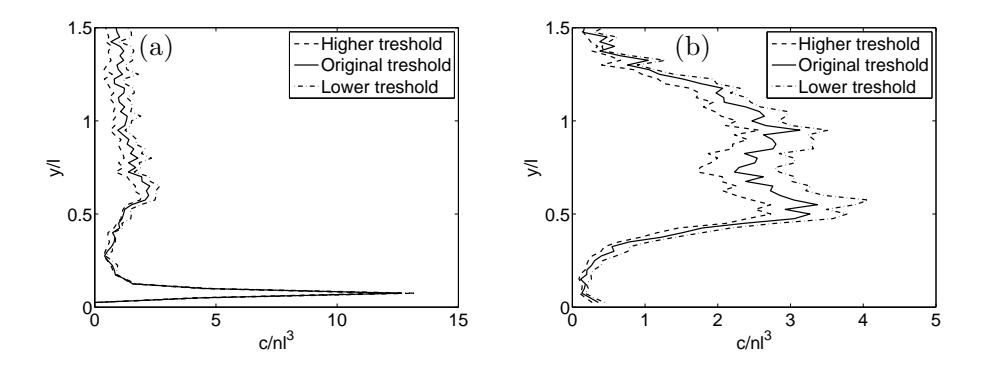


FIGURE 7. Variations in concentration as a function of y for different threshold values set in the PTV; (a) case B and (b) case C.

the increased concentration near half a fiber length from the wall to y/l=0.5 is smaller than the estimated possible offset for all cases apart from case B.

For $r_p \approx 7$ in figure 6 (a) there are also a large number of fibers accumulated very close to the wall. The origin of this accumulation is clearly the density difference between the fibers and fluid. Still, the accumulation at the wall is only seen for the shorter fibers. There is a small trace of a local increase near the wall also for the longer fibers in (b) at the wall, but this increase is very small if compared with the peak for the shorter fibers.

3.3. Angular distribution in near wall region

The orientation distribution for all cases, at x=750 mm, is shown in figure 8 for different distances from the wall, *i.e.* for different fiber velocities. The distance from the wall has been scaled with the fiber length l. In order to compensate for a varying wall normal concentration the orientation distribution is normalized at each distance from the wall. The darker regions in the graphs indicate where the fraction of fibers is large. Below the solid line it is not possible for a fiber to complete any undisturbed Jeffery orbit without hitting the wall.

Due to the positive streamwise rate-of-strain in the upstream contraction, between x=0 and x=150 mm, the fibers will initially tend to align with the flow direction ($\beta=0$). It is clear for all cases that for distances farther away from the wall than half a fiber length most of the fibers have stayed close to the flow direction. As the distance is decreased below y/l=0.5 the shorter fibers in (a) and (b) are detected above the solid line, where it is possible to rotate in Jeffery orbits. In the very proximity of the wall the fibers are oriented close to perpendicular to the flow direction. Also for the longer fibers a change in orientation is observed near the wall. When interpreting (c) and (d) near the

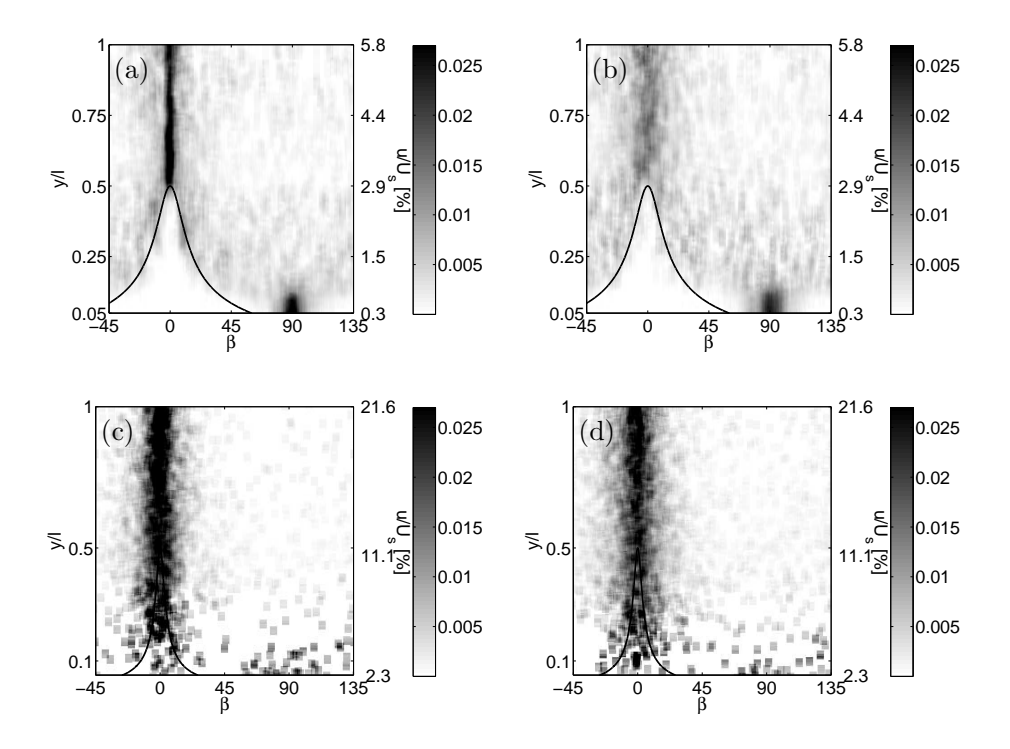


FIGURE 8. Fraction of fibers as a function of β for different distances from the wall; (a) $r_p \approx 7$, $nl^3 \approx 0.01$, (b) $r_p \approx 7$, $nl^3 \approx 0.25$, (c) $r_p \approx 30$, $nl^3 \approx 0.25$ and (d) $r_p \approx 30$, $nl^3 \approx 2.0$. The distribution of fibers is normalized at each y-position.

wall it should be kept in mind that the statistics is weak here due to the low concentration. Still, some of the longer fibers are detected in the region below the solid line.

In order to investigate the significance of the fibers detected below the line in figure 8 (c) and (d) a manual inspection was made of the images. Twenty of the fibers located below the line in 8 (c) were investigated. Fifteen of these fibers were found to have a curvature of the order 10 to 20 degrees. Two of the fibers were mismatches in the PTV where the velocity is based on different fibers in the set of three subsequent images. Two other fibers were located so close to the line so that they might as well be interpreted to be on the line or slightly above. The remaining fiber was a fiber with $r_p \approx 7$ which had remained in the system after the previous measurements. The curved fibers tended to be detected in the region above y/l = 0.2 where the angular spacing to the solid

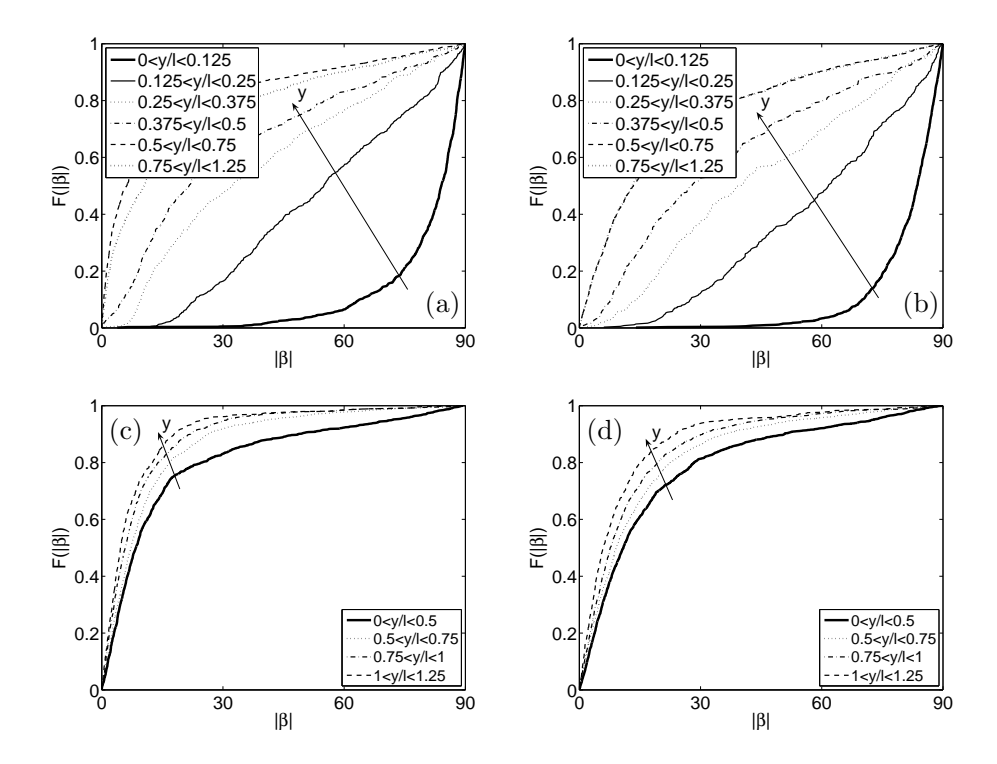


FIGURE 9. Distribution function $F(|\beta|)$ at different distances from the wall; (a) case A, (b) case B, (c) case C and (d) case D.

line is relatively small. Concluding, no straight fiber was detected in an area where it could not rotate in a Jeffery orbit without hitting the wall.

Detailed information on the orientation of the fibers is given by the distribution function $F(|\beta|) = P(B \le |\beta|)$, defined as the probability that a fiber will be oriented between the flow direction and a given angle $|\beta|$. The distribution function is shown in figure 9 for all cases. The figures illustrate how $F(|\beta|)$ varies with the distance from the solid surface. In figure 9 (a) and (b), $r_p \approx 7$, it is seen that for distances farther away from the wall than half a fiber length the majority of the fibers are still oriented close to the flow direction, since F increases rapidly at $|\beta| = 0$. However, as soon as the fibers are located closer to the wall than half a fiber length $F(|\beta|)$ changes character. A gradual change towards a more isotropic distribution occurs as the distance from the wall is decreased to $y/l \approx 0.25$. When the distance is decreased even more the fibers tend to orient themselves close to perpendicular to the flow direction in the region 0 < y/l < 0.125.

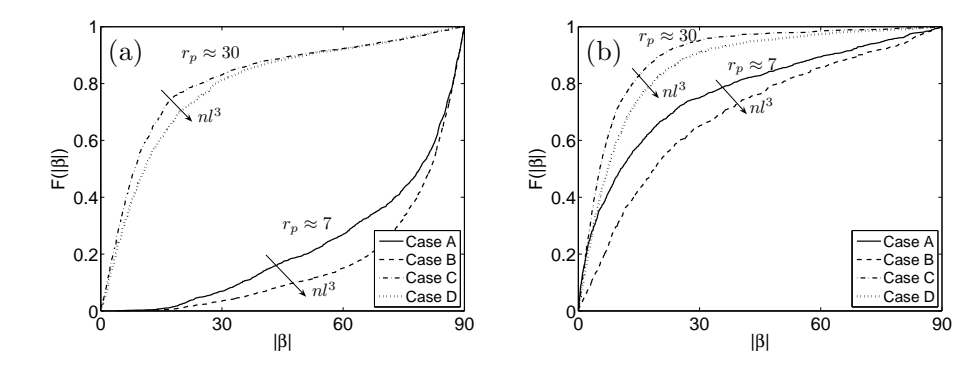


FIGURE 10. Distribution function $F(|\beta|)$ for all cases: (a) in the region 0 < y/l < 0.5 and (b) in the region 0.75 < y/l < 1.25.

The angular distribution at different y-positions, for fibers with aspect ratio $r_p \approx 30$, are presented in figure 9 (c) and (d). Due to the limited statistics near the wall the resolution is reduced as compared to the shorter fibers. The distributions show that the fibers are fairly aligned with the flow direction for all cases, although the fibers tend to be less aligned when the distance to the wall is decreased.

The differences and similarities between the cases are highlighted in figure 10. $F(|\beta|)$ is shown for all cases in two different regions; close to the wall, 0 < y/l < 0.5, in (a) and about one fiber length from the wall, 0.75 < y/l < 1.25, in (b). The longer fibers are clearly more aligned than the short fibers in both regions. A small effect is also noted for a change in concentration; for both aspect ratios the fibers tend to adopt slightly higher values of β for an increasing concentration. This could perhaps be attributed to fiber-fiber interactions.

3.4. Physical mechanisms for drift in fiber orientation

It is seen in figure 8 (a) and (b) that the shorter fibers tend to adopt an orientation that makes it possible to rotate in Jeffery orbits also near the wall. It is also clear from figure 6 that the shorter fibers tend to accumulate at the wall. In order for a fiber, initially at some distance from the wall, to end up at the wall there has to be a migration in orientation as the wall is approached. In other words, there has to be a physical mechanism that affects the fiber orientation so that a fiber, initially oriented close to the flow direction, can end up oriented close to perpendicular to the flow when it reaches the wall.

In this section the order of magnitude of inertial and sedimentation effects will be considered leading to the results in figure 12. The experimental results

indicate that the fibers are rotating in a manner close to the solution of Jeffery (1922). It is therefore assumed that this will be the base motion and that inertia and sedimentation will only cause a small deviation from the solution. The drift in orientation in the present experiments will be estimated based on theoretical predictions on inertial and sedimentation effects by Subramanian & Koch (2005) and Carlsson & Koch (2009).

3.4a. Drift due to sedimentation towards the wall. Due to the density difference between the fibers and the fluid, the fibers will sediment slowly. As a sedimenting fiber approaches a wall the velocity disturbance of the fluid, due to the presence of the fiber, will be reflected by the wall. This causes the fiber to rotate towards the xz-plane, i.e. towards an orientation parallel to the wall. Carlsson & Koch (2009) estimated this rotation for a large aspect ratio fiber in a wall-bounded shear flow. This was done by introducing a mirrored image fiber in order to ensure that the vertical velocity component at the wall is equal to zero. The rotation of a fiber nearly aligned with a wall as it sediments towards the wall in an otherwise quiescent fluid was found to be

$$\dot{\phi}_{wr} = \frac{3\phi\Delta\rho gV}{2\pi\mu l^2} \left[\frac{16y_*^2}{3} - \left(1 + 4y_*^2\right)^{1/2} \left(\frac{8y_*}{3} + \frac{1}{6y_*}\right) + y_* \ln\left[\frac{(1 + 4y_*^2)^{1/2} + 1}{(1 + 4y_*^2)^{1/2} - 1}\right] \right],\tag{9}$$

where y_* is the distance from the wall of the fiber center normalized with l. Furthermore, μ , V and $\Delta \rho$ is the dynamic viscosity of the fluid, the volume of the fiber and the density difference between the fiber and fluid, respectively. The angles ϕ and θ are defined in figure 1.

Due to the linearity of the problem the principle of superposition applies to the rotation of the fiber. Therefore, as long as there is no wall contact, equation (9) estimates the additional rotation rate of a fiber in a shear flow, when it is oriented close to the xz-plane. A fiber rotating in a Jeffery orbit spends most of its time nearly aligned with the xz-plane. Therefore it is reasonable to expect that most of the orbit drift takes place when the fiber is oriented close to this plane. A more detailed justification of this assumption is given by Carlsson & Koch. A consequence of the fiber being nearly parallel to the wall is also that the rate of change of θ due to the wall reflection $\dot{\theta}_{wr} \ll \dot{\phi}_{wr}$ and it is therefore not considered.

Carlsson & Koch also introduced a local contact force at one of the fiber end points to model the situation when contact occurs between the wall and the fiber. Both a no slip and a free slip condition for the wall contact were considered. The additional rotation rate from the model was found to be

$$\dot{\phi}_c^{ns} = K^{ns} \left[\frac{3\ln(2r_p)\cos\phi}{8\pi\mu l^2\sin\theta} \Delta\rho gV \right]$$
 (10)

$$\dot{\phi}_c^{ns} = K^{ns} \left[\frac{3 \ln(2r_p) \cos \phi}{8\pi \mu l^2 \sin \theta} \Delta \rho g V \right]$$

$$\dot{\theta}_c^{ns} = K^{ns} \left[\frac{3 \ln(2r_p) \cos \theta \sin \phi}{8\pi \mu l^2} \Delta \rho g V \right],$$
(10)

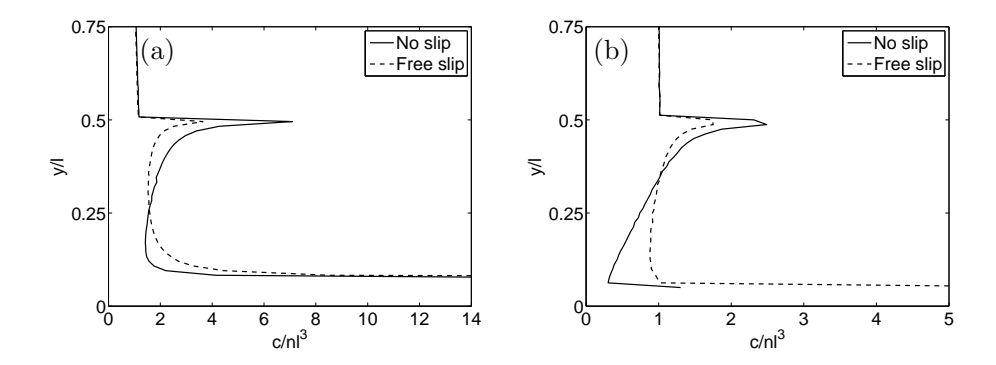


FIGURE 11. Computational concentration profiles with no slip and free slip wall contact condition for (a) $r_p \approx 7$ and (b) $r_p \approx 30$.

for a no slip condition applied for the fiber end point in contact with the wall and

$$\dot{\phi}_{c}^{fs} = K^{fs} \left[\frac{3\dot{\gamma}\sin^{2}\theta\sin^{2}\phi(\sin^{2}\phi - 1)}{2(\sin^{2}\theta\sin^{2}\phi - 2)} + \frac{3\ln(2r_{p})}{4\pi\mu l^{2}} \Delta\rho gV \frac{(1 + \sin^{2}\theta\sin^{2}\phi)(1 - \sin^{2}\phi)}{\sin\theta\cos\phi(2 - \sin^{2}\theta\sin^{2}\phi)} \right]$$
(12)

$$\dot{\theta}_c^{fs} = K^{ns} \left[\frac{3\dot{\gamma}\sin^3\theta\cos\theta\sin^3\phi\cos\phi}{2(2-\sin^2\theta\sin^2\phi)} + \frac{3\ln(2r_p)}{4\pi\mu l^2} \Delta\rho g V \frac{\cos\theta\sin\phi(1+\sin^2\theta\sin^2\phi)}{(2-\sin^2\theta\sin^2\phi)} \right]$$
(13)

for a free slip condition. The parameters K^{ns} and K^{fs} are non-zero and equal to one only when the fiber end point is in contact to the wall.

It was shown that both the rotation due to the wall reflection and due to the wall contact causes a migration towards lower values of the Jeffery orbit constant C, *i.e.* towards higher values of β . In a comparison of the model with the present experimental data, for fibers with $r_p \approx 7$, a qualitative agreement was found in that there was an accumulation of fibers oriented perpendicular to the flow direction at the wall.

In order to estimate the concentration profile a large number of fibers is chosen at the inlet of the channel. The concentration is initially assumed to be $c/nl^3 = 1$ for all y-positions. The initial orientation distribution is found by

using the relation

$$f(C) = \frac{RC}{\pi \left(4RC^2 + 1\right)^{3/2}},\tag{14}$$

derived by Rahnama, Koch & Shaqfeh (1995) to be a steady state orientation distribution for dilute and semi-dilute aspect ratios in the limit of large aspect ratio. In equation (14) R is a fitting parameter. Here R is chosen so that the single moment $\langle \cos^2 \beta \rangle$ of the β -distribution is the same as for the experiments. Only fibers detected at y/l > 1 and y/l > 0.5 for $r_p \approx 7$ and 30, respectively, is used to find R. This results in $R \approx 0.57$ and 0.97 for the fibers with $r_p \approx 7$ and 30, respectively.

In figure 11 the computational concentration profiles are shown. For the shorter fibers in (a) the profiles for the no slip and free slip condition are qualitatively similar to the experimental profiles for cases A and B shown in figure 6 (a). There is an increased concentration at the wall and also at $y/l \approx 0.5$ due to a pole-vaulting-like motion occurring as a result of the wall contact conditions. For the longer fibers in 11 (b) there is a peak at $y/l \approx 0.5$ and there is also an increase in concentration near the wall. The local increase in concentration near the wall for case C and D in figure 6 (b) seems a bit small to be explained when only taking into account the sedimentation according to Carlsson & Koch.

3.4b. Drift due to fluid inertia. Since fewer fibers are detected at the wall than expected for fibers with $r_p \approx 30$, when taking sediment effects into account, this suggests that there may be at least one additional physical mechanism acting in the experiments. It has been shown in earlier studies (Qi & Luo 2003; Subramanian & Koch 2005, 2006; Altenbach et al. 2007) that both fluid and particle inertia are expected to drift a fiber, suspended in a simple shear flow, towards a final orientation in the xy-plane, i.e. towards $\beta=0$. In this plane the fiber will spend most of its time close to the flow direction. Since inertia will tend to rotate the fibers towards the xy-plane this could potentially prevent the drift in orientation towards the vorticity axis, due to sedimentation towards the wall. Near the wall in the experiments, a particle Reynolds number $Re_d = \dot{\gamma} l^2/\nu$ based on the full length l of the fiber, is about 0.01 and 0.2 for fibers with $r_p \approx 7$ and 30, respectively. Although Re_l appear small also for $r_p \approx 30$ it could be large enough to slow down or possibly even prevent a weak drift towards the vorticity axis.

The magnitude of inertial effects can be estimated based on the work of Subramanian & Koch (2005). They examined the motion of a fiber suspended in a simple shear flow, for a small but finite Re_l . The fiber is assumed to be slender and the particle Reynolds number based on the diameter of the fiber $Re_d = \dot{\gamma} ld/\nu$ is considered negligible. As mentioned one result of their study is that a small Re_l will tend to drift the rotating fiber towards the xy-plane and

 $\beta = 0$. From Subramanian & Koch the additional rotation rate of a fiber due to fluid inertia in a simple shear flow is given by

$$\dot{\phi}_{in} = -\frac{\dot{\gamma}Re_l}{16\ln(r_p)}\sin^2\theta\sin^2\theta\cos^2\phi\left(\frac{1}{3} - \frac{7}{15}\cos^2\phi\right) \tag{15}$$

$$\dot{\theta}_{in} = \frac{7\dot{\gamma}Re_l}{120\ln(r_p)}\sin^3\theta\cos\theta\sin^2\phi\cos^2\phi. \tag{16}$$

3.4c. Estimation of drift in orientation. Equations (9–15) estimates the drift in orientation due to sedimentation towards the wall and fluid inertia. An approximation of the total rate of rotation is now:

$$\dot{\phi} = \dot{\phi}_{jef} + \dot{\phi}_{wr} + \dot{\phi}_c + \dot{\phi}_{in} \tag{17}$$

$$\dot{\theta} = \dot{\theta}_{jef} + \dot{\theta}_c + \dot{\theta}_{in},\tag{18}$$

where $\dot{\phi}_{jef}$ and $\dot{\theta}_{jef}$ is Jeffery's equations defined in equations (1) and (2). Since the terms from sedimentation and inertia are small, a fiber is not expected to deviate far from a Jeffery orbit in one period. Therefore it is convenient to study how the orbit constant C, introduced in equation (5), changes with time. This is shown in figure 12 for different initial orbit constants C_0 and initial distances y_0 from the wall. The results for fibers with $r_p \approx 7$ is shown in (a) and (b) for the no slip and free slip wall contact condition, respectively. In (c) and (d) the results for $r_p \approx 30$ is shown for both wall contact conditions. On the horizontal axis β_{0min} is the minimum absolute value of β over a complete period that a fiber with the initial orbit constant C_0 obtains.

The solid lines in the figure show where dC/dt=0, or more accurately where the change of C over half a period of rotation is zero. Below the solid line dC/dt<0, since the estimated effect due to wall reflection and wall contact is larger than the effect of fluid inertia, resulting in a total drift towards larger values of β . Above the solid line dC/dt>0 resulting in gradually smaller values of β . The dashed lines shows the minimum value of β for a fiber rotating in Jeffery orbits without hitting the wall. If a fiber is located below the dashed line the fiber will make contact with the wall during the flip and the wall contact is included in the computations. It is emphasized that the figure indicates the sign of dC/dt over half a period of rotation at various initial conditions. As time evolves a fiber will change both its orientation and wall normal position. Above the dashed line a fiber will always sediment towards lower values of y. However, it will never be allowed to sediment far below the dashed line since it will continuously be pushed up to the dashed line in each flip around the vorticity axis due to the wall contact.

It is seen in figure 12 (a) and (b) that the results with no slip and free slip are identical for the short fibers. Recall that only the sign of dC/dt is shown in the figure. The values of dC/dt will differ in the region on and below the dashed line where the wall contact is included in the computations. The fact

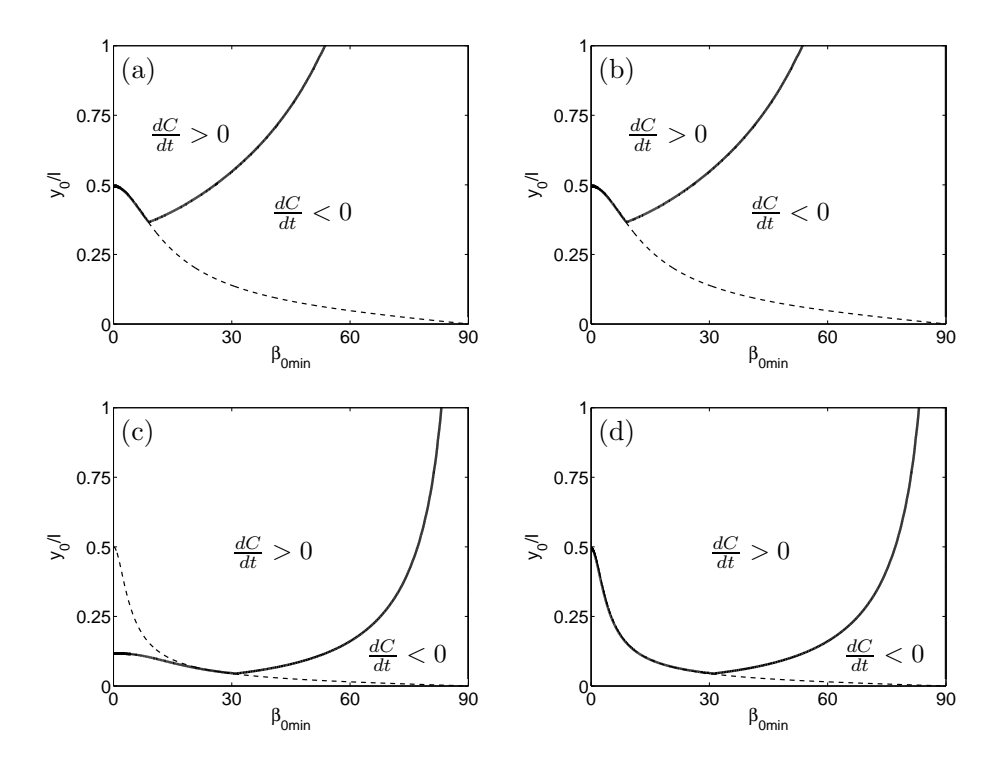


FIGURE 12. The sign of the orbit drift for different inital orientations and distances from the wall. The solid line indicates where dC/dt=0 and below the dashed line a fiber will make wall contact during its flip around the vorticity axis. Fibers with $r_p\approx 7$ with (a) no slip condition and (b) free slip condition during wall contact. Fibers with $r_p\approx 30$ with (c) no slip condition and (d) free slip condition.

that (a) and (b) are the same just shows that the wall contact, for both the no slip and free slip condition, causes an orbit drift strong enough to make the total change of C over half a period of rotation to be negative. This is the case for all orientations of a fiber, *i.e.* as soon as a fiber has sedimented down to a distance from the wall where wall contact occurs the fiber will take on lower values of C. After a sufficient amount of time the fiber will be located at the wall oriented along the direction of vorticity. This could explain the increased number of fibers at the wall oriented close to perpendicular to the flow direction for case A and B in the experiments.

Looking at figure 12 (c) for $r_p \approx 30$, with the no slip condition implemented in the contact, the results are quite different as compared to (a) and (b). For

a longer fiber Re_l is larger and the inertial term is larger in the computations. Therefore dC/dt is positive in a larger fraction of the space shown in the figure. A feature worth noticing is that the thick line crosses the dashed line in 12 (c). This indicates that even after a fiber with small values of β_{min} has sedimented down to a y-position where wall contact occurs it will not tend to adopt lower values of C. Consequently, the fiber would not be expected to settle all the way down to the wall since it will stay close to the dashed line and β will not tend to increase but rather decrease.

Possibly this could explain the absence of fibers with $r_p \approx 30$ near the wall in figure 6. However, when implementing the free slip condition, which causes a stronger drift towards lower C than the no slip condition, the situation is changed. This is shown in figure 12 (d) where it is seen that for this case a fiber takes on lower values of C as soon as the wall contact is included in the computations, similar to the situation in (a) and (b).

The nature of the fiber-wall contact and how well the two implemented models capture the fiber dynamics is presently not clear. A slender body approach was used by Carlsson & Koch to estimate the rotation and translation of the fiber near the wall. In order to obtain a more accurate description, it may be necessary to take into consideration that the fiber has a finite thickness when one of the fiber end points is positioned very close to the wall.

4. Conclusions

In a slowly sedimenting fiber suspension flowing down an inclined wall, the fiber orientation has been analyzed in planes parallel to the wall. Due to an upstream contraction of the flow the fibers were initially oriented close to the flow direction. Farther downstream this orientation was still found to be the most probable for distances larger than half a fiber length from the wall. For fibers with $r_p \approx 7$ a clear change in the orientation distribution is found closer to the wall. At distances farther from the wall than $y/l \approx 0.5$ most of the fibers are close to aligned with the flow and at distances closer to the wall than about an eighth of a fiber length most of the fibers are oriented perpendicular to the flow direction.

An increased concentration of fibers was also found near the wall due to the sedimentation. A large fraction of the shorter fibers with $r_p \approx 7$ were found at the wall. This was not the case for fibers with $r_p \approx 30$ where most of the fibers were detected at distances farther from the wall than about half a fiber length. The fiber orientation results are in qualitative agreement with the studies by Holm & Söderberg (2007) and Carlsson et al. (2007). Also in these studies fibers were detected at orientations close to perpendicular to the flow direction in the near wall region. Carlsson et al. only performed measurements on one fiber suspension with $r_p \approx 7$ and $nl^3 \approx 0.25$ and in comparison to Holm & Söderberg more statistics have been added and a more accurate method to determine the fiber distance from the wall has been used.

Sedimentation towards the wall and fluid inertia have been presented as two physical mechanisms that could influence the orientation of fibers in the presence of a wall. An estimation of the drift in orientation of a fiber was performed based on theoretical predictions by Subramanian & Koch (2005) and Carlsson & Koch (2009). A likely reason for the accumulation of fibers oriented perpendicular to the flow direction for $r_p \approx 7$ is the density difference between the fibers and the fluid. When a fiber sediments towards the wall the reflection of the fluid velocity disturbance and the wall contact during the flip causes the fiber to migrate towards lower values of C (larger values of β). On the other hand fluid inertia will tend to drift the orientation so that C increases with time. This is presented as a possible reason to why few fibers in the experiments with $r_p \approx 30$ are found at the wall.

It should also be recalled that the wall normal distance of the fibers have been normalized with the fiber length. Therefore, the residence time of a fiber at y/l, will be about four times longer for fibers with $r_p \approx 7$ as compared to fibers with $r_p \approx 30$. Another difference is that the number of completed periods of rotation will be about 16 times as many for a fiber with $r_p \approx 7$ at y/l than for a fiber with $r_p \approx 30$, since T_J is almost linearly proportional to r_p from equation (3). Since the residence time is shorter and the number of rotation periods is less, for fibers with $r_p \approx 30$, it is also reasonable to expect that less fibers have time to settle to the wall.

Still, the difference in the amount of detected fibers at the wall appears surprisingly large. An experiment where the longer fibers have time to complete more periods of rotation is needed in order to verify the presented hypothesis of competition between (i) sedimentation towards the wall, wall contact and (ii) fluid inertia. The results suggest that the combined effect of sedimentation towards the wall and fluid inertia could be a focus area of future studies.

Acknowledgments

The authors acknowledge helpful discussions with Professor Donald L. Koch and Dr. Richard Holm. This work has been supported by the European Union FP6 project EcoTarget, contract number 500345 (NMP2-CT-2004-500345) (AC and FL) and by the Swedish Research Council, contract number VR-2005-5816 (FL).

References

- ACHESON, D. J. 1990 Elementary Fluid Dynamics, 38-40. Oxford University Press.
- ALTENBACH, H., NAUMENKO, K., PYLYPENKO, S. & RENNER, B. 2007 Influence of rotary inertia on the fiber dynamics in homogenous creeping flows. Z. Angew. Math. Mech 87 (2), 81–93.
- ANCZUROWSKI, E. & MASON, S. G. 1968 Particle motions in sheared suspensions. XXIV. Rotation of rigid spheroids and cylinders. *Trans. Soc. Rheology* **12** (2), 209–215.
- BINDER, R. C. 1939 The motion of cylindrical particles in viscous flow. *J. Appl. Phys.* **10**, 711–713.
- Bretherton, F. P. 1962 The motion of rigid particles in a shear flow at low Reynolds number. *J. Fluid Mech.* 14, 284–304.
- Carlsson, A. & Koch, D. L. 2009 Orbit drift of a slowly settling fiber in a wall-bounded shear flow. Manuscript in preparation.
- Carlsson, A., Lundell, F. & Söderberg, L. D. 2007 Fiber orientation control related to papermaking. *J. Fluids Eng.* **129** (4), 457–465.
- Carlsson, A., Lundell, F. & Söderberg, L. D. 2009 Evaluation of steerable filter for detection of fibres in flowing suspensions. Manuscript in preparation.
- Chwang, A. T. 1975 Hydrodynamics of low-Reynolds-number flow. Part 3. Motion of a spheroidal particle in quadratic flows. *J. Fluid Mech.* **72**, 17–34.
- Dabros, T. 1985 A singularity method for calculating hydrodynamic forces and particle velocities in low-Reynolds-number flows. J. Fluid Mech. 156, 1–21.
- Gavze, E. & Shapiro, M. 1997 Particles in a shear flow near a solid wall: Effect of nonspherity on forces and velocities. *Int. J. Multiphase Flow* **23** (1), 155–182.
- Gavze, E. & Shapiro, M. 1998 Motion of inertial spheroidal particles in a shear flow near a solid wall with special application to aerosol transport in microgravity. *J. Fluid Mech.* **371**, 59–79.
- HARRIS, J. B. & PITTMAN, J. F. T. 1975 Equivalent ellipsoidal axis ratios of slender rod-like particles. J. Coll. Interf. Sci. 50 (2), 280–282.
- HOLM, R. & SÖDERBERG, D. 2007 Shear influence on fibre orientation. *Rheol. Acta* 46, 721–729.
- HSU, R. & GANATOS, P. 1989 The motion of a rigid body in viscous fluid bounded by a plane wall. J. Fluid Mech. 207, 29–72.

- HSU, R. & GANATOS, P. 1994 Gravitational and zero-drag motion of a spheroid adjacent to an inclined plane at low Reynolds number. J. Fluid Mech. 268, 267–292.
- Jacob, M. & Unser, M. 2004 Design of steerable filters for feature detection using Canny-like criteria. *IEEE T. Pattern Anal.* **26** (8), 1007–1019.
- Jeffery, G. B. 1922 The motion of ellipsoidal particles immersed in a viscous fluid. *Proc. Roy. Soc. London A* **102** (715), 161–179.
- Moses, K. B., Advani, S. G. & Reinhardt, A. 2001 Investigation of fiber motion near solid boundaries in simple shear flow. *Rheol. Acta* 40, 296–306.
- POZRIKIDIS, C. 2005 Orbiting motion of a freely suspended spheroid near a plane wall. J. Fluid Mech. **541**, 105–114.
- QI, D. & Luo, L. S. 2003 Rotational and orientational behaviour of threedimensional spheroidal particles in Couette flows. J. Fluid Mech. 477, 201–213.
- RAHNAMA, M., KOCH, D. L. & SHAQFEH, E. S. G. 1995 The effect of hydrodynamic interaction on the orientation distribution in a fiber suspension subject to simple shear flow. *Phys. Fluids* **7**, 487–506.
- Stover, C. A. & Cohen, C. 1990 The motion of rodlike particles in the pressure-driven flow between flat plates. *Rheol. Acta* 29, 192–203.
- Subramanian, G. & Koch, D. L. 2005 Inertial effects on fibre motion in simple shear flow. *J. Fluid Mech.* **535**, 383–414.
- Subramanian, G. & Koch, D. L. 2006 Inertial effects on the orientation of nearly spherical particles in simple shear flow. *J. Fluid Mech.* **557**, 257–296.
- TAYLOR, G. I. 1923 The motion of ellipsoidal particles in a viscous fluid. *Proc. Roy. Soc. London A* 103, 58–61.
- TREVELYAN, J. & MASON, S. G. 1951 Particle motions in sheared suspensions I. Rotations. J. Colloid Sci. 6, 354–367.

Orbit drift of a slowly settling fibre in a wall-bounded shear flow

By Allan Carlsson[†] & Donald. L. Koch[‡]

[†]Linné Flow Centre, KTH Mechanics, SE - 100 44 Stockholm, Sweden [‡]School of Chemical Engineering, Cornell University, Ithaca, NY 14853, USA

The orbit drift of a slowly settling fibre in a wall-bounded shear flow is estimated using a slender body approach. A local contact force is also introduced at the fibre end point to prevent the fibre end from penetrating the wall during rotation. It is shown that this will tend to make a fibre drift across orbits and finally end up close to the wall aligned with the vorticity axis. The results are in qualitative agreement with previously reported experimental results by Holm & Söderberg 2007 Rheol. Acta 46, 721-729 and Carlsson, Lundell & Söderberg 2007 J. Fluids Eng. 129 (4), 457-465.

1. Introduction

This work is a first attempt of understanding the underlying physical mechanisms for the near wall dynamics of slowly settling fibres in shear flows. Considerable attention has been given to understand the dynamics of elongated particles suspended in flowing suspensions. A study which is frequently used as a starting point is the article by Jeffery (1922). Jeffery derived governing equations of motion for an isolated ellipsoid suspended in an unbounded simple shear flow. The particle was assumed to be neutrally bouyant in a Newtonian fluid and all inertial effects were assumed negligible. The equations, frequently referred to as Jeffery's equations, have later been extended by Bretherton (1962) to be valid for almost any axi-symmetric particle with a for-aft symmetry if an effective aspect ratio is introduced. This includes fibres with a cylindrical shape. The equations have been validated in several experimental studies, e.g. Trevelyan & Mason (1951), Goldsmith & Mason (1962) and Anczurowski & Mason (1968).

Some attention has also been given to wall-bounded shear flows. An interesting experimental observation is that slowly sedimenting fibres will tend to orient themselves aligned with the vorticity axis close to the wall, e.g. Holm & Söderberg (2007) and Carlsson, Lundell & Söderberg (2007, 2009). Carlsson et al. studied fibre orientation in planes parallel to the wall and showed that the fibres kept an orientation close to the flow direction down to distances of half a

fibre length from the wall. Closer to the wall the set of possible Jeffery orbits without hitting the wall is reduced. It was shown that the fibres adopted possible orientations within this reduced set of Jeffery orbits. In the very proximity of the wall the fibres were nearly parallel to the vorticity axis. An increased fibre concentration was also found at the wall. In order for fibres to be able to settle at the wall there has to be a physical mechanism that makes a fibre, initially close to the flow direction, migrate across orbits and end up close to the wall aligned with the vorticity axis.

Yang & Leal (1984) studied the motion of a slender body near a fluid-fluid interface. By letting the viscosity of one of the fluids tend to infinity the motion of a fibre in a wall-bounded shear flow could be computed. It was found that the shear induced wall reflection leads to a small perturbation to the orbit found by Jeffery and also gives periodic translational motions. However, these effects are small and do not lead to a cumulative drift in orientation over successive orbits and can therefore not explain the observation by Carlsson et al. (2007). This can also be inferred from the study by Pozrikidis (2005) who studied the motion of a neutrally buoyant prolate spheroid near a plane wall. A result from this study was that the period of rotation was also slightly longer as compared to the period in an unbounded shear flow. Additional numerical studies have also been performed on prolate spheroids where the major axis has been restricted to be oriented in the flow-gradient plane, e.g. Dabros (1985), Hsu & Ganatos (1994) and Gavze & Shapiro (1997, 1998).

There are also some additional experimental studies on fibre dynamics near solid walls. Stover & Cohen (1990) and Moses, Advani & Reinhardt (2001) both verified that the analysis of Jeffery is a good approximation for distances from the wall greater than one fibre length. Closer to the wall Stover & Cohen noted that Jeffery's equations still formed a good base although the period of rotation was found to be longer. Fibres closer to the wall than half a fibre length and oriented in the flow direction were found to interact with the wall in what was referred to as a "pole vaulting" motion, where the fibre moves away from the wall to a point where the fibre centre is located at half a fibre length from the wall. This motion is irreversible and cannot be explained only taking into account a Stokes flow interaction with the wall. This imply that the fibre interacts with the wall by direct mechanical contact. That lubrication forces are not expected to prevent the fibre from making contact with the wall can also be deduced from Harlen, Sundararajakumar & Koch (1999). A discussion on short-range interactions between fibres is provided and it is concluded that lubrication forces become significant only when fibres are nearly aligned.

Slender body theory is a useful tool to model the motion of fibres and has been applied near solid walls. Blake (1974) derived the image system for a slender body near a wall by introducing a mirrored image fibre to cancel the flow disturbance generated by the fibre at the wall and thereby satisfy the noslip condition at the wall. The image system by Blake has been used by for

instance Russel $et\ al.\ (1977)$ to predict the translation and rotation of fibres sedimenting near a vertical wall, i.e. with the gravity vector parallel to the wall. Two types of motions were found. A fibre approaching the wall at small angles turned to a vertical orientation and moved away from the wall as the fibre continued to turn. This was referred to as a "glancing" turn. For larger approaching angles there was a close interaction of the leading fibre end with the wall, causing the fibre to pivot and later move away from the wall with the opposite fibre end leading. The two types of motions were also observed experimentally in a qualitative agreement with the theory.

However, no non-hydrodynamic interaction with the wall is considered in these studies. Since the fibres under study by Carlsson *et al.* (2007, 2009) did not appear to alter their orientation until they were at a distance from the wall where solid body contact is possible during rotation it is motivated to study this further. Here a slender body analysis is presented that estimates the orbit drift of a slowly sedimenting fibre in a shear flow near a solid boundary. A mirrored image fibre is introduced that cancels the vertical velocity component at the wall.

Furthermore, the fibre motion due to wall contact is estimated by adding a local contact force at the instant in time when a fibre end hits the wall. No near range hydrodynamic effects will be considered before the contact occurs. This is motivated by assuming that the fibre rotation due to the wall reflection is weak in comparison to the shear induced rotation. The effect of gravity to shear on the fibre rotation can be estimated by $\Gamma = \Delta \rho g d/\mu \dot{\gamma}$, where $\Delta \rho$ is the density difference between the fibre and the fluid, g is the constant acceleration of gravity and d is the fibre diameter. Furthermore, μ is the dynamic viscosity of the fluid and $\dot{\gamma}$ is the shear rate of the fluid.

2. Fibre rotation and translation

The present situation is illustrated in figure 1. A straight rigid fibre of length 2l, with its centre located at x, is suspended in a shear flow $U^s = \dot{\gamma} y e_x$, where $\dot{\gamma}$ is the shear rate of the fluid and y is the normal distance from the wall located at y=0. The density difference $\Delta \rho$ between the fibre and the surrounding fluid, in combination with the constant acceleration of gravity $g=-ge_y$, will make the fibre settle toward the wall. There will also be a velocity disturbance of the fluid reflected at the wall as the fibre moves in the fluid. This disturbance is denoted by U^w .

When a fibre is suspended in a viscous flow, the motion of the fluid will be disturbed by the presence of the fibre. The forces exerted on a fibre in a flow where fluid inertia can be neglected have been derived by for instance Batchelor (1970) and Cox (1970). We consider fibres whose length 2l is large compared to the fibre diameter d. The force per unit length of the fibre on the fluid can

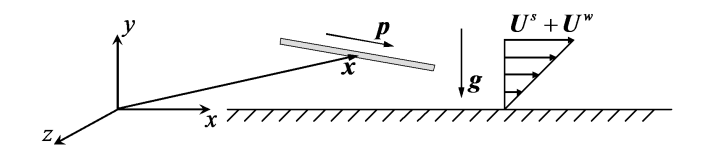


FIGURE 1. Schematic of sedimenting fibre in a shear flow near a wall.

be expressed as

$$f = \frac{4\pi\mu}{\ln(2r_p)} \left(\mathbf{I} - \frac{1}{2} p \mathbf{p} \right) \cdot \left(\mathbf{u} + \boldsymbol{\omega} \times \mathbf{p} s - \mathbf{U}^{\infty} \right), \tag{1}$$

where μ is the dynamic viscosity of the fluid, $r_p = 2l/d$ is the aspect ratio of the fibre, **I** is the unit matrix, p is a unit vector in the direction of the fibre and s is the position along the fibre, taking on values between -l and l. Furthermore, u and ω is the translational velocity of and the fibre rotation rate around the fibre centre, respectively, and U^{∞} is the undisturbed velocity field, *i.e.* the velocity of the fluid with the velocity disturbance due to the fibre itself excluded. Equation (1) is the leading order term in an expansion in terms of $1/\ln(2r_p)$. Hence, it is assumed that $\ln(2r_p) >> 1$.

Due to the linearity of Stokes equations the principle of linear superposition applies. As long as there is no contact between the fibre and the wall, linear superposition also applies to the motion of the fibre. This is based on that the rotation rate of the fibre is linear with respect to the fluid velocity. The superposition principle makes it possible to separate the problem into different parts. The shear induced rotation is given by Jeffery (1922) and will be repeated briefly below. The wall reflected velocity disturbance will also cause the fibre to rotate. There will be a velocity disturbance of the fluid introduced by the shear flow and also a disturbance because the fibre simultaneously settles toward the wall. Recall, that the wall reflection due to the shear flow will not cause a fibre to leave its orbit, *i.e.* the fibre end points will still form closed orbits, *e.g.* Yang & Leal (1984) and Pozrikidis (2005). Since, the shear induced reflection only leads to a small disturbance of the rotation rate given by Jeffery and does not lead to any orientation drift over successive orbits it is neglected in this study. Therefore, only the wall reflection due to the fibre settling is considered below.

$2.1.\ Rotation\ and\ translation\ of\ fibre\ in\ shear\ flow$

We begin by discussing the motion of a fibre in an unbounded simple shear flow given by U^s , *i.e.* there is no settling and no wall effects taken into account. Setting the net force and torque on the fibre to be zero equation (1) can be

used to derive solutions for the translation and rotation rate of the fibre

$$\dot{\boldsymbol{x}}_s = (\mathbf{E} + \boldsymbol{\Omega}) \cdot \boldsymbol{x} \tag{2}$$

$$\dot{\boldsymbol{p}}_{s} = \boldsymbol{\Omega} \cdot \boldsymbol{p} + \kappa \left(\mathbf{I} - \boldsymbol{p} \boldsymbol{p} \right) \cdot \left(\mathbf{E} \cdot \boldsymbol{p} \right). \tag{3}$$

 Ω and E are the vorticity and rate-of-strain tensors given by

$$\Omega = \frac{1}{2} \left((\nabla U^s)^T - \nabla U^s \right) \tag{4}$$

$$\mathbf{E} = \frac{1}{2} \left(\left(\nabla U^s \right)^T + \nabla U^s \right), \tag{5}$$

where ∇U^s is the velocity gradient tensor. Index s is here used to denote that equations (2) and (3) is the translation and rotation of the fibre due to the shear flow. The parameter $\kappa = \left(r_e^2 - 1\right)/\left(r_e^2 + 1\right)$ makes the equations valid also for small aspect ratios. With the assumptions we have already restricted ourselves to κ would naturally be equal to 1, but in order for the fibre to rotate through the xz-plane the correction term, which comes from Jeffery's analysis, is required and will therefore be used.

Equation (3) is the solution of Jeffery (1922) for the motion of a spheroidal particle with aspect ratio r_e . Bretherton (1962) showed that Jeffery's equations are valid for a large set of axisymmetric particles with a for-aft symmetry provided that an effective ellipsoidal aspect ratio that gives a relation between r_p and r_e is found. Some attention has been given in order to determine this relation for cylindrical particles, e.g. Trevelyan & Mason (1951), Anczurowski & Mason (1968), Cox (1971) and Harris & Pittman (1975). In this study the empirical relation of Harris & Pittman is used

$$r_e = 1.14r_p^{0.844}. (6)$$

Equation (6) was found to agree, by Harris & Pittman, with experimental data for r_p in the range between 1 and 120.

It is customary to introduce the polar angle θ between the fibre axis \boldsymbol{p} and the vorticity direction \boldsymbol{e}_z and the dihedral angle ϕ between the flow-vorticity and fibre-vorticity planes. With these angles $\boldsymbol{p} = (\sin\theta\cos\phi, \sin\theta\sin\phi, \cos\theta)$ and equation (3) becomes

$$\dot{\phi}_s = -\frac{\dot{\gamma}}{r_e^2 + 1} \left(r_e^2 \sin^2 \phi + \cos^2 \phi \right) \tag{7}$$

$$\dot{\theta}_s = \frac{\kappa \dot{\gamma}}{4} \sin 2\theta \sin 2\phi. \tag{8}$$

When a fibre rotates according to equations (7) and (8) the fibre end points will form closed orbits in space. The orbits are often quantified by the Jeffery orbit constant

$$C = \frac{\tan\theta \left(r_e^2 \sin^2\phi + \cos^2\phi\right)^{1/2}}{r_e}.$$
 (9)

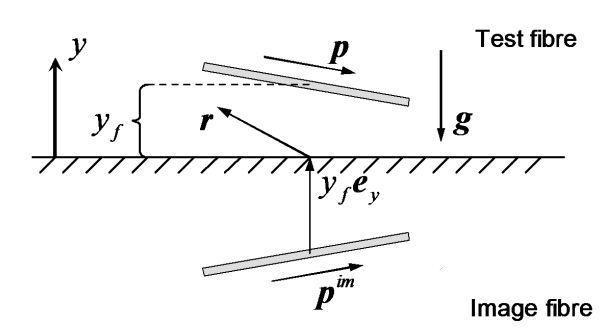


FIGURE 2. Hydrodynamic image of a fibre sedimenting toward wall.

A value of C=0 indicates that the fibre will spin around its own major axis aligned with the vorticity axis. As $C\to\infty$ the fibre will undergo a tumbling motion in the flow-gradient plane and form a circular orbit i this plane. The period of rotation for a fibre rotating in Jeffery orbits is not dependent on C and is given by

$$T = \frac{2\pi}{\dot{\gamma}} \left(\frac{r_e^2 + 1}{r_e} \right). \tag{10}$$

2.2. Rotation and translation of sedimenting fibre due to wall reflection

In this section it is taken into account that there is a density difference $\Delta \rho$ between the fibre and fluid. As the fibre settles toward the wall the velocity disturbance of the fluid will be reflected by the wall. The reflected velocity disturbance will affect the rotation and translation of the fibre. As mentioned previously the effect of settling will be considered to be weak in comparison to the effect of shear, i.e. $\Gamma << 1$. From equations (7) and (8) we know that a fibre will spend most of its time nearly aligned with the flow-vorticity plane. It is therefore reasonable to assume that most of the orbit drift, i.e. change of C, will take place when the fibre is oriented close to the flow-vorticity plane. Therefore $p_y << 1$ in the following analysis, where $p_y = \sin\theta\sin\phi$ is the y-component of the unit vector p along the fibre defined above. This assumption will be returned to.

Since the fibre is nearly aligned with the xz-plane $u \approx u_y e_y$ and $\dot{p} \approx \dot{p}_y e_y$. Therefore only the y-components will be considered in the analysis. With the last assumption it is also convenient to introduce a coordinate system (s,y,t), where s is parallel to the projection of the fibre in the xz-plane and t is orthogonal to both s and y.

Blake & Chwang (1974) studied the image system of flow singularities in the presence of a no slip wall. It was shown by Blake (1974) that the essential features for a slender body in a Stokes flow near a wall can be obtained by a point force distribution along the centreline of the fibre combined with a distribution of flow singularities along a mirrored image fibre in order to satisfy the no slip at the wall.

The physical fibre will be referred to as the test fibre and the hydrodynamic image will be referred to as the image fibre. The vertical velocity component at the wall will be zero by introducing a line distribution of point forces along the image fibre. The point forces on the image fibre must then be of equal magnitude but with opposite sign as compared to the point forces along the test fibre

In order to satisfy the no-slip at the wall a line distribution of force dipoles also have to be included on the image fibre. However, at this initial stage we only include a point force distribution to cancel the normal velocity component at the wall to see if a qualitative agreement with experiments can be obtained. The velocity field due to the force dipoles is of the same order of magnitude as the velocity field due to the point forces in the region of interest. Therefore, including force dipoles may also have an impact on the fibre motion. The effect of adding force dipoles will be addressed in a future study.

A line distribution of point forces is implemented on a mirrored image fibre in order to cancel the normal velocity component at the wall. The fluid velocity at a point in space r due to the image fibre can then be expressed as

$$U^{w}(\mathbf{r}) = \int_{-l}^{l} \mathbf{f}^{im} \cdot \mathbf{J}(\mathbf{r} + \mathbf{e}_{y}(y_{f} + s'p_{y}) - s'\mathbf{e}_{s}) ds', \tag{11}$$

where s' denotes the position along the image fibre and ${\bf J}$ is the Oseen tensor defined by

$$\mathbf{J}\left(\mathbf{r}\right) = \frac{1}{8\pi u r} \left(\mathbf{I} + \frac{\mathbf{r}\mathbf{r}}{r^2}\right). \tag{12}$$

The force on the fluid per unit length by the image fibre f^{im} is equal to f, only differing by an opposite sign of the y-component. Assuming that the density of the fibre is uniform the net force and torque on the test fibre can be expressed

$$\int_{-l}^{l} \mathbf{f} ds = \Delta \rho \mathbf{g} V \tag{13}$$

$$\int_{-l}^{l} s \boldsymbol{p} \times \boldsymbol{f} ds = 0. \tag{14}$$

where $V=\pi d^2l/2$ is the volume of the fibre. With f from equation (1) it is possible to compute the motion of a fibre, nearly aligned with the wall, as it settles toward the wall. It should be mentioned that the velocity disturbance, due to the wall reflection, is considered to be a far-field hydrodynamic effect. Consequently the analysis is only valid when the distance of the fibre centre to the wall $y_f >> d$. The effect of a finite thickness of the fibre could possibly

be of significance when the fibre rotates and one end nearly touches the wall. However, this effect will not be captured in the following analysis.

2.2a. Effect on fibre translation due to wall reflection. Equation (1) and (13) with $p_y = 0$ gives the translational velocity of the test fibre

$$u_y = -\frac{\ln(2r_p)}{8\pi\mu l}\Delta\rho gV + \bar{U}_y^w,\tag{15}$$

where \bar{U}_y^w is the average velocity disturbance, along the test fibre, due to the wall reflection given by

$$\bar{U}_{y}^{w}(y_{f}) = \frac{1}{2l} \int_{-l}^{l} U_{y}^{w}(s, y_{f}) ds.$$
 (16)

The wall reflection velocity U_y^w is given by equation (11). At this point y_f , s and s' are non-dimensionalized with l, which gives

$$U_y^w(s, y_f) = \frac{\Delta \rho g V}{16\pi \mu l} \int_{-(1+s)}^{1-s} \left[\frac{1}{\left(s''^2 + 4y_f^2\right)^{1/2}} + \frac{4y_f^2}{\left(s''^2 + 4y_f^2\right)^{3/2}} \right] ds'', \quad (17)$$

where s'' = s' - s. Note that y_f , s and s'' are the only non-dimensional quantities in equation (17). Solving the integrals in equations (16) and (17) finally yields the translational velocity of the test fibre

$$u_y = \frac{\Delta \rho g V}{8\pi \mu l} \left(\frac{1}{2} \ln \left[\frac{(1+y_f^2)^{1/2} + 1}{(1+y_f^2)^{1/2} - 1} \right] - \ln(2r_p) \right).$$
 (18)

2.2b. Fibre rotation due to wall reflection. The fibre will not rotate if $p_y=0$. Therefore a fibre that is close to aligned with the xz-plane, but not perfectly aligned will be considered in this section. Setting the net torque to be zero, see equation (14), with $p_y << 1$ the rotation of the test fibre is found to be

$$\dot{p}_y = \frac{3\Delta\rho gV}{4l^2} \int_{-1}^1 s ds \int_{-(1+s)}^{1-s} \mathcal{J}_{yy}(s'', 2y_f + s''' p_y, 0) ds'', \tag{19}$$

where s'' = s' - s and s''' = s + s'. J_{yy} is expanded in a Taylor series around $y = 2y_f$ which results in

$$J_{yy}(s'', 2y_f + s'''p_y, 0) \approx J_{yy}(s'', 2y_f, 0) + s'''p_y \frac{\partial J_{yy}(s'', 2y_f, 0)}{\partial y} + O(p_y^2),$$
(20)

where only the second term on the right-hand side will contribute to the rotation. Using equation (12) $\partial J_{yy}/\partial y$ is solved and the solution is put into

equation (19) which gives

$$\dot{p}_y = \frac{3p_y \Delta \rho g V}{32\pi \mu l^2} \int_{-1}^{1} \int_{-(1+s)}^{1-s} 2s \left(s'' + 2s\right) \left(\frac{y_f \left(s''^2 - 8y_f^2\right)}{\left(s''^2 + 4y_f^2\right)^{5/2}}\right) ds ds''. \tag{21}$$

Solving the integrals gives a final expression

$$\dot{p}_y = -\frac{p_y \dot{\gamma} \Gamma G}{r_p},\tag{22}$$

where once again $\Gamma = \Delta \rho g d/\mu \dot{\gamma}$ and

$$G(y_f) = -\frac{3}{32} \left[\frac{16y_f^2}{3} - \left(1 + y_f^2\right)^{1/2} \left(\frac{16y_f}{3} + \frac{4}{3y_f} \right) + 2y_f \ln \left[\frac{(1 + y_f^2)^{1/2} + 1}{(1 + y_f^2)^{1/2} - 1} \right] \right]. \tag{23}$$

Since ϕ is small $p_y \approx \phi \sin \theta$ and $\dot{p}_y \approx \dot{\phi} \sin \theta$. Consequently

$$\dot{\phi} \approx -\frac{\phi \dot{\gamma} \Gamma G}{r_p}.\tag{24}$$

There will also be a change in θ from equation (22). Since the fibre is oriented close to the flow-vorticity plane and θ is the polar angle from the fibre axis to vorticity, $\dot{\theta}$ will be comparable to $\dot{\phi}$ only when the fibre is close to the vorticity axis. It will be shown below that the fibre will tend to migrate toward a final orientation aligned with the vorticity axis. Therefore, the inclusion of $\dot{\theta}$ should not have a significant contribution to the solution until the fibre is already close to its final destination.

The function G will always have a positive sign implicating that the wall reflection will always tend to rotate the fibre toward $\phi = 0$. Since $\dot{\phi}$ is proportional to ϕ it can be worthwhile to return to the assumption of only computing the drift for $\phi << 1$.

A fibre rotating in a Jeffery orbit is characterized by the orbit constant C defined in equation (9). The angular variation required to cross a given amount of C-space is smaller when the fibre is nearly aligned with the xz-plane. Consider a fibre rotating with C=O(1). To change C by an O(1) amount, when $\phi=O(1/r_p)$ and near the xz-plane, ϕ has to change by an order of $1/r_p$. During the flip, when $\phi=O(1)$, ϕ has to change by an order of 1 to change C by the same amount. This implies that the orbit drift dC/dt due to the wall reflection will be of the same order both when the fibre is nearly aligned with the xz-plane and during the flip. In a Jeffery orbit a fibre spends a time of order $1/\dot{\gamma}$ rotating with $\phi=O(1)$ and a time of order $r_p/\dot{\gamma}$ with $\phi=O(1/r_p)$. Since the flip only occurs for a small fraction of the overall period and dC/dt is of the same order throughout the whole period most of the orbit drift will take place when the fibre is nearly aligned with the xz-plane.

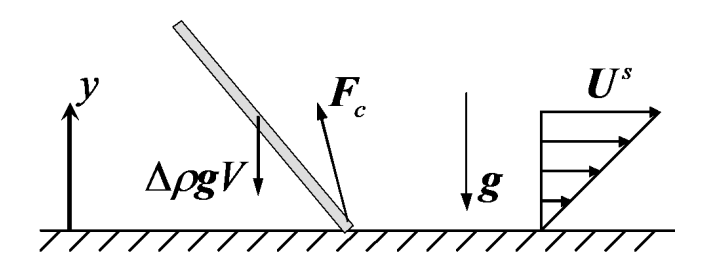


FIGURE 3. Schematic of wall contact due to rotation of fibre.

Now again consider that the fibre is also suspended in a shear flow. Superimposing $\dot{\phi}$ from equation (22) to Jeffery's equations results in the total rate of rotation

$$\dot{\phi} = -\frac{\dot{\gamma}}{r_e^2 + 1} \left(r_e^2 \sin^2 \phi + \cos^2 \phi \right) - \frac{\phi \dot{\gamma} \Gamma G}{r_p}$$
 (25)

$$\dot{\theta} = \frac{\kappa \dot{\gamma}}{4} \sin 2\phi \sin 2\theta. \tag{26}$$

This solution will be used to compute the orbit drift of the fibre when there is no contact with the wall. An order of magnitude analysis of equation (25), when $\phi = O(1/r_p)$, yields that the first term is $O(\dot{\gamma}/\Gamma_p)$ and the second term is $O(\dot{\gamma}\Gamma_p)$. The value of G ranges from about 0.1 to 1 for distances from the wall $y_f \approx 1$ and 0.1, respectively. Thus, Γ estimates the significance of the wall reflection in relation to the shear flow on the rotation of the fibre.

2.3. Rotation and translation of fibre due to wall contact

We will now address the situation when the fibre interacts with the wall by direct contact. The situation is illustrated schematically in figure 3. The wall contact is modeled by a local contact force \mathbf{F}_c . The net force and torque on the fibre is now given by

$$\int_{-l}^{l} \mathbf{f} ds = \Delta \rho \mathbf{g} V + \mathbf{F}_{c} \tag{27}$$

$$\int_{-l}^{l} s \boldsymbol{p} \times \boldsymbol{f} ds = l \boldsymbol{p} \times \boldsymbol{F}_{c}, \tag{28}$$

Again using equation (1) the fibre translation and rotation when the fibre end is in contact with the wall and $\kappa = 1$ is

$$\dot{\boldsymbol{x}} = \dot{\boldsymbol{x}}_s + \frac{\ln(2r_p)}{8\pi\mu l} \left(\mathbf{I} + \boldsymbol{p}\boldsymbol{p} \right) \cdot \left(\Delta \rho \boldsymbol{g} V + \boldsymbol{F}_c \right)$$
(29)

$$\dot{\boldsymbol{p}} = \dot{\boldsymbol{p}}_s + \frac{3\ln(2r_p)}{8\pi\mu l^2} \left(\mathbf{I} - \boldsymbol{p}\boldsymbol{p} \right) \cdot \boldsymbol{F}_c. \tag{30}$$

A boundary condition is required in order to compute F_c . The exact nature of the fibre-wall contact is not clear. Petrich & Koch (1998) used a Coulombic friction model to compute the interaction of contacting fibres and managed to get a good agreement with experimental data for the contact of a sedimenting synthetic fibre on a fixed strand of the same material. With Coulombic friction the contact will slip in the tangent direction if the tangent force exceeds a friction coefficient times the normal force. Below two cases will be studied corresponding to the limits of zero and infinite friction coefficient. It will thereby bracket the behaviour one might expect with Coulombic friction. These two cases will be referred to as a free slip and a no slip contact with the wall, respectively.

2.3a. No slip condition between wall and fibre end. It is here assumed that the fibre end will stick to the wall when there is contact, *i.e.* the velocity of the fibre end in contact with the wall $\dot{x} + l\dot{p} = 0$. Implementing this condition gives

$$\dot{\boldsymbol{x}} = \dot{\boldsymbol{x}}_s + l\boldsymbol{p}\boldsymbol{p} \cdot \mathbf{E} \cdot \boldsymbol{p} + \frac{3\ln(2r_p)}{32\pi\mu l} \left(\mathbf{I} - \boldsymbol{p}\boldsymbol{p} \right) \cdot \Delta \rho \boldsymbol{g} V$$
(31)

$$\dot{\boldsymbol{p}} = \dot{\boldsymbol{p}}_s - \frac{3\ln(2r_p)}{32\pi\mu l^2} \left(\mathbf{I} - \boldsymbol{p}\boldsymbol{p} \right) \cdot \Delta \rho \boldsymbol{g} V. \tag{32}$$

In terms of ϕ and θ equations (31) and (32) are

$$\dot{\boldsymbol{x}} = \dot{\gamma} y \begin{pmatrix} 1\\0\\0 \end{pmatrix} + \dot{\gamma} l \begin{pmatrix} \sin^3 \theta \cos^2 \phi \sin \phi\\ \sin^3 \theta \sin^2 \phi \cos \phi\\ \sin^2 \theta \cos \theta \sin \phi \cos \phi \end{pmatrix}
+ \frac{3\ln(2r_p)}{32\pi\mu l} \Delta \rho \boldsymbol{g} V \begin{pmatrix} \sin^2 \theta \sin \phi \cos \phi\\ \sin^2 \theta \sin \phi \cos \phi\\ \sin^2 \theta \sin \phi \end{pmatrix}$$
(33)

$$\dot{\phi} = -\dot{\gamma}\sin^2\phi + \frac{3\ln(2r_p)\cos\phi}{32\pi\mu l^2\sin\theta}\Delta\rho gV$$
 (34)

$$\dot{\theta} = \frac{\dot{\gamma}}{4} \sin 2\theta \sin 2\phi + \frac{3\ln(2r_p)\cos\theta\sin\phi}{32\pi\mu l^2} \Delta\rho gV. \tag{35}$$

It is once again emphasized that equations (33–35) is an estimation of the fibre translation and rotation when one of the fibre ends is in contact with the wall. This solution is applied at the moment in time when the y-position of the fibre end is first equal to zero, i.e. when $\mathbf{e}_y \cdot (\mathbf{x} + l\mathbf{p}) = 0$ or alternatively $y_f + l\sin\theta\sin\phi = 0$. At the moment when the y-component of the wall contact force is zero, i.e. when $\mathbf{e}_y \cdot \mathbf{F}_c = 0$, the contact is released. This condition can also be expressed $\mathbf{F}_c \neq 0$ as long as

$$F_y^c = \frac{4\pi\dot{\gamma}\mu l^2}{\ln(2r_p)} \left(\sin^3\theta \sin^2\phi \cos\phi\right) + \frac{\Delta\rho gV}{4} \left(1 + 3\sin^2\theta \sin^2\phi\right) > 0.$$
 (36)

It is noted, looking at equations (34) and (35) that if $\Delta \rho = 0$ the equations reduces to Jeffery's solution for $r_p >> 1$. That is without the settling toward the wall the fibre rotation would be given by Jeffery also during the wall contact. Although the net force on a fibre in an unbounded shear flow without gravity is zero, there is a tension inside the fibre preventing it from compressing and extending during rotation. The force per unit area on the fibre is parallel to the fibre orientation p. Thus, when there is no slip in the wall contact the contact force on the fibre will also be parallel to p. Therefore the contact force does not cause a torque and consequently it causes no rotation. When gravity is included in the force balance the contact force will not be parallel to p.

For the translation of the fibre given by equation (34) an additional term proportional to $\dot{\gamma}l$ appears. This term will translate the fibre to a distance from the wall where it is just possible for the fibre to move in Jeffery orbits without hitting the wall. This motion is qualitatively similar to the pole vaulting motion observed experimentally by Stover & Cohen (1990).

2.3b. Free slip condition between wall and fibre end. Here the extreme case where the fibre end is allowed to move freely in both the x and z-direction is considered, i.e. the tangential force is set to zero. The applied boundary condition is that the only non-zero component of the contact force is the y-component, i.e. $\mathbf{F}_c = (0, F_y^c, 0)$, and the fibre end velocity in the wall normal direction $\dot{y} + l\dot{p}_y = 0$. Applying these restrictions to equations (29) and (30) give the following expressions for the translation and rotation of the fibre

$$\dot{x} = \dot{\gamma}y \begin{pmatrix} 1\\0\\0 \end{pmatrix} + \frac{\dot{\gamma}l\sin^3\theta\sin^2\phi\cos\phi}{4 - 2\sin^2\theta\sin^2\phi} \begin{pmatrix} \sin^2\theta\sin\phi\cos\phi\\1 + \sin^2\theta\sin^2\phi\\\sin\theta\cos\theta\sin\phi \end{pmatrix}
+ \frac{3\ln(2r_p)}{16\pi\mu l} \Delta\rho g V \frac{(\sin^2\theta\sin^2\phi - 1)}{(2 - \sin^2\theta\sin^2\phi)} \begin{pmatrix} \sin^2\theta\sin\phi\cos\phi\\1 + \sin^2\theta\sin\phi\cos\phi\\1 + \sin^2\theta\sin\phi \end{pmatrix}
\dot{\phi} = -\dot{\gamma}\sin^2\phi + \frac{3\dot{\gamma}\sin^2\theta\sin^2\phi(\sin^2\phi - 1)}{2(\sin^2\theta\sin^2\phi - 2)}
+ \frac{3\ln(2r_p)}{16\pi\mu l^2} \Delta\rho g V \frac{(1 + \sin^2\theta\sin^2\phi)(\sin^2\phi - 1)}{\sin\theta\cos\phi(\sin^2\theta\sin^2\phi - 2)}
\dot{\theta} = \frac{\dot{\gamma}}{4}\sin 2\theta\sin 2\phi - \frac{3\dot{\gamma}\sin^3\theta\cos\theta\sin^3\phi\cos\phi}{2(\sin^2\theta\sin^2\phi - 2)}
- \frac{3\ln(2r_p)}{16\pi\mu l^2} \Delta\rho g V \frac{\cos\theta\sin\phi(1 + \sin^2\theta\sin^2\phi)}{(\sin^2\theta\sin^2\phi - 2)}.$$
(39)

As for the no slip condition the contact force is applied when $y_f + l \sin \theta \sin \phi = 0$ and is released when $F_y^c = 0$ where

$$F_y^c = \frac{4\pi\dot{\gamma}\mu l^2}{\ln(2r_p)} \left(\frac{\sin^3\theta \sin^2\phi \cos\phi}{2 - \sin^2\theta \sin^2\phi} \right) + \frac{\Delta\rho gV}{2} \left(\frac{1 + \sin^2\theta \sin^2\phi}{2 - \sin^2\theta \sin^2\phi} \right). \tag{40}$$

3. Numerical results

In this section the general features of the model derived in the previous section is investigated. This is followed up with a comparison with experimental results by Carlsson *et al.* (2009).

3.1. General features of theoretical model

As already mentioned a fibre suspended in an unbounded simple shear flow will not experience any orbit drift. For this case the parameter C will remain constant for an infinite time. All the additional terms found in the previous section, including the rotation due to hydrodynamic wall reflection and wall contact, will tend to lower values of C.

To start with we will consider the rotation of a fibre where only the wall reflection is taken into account. The fibre rotation is given by equations (25) and (26). The fibre is given an initial orientation given by $C_0=0.05$ and $\phi_0=0$ and is placed at $y_{f0}=0.75$. The particle aspect ratio is set to $r_p=100$ and $\Gamma=0.07$. The fibre will eventually sediment down to a y-position where it will make wall contact. Here the computation is stopped before this occurs. In figure 4 (a) and (b) the evolution of ϕ and θ is shown, respectively. The time is normalized with the Jeffery orbit period for large aspect ratios $T_{jef}=2\pi r_e/\dot{\gamma}$. The graphs qualitatively agree with Jeffery's solution for unbounded shear flow, where the fibre spend most of its time oriented near the xz-plane, i.e. $\phi << 1$. With regular intervals of $T_{jef}/2$ $\dot{\phi}$ is rapidly increased as the fibre flips around the vorticity axis.

In figure 4 (c) the evolution of p_x and p_y is shown. Clearly the fibre ends do not form closed orbits in this case. The amplitude of both p_x and p_y decreases for every period of rotation. Since the distance to the wall y_f is decreasing with time the orbit drift also becomes stronger with time. The fibre would finally end up aligned with the vorticity axis after a sufficiently long time. This is also indicated in figure 4 (d) where C is shown as a function of time. C will continue to decrease until C = 0 and $\theta = 0$.

It is seen that dC/dt=0 when $\phi=0$. This is natural since $\phi=0$ is the equilibrium orientation for a fibre settling toward the wall and $\dot{\phi}=0$ due to the reflection at this orientation. The change in C based on this model is largest during the flip where $\phi=O(1)$. However, returning to figure 4 (a) it is clear that the flip only takes place over a small fraction of the overall period and therefore most of the orbit drift still takes place when ϕ is small although separated from zero.

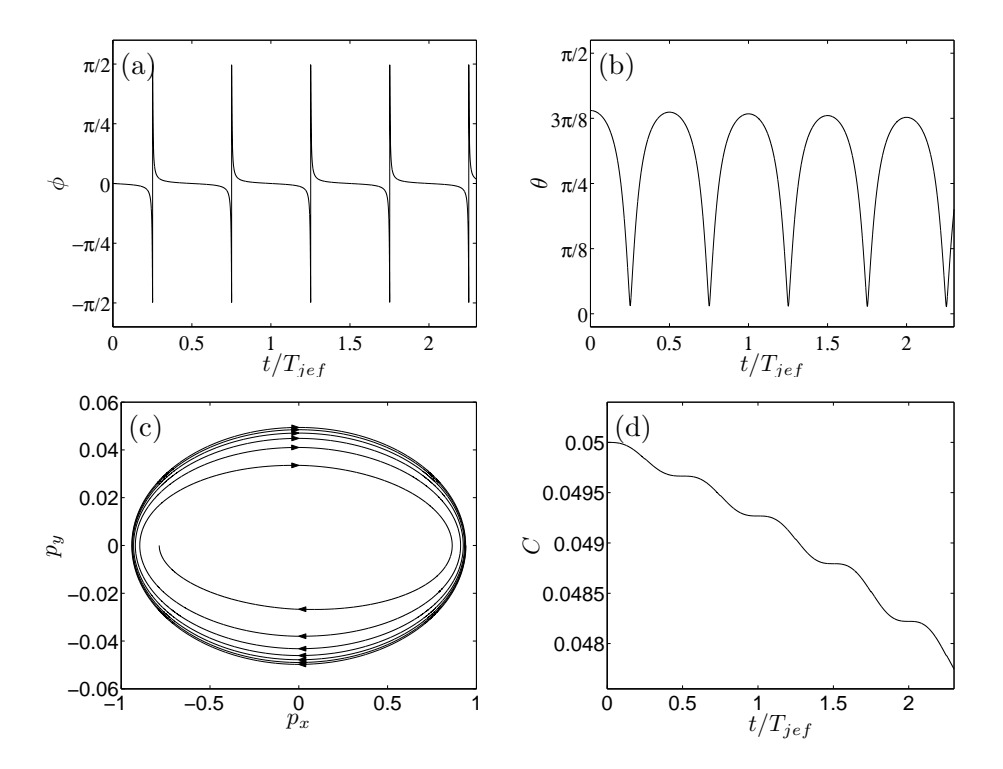
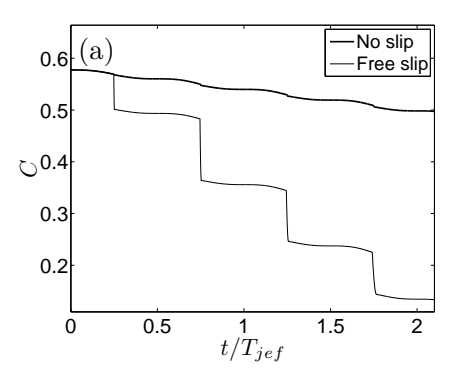


FIGURE 4. Orbit drift due to wall reflection. In (a) and (b) the evolution of ϕ and θ is shown, respectively and in (c) the evolution of the x and y-component of the unit vector \boldsymbol{p} is shown and in (d) the evolution of C.

Now the wall contact will also be considered. As before $r_p = 100$, the initial distance from the wall $y_{f0} = 0.5$ and $\Gamma = 0.14$. The initial fibre orientation in this plane is so that it would not, but barely, touch the wall during its rotation if it were neutrally buoyant. This is determined by the highest possible C a fibre near the wall can have, without touching the wall, given by $C = \tan(\sin^{-1}(y/l))$.

In figure 5 (a) the change of C with time is shown for both the no slip condition and the free slip condition, implemented when a fibre end is in contact with the wall. The thick and thin lines correspond to results from the no slip condition and free slip condition, respectively. The drift in C during the wall contact is larger with the free slip than the no slip condition. There is an additional drift during contact also due to the no slip condition although for this particular case the main orbit drift occurs due to the wall reflection.



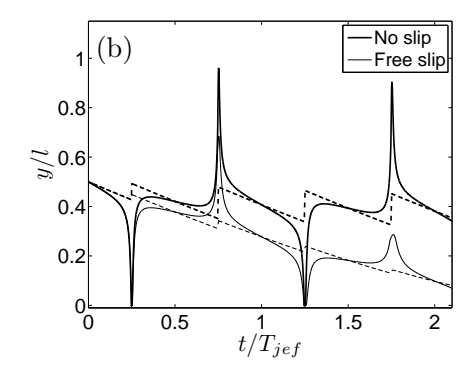


FIGURE 5. Orbit drift with wall reflection and wall contact for $\Gamma=0.14$. Results with the no slip condition is shown with a thick lines and results with the free slip condition are shown with thin lines. In (a) the evolution of C is shown and in (b) the y-position of one fibre end (solid) and the y-position of the fibre centre (dashed) is shown.

In figure 5 (b) the distance from the wall of the fibre centre (dashed lines) and one of the fibre ends (solid lines) are shown for both conditions. It is seen that the decrease in C during the contact is coupled to how much the fibre centre lifts during the contact. For the no slip condition this lift is larger, indicating that a fibre would take a longer time in order to settle down to the wall.

Just after the contact is released the fibre will rotate with a C close to the largest possible value without hitting the wall, i.e. $C \approx \tan(\sin^{-1}(y_f))$. This is the case for both contact conditions. It seems like the contact with the wall will never drift the fibre to a value lower than this C.

3.2. Comparison with experimental results

Carlsson et al. (2009) performed experimental measurements on slowly sedimenting fibres in a shear flow. A viscous liquid film with a thickness of about 17 mm was flowing down a slightly inclined plane, thereby generating a shear layer above the solid plane. The suspended fibres were about 0.5 mm long with an aspect ratio of $r_p \approx 7$. The suspension was dilute with $nl^3 \approx 0.001$, where n is the number density of fibres. The non-dimensional parameter $\Gamma \approx 0.007$.

The fibre orientation was measured at different distances from the wall in planes parallel to the wall. In this context it is convenient to introduce the orientation β which is defined as the angle from the flow direction to the projection of the fibre in the xz-plane, i.e. $\beta=0$ and $\pi/2$ when the fibre is aligned and perpendicular with the flow direction in this plane, respectively.

At the inlet a contraction was located to give the fibres an orientation closer to the flow direction.

Before applying the theoretical model to the experimental flow case it is once again emphasized that the theory is derived for slender bodies where $\ln(2r_p) >> 1$, which could be considered a weak assumption for $r_p \approx 7$. The validity of neglecting near range hydrodynamic effects, i.e. $y_f/d >> 1$, could also be discussed. This assumption is more reasonable for large aspect ratios since y_f/d can be large even when y/l is very small. It is also recalled that only the normal velocity component is zero at the wall. Still, the computation is carried out to see if some of the trends found experimentally can be qualitatively reproduced.

In order to compute the evolution of the C distribution as a function of y and how the concentration evolves it is necessary to define some inlet condition for these quantities. It will be assumed that the fibres are initially homogenously distributed across the shear layer at x=0, *i.e.* the concentration is initially constant with respect to y. In order to estimate the initial C distribution the study of Rahnama, Koch & Shaqfeh (1995) will be used. Rahnama et al. computed a steady state fibre orientation distribution for dilute and semi-dilute fibre suspensions in the limit of large aspect ratio

$$f(C) = \frac{RC}{\pi (4RC^2 + 1)^{3/2}},$$
(41)

where R is a fitting parameter. Assuming that the fibres are rotating in Jeffery orbits and that all phase angles are equally likely it is possible to determine R to get an approximative fit with the experimental β distribution. There are only measurements of β at x=0.75 m and none at the inlet upstream. For distances from the wall farther away than half a fibre length the β distribution does not change significantly in the experiments. To compute R only fibres that are located at y>2l is considered. The parameter R is chosen so that the single moment $\langle \cos^2\beta \rangle$ of the β -distribution is the same for the experiments and computations. This yields $R\approx 0.57$.

A comparison of the experimental β distribution with the theoretical for R=0.57 is shown in figure 6 (a). In figure 6 (b) the corresponding C distribution given by equation (41) for $R\approx 0.57$ is shown. Initially this distribution is assumed to be independent of y.

A large set of fibres is chosen at the inlet (x=0) of the experiments and the evolution of y and C is computed for each fibre until the corresponding x-position of the camera is reached. This is done for both the no slip and the free slip condition. The number of fibres entering the domain at each y position is proportional to $\dot{\gamma}y$ to represent the expected fibre flux for a homogeneous initial concentration.

In figure 7 the concentration c, normalized with the initial concentration of the suspension nl^3 , is shown. It is seen that both computations result in a

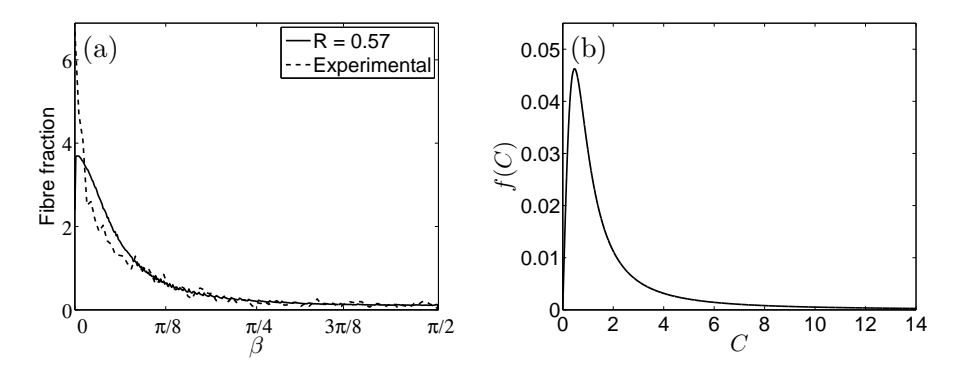


FIGURE 6. (a) β distribution with R=0.57 in equation (41) (solid) compared with experimental data (dashed) by Carlsson et al. (2009) and (b) f(C) for R=0.57.

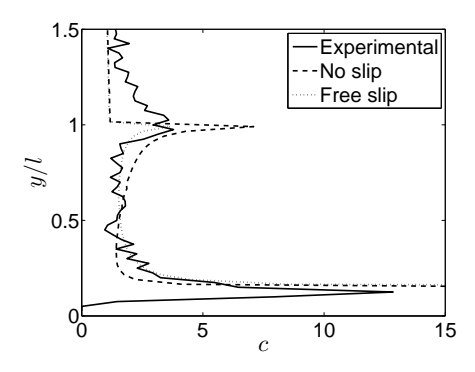


FIGURE 7. The fibre concentration as a function of the vertical distance to the wall y.

concentration very close to one for distances farther from the wall than y/l=1. Below this y position there is an increase of fibres due to the wall contact which pushes fibres with larger values of C from the wall during the flip in the rotations. As the distance to the wall is decreased farther the concentration drops until the very proximity of the wall, where there is a sharp increase in the concentration.

Looking at the experimental profile it seen that it is qualitatively similar to the computations. There are some thresholds set in the image analysis which make the absolute levels uncertain. A scaling has been introduced so that the average concentration in the region 1.5 < y/l < 2 is equal to 1. Also here there is an increase in c close to y/l = 1. In Carlsson $et\ al.\ (2009)$ this peak is

slightly above y/l=1, but moving the peak to y/l=1 is within the reported accuracy of the measurements. It is likely that this peak has its origin in a pole vaulting motion from the wall. The transition from values of $c\approx 1$ to the maximum value of c at $y/l\approx 1$ is gradual in the experiments. This could partly be due to inaccuracies in the measurements and the fibres also have a small length variation, which would make the peak in c less distinct. As in the computations there is also an increased concentration of fibres found in the proximity of the wall.

In figure 8 (a–f) the β distribution is shown for different distances from the wall. This is shown in terms of the cumulative distribution function $F(\beta) = P(B \le \beta)$ showing the probability that a fibre will be oriented between $\beta = 0$ and β . It is noted that the computed orientation distributions are not highly dependent on which wall contact condition that has been applied. For fibres in the region 2.0 < y/l < 2.5 in (a) the computed F is close to the experimental F. There is a small deviation between the two. Here it should be recalled that the value of F did not result in a perfect agreement with the F-distribution from the experiments.

In figure 8 (b), showing the region just above half a fibre length from the wall, the experimental distribution becomes more aligned with the flow direction. Note that the computational distributions coincide and do not change significantly as compared to the distribution farther from the wall in (a). This is since the fibres have not yet started to make wall contact.

Looking at 8 (c) just below half a fibre length from the wall it is seen that a similar shift toward lower values of β is seen, although now for the computational distributions. This may be somewhat surprising at first, considering that all fibres individually will tend to adopt lower values of C and consequently larger values of β . The reason for why this occurs in the model is coupled to the concentration profile in figure 7. The source of the increase in c just below y/l=1 is that fibres with relatively large values of C will do a pole vaulting like motion during the flip of their rotations. Due to the wall contact, the average settling speed toward the wall over the period of one rotation is also smaller for fibres rotating with larger values of C. Since fibres with larger C travel slower toward the wall there will be an increase in concentration of fibres with large C, whereas the concentration of fibres with small C will not be affected. A result of this is that the fraction of fibres with larger C will increase relative to fibres with smaller C, which also implies more fibres close to $\beta=0$ seen in the region below y/l=1.

Returning to 8 (b) a similar shift was seen for the experimental orientation distribution. It is likely that this shift is also due to a pole vaulting type of motion. It is seen in figure 7 that the concentration is high also above y/l = 1. An increase in concentration indicates that there are fibres in the region that have started to pole vault. This may be a surprising statement considering

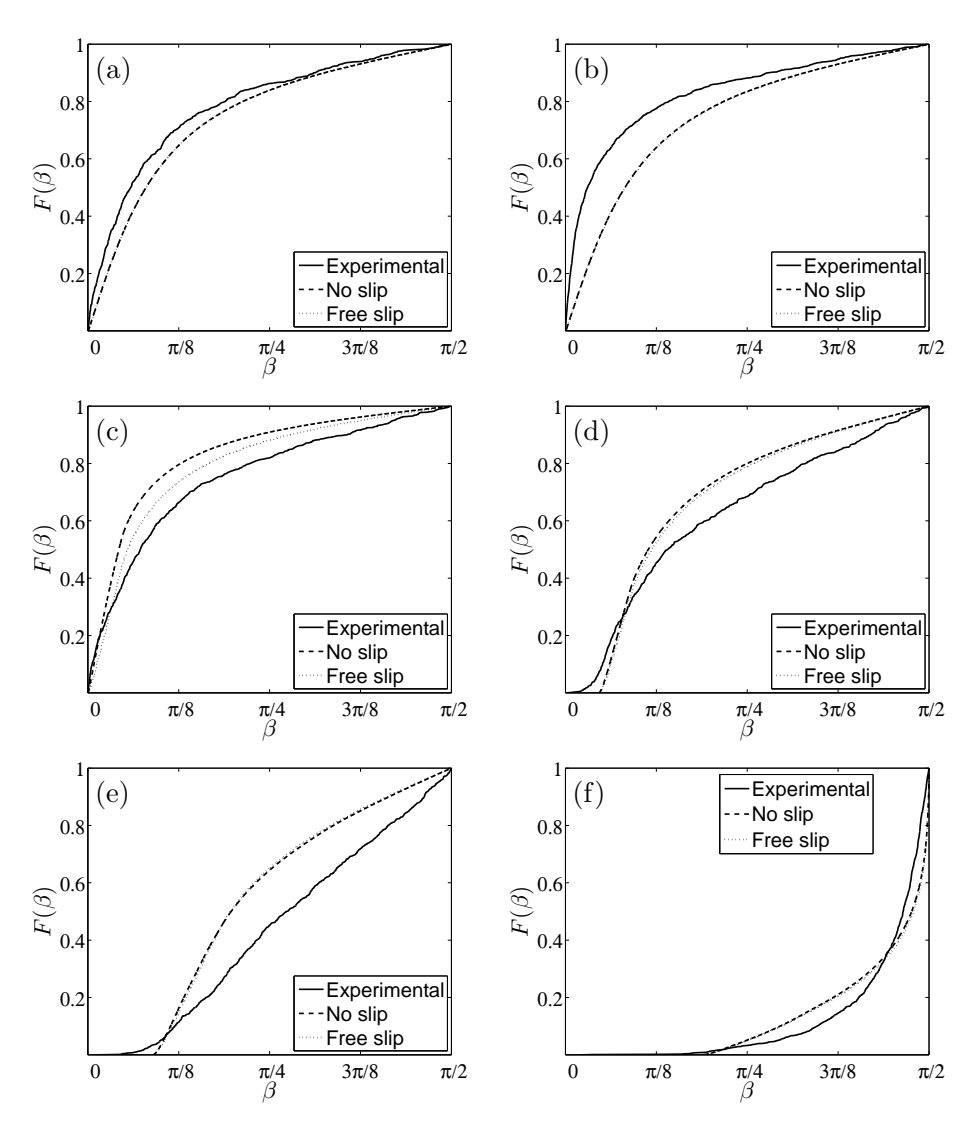


FIGURE 8. The cumulative distribution function $F(\beta)$ is shown for different distances from the wall: (a) 2.0 < y/l < 2.5 (b) 1.0 < y/l < 1.25, (c) 0.75 < y/l < 1.0, (d) 0.5 < y/l < 0.75, (e) 0.25 < y/l < 0.5 and (f) 0 < y/l < 0.25. Experimental data from Carlsson et~al. (2009) are shown as solid lines, computations with the no and free slip condition for the wall contact are shown as dashed and dotted lines, respectively.

that a fibre at y/l>1 can not make contact with the wall during rotation. Here it should be recalled that the measured y-position is not exact and that there is also a small length variation of the fibres. Thereby it is possible that some of the fibres in the region are actually slightly closer to the wall than the measured value, where wall contact is possible.

As the distance to the wall is decreased further in figure 8 (d–e) the computations continue to underestimate the drift, toward larger values of β , as compared to the experiments. In (f) showing the region closest to the wall most of the fibres have adopted large values of β . In the very proximity of the wall basically all fibres have $\beta \approx \pi/2$ in the experiments as well as in the computations, *i.e.* orientations close to the vorticity axis.

4. Concluding remarks

A slender body approach was used in order to estimate the motion of a sedimenting fibre in a wall-bounded shear flow. It has been assumed that inertia of the fluid is negligible and that the fluid motion is governed by Stokes flow equations. The velocity disturbance of the fluid as the fibre settles toward the wall is estimated by introducing an image fibre to cancel the vertical velocity component at the wall. In order to satisfy the no-slip on the wall a line distribution of force dipoles would also have to be placed on the image fibre. This will be returned to in a future study.

Due to the linearity of the problem the superposition principle is applied in order to estimate how the wall reflected velocity disturbance influences the fibre translation and rotation. Furthermore, a local contact force is implemented to account for the fibre-wall interaction that occurs when one fibre end point hits the wall. In the wall reflection analysis it is assumed that $\ln(2r_p) >> 1$ and $y_f >> d$. The effects of a fibre having a finite thickness are not taken into consideration. This could be of particular significance when a fibre end is located very close to the wall.

It has been shown that the wall reflection will tend to make a fibre migrate across orbits to lower values of C. The implemented wall contact model tends to enhance this drift in C. This leads to a final state where the fibre is aligned with the vorticity axis and spins around its main axis.

A numerical study based on the theoretical derivations was done for comparison with the experimental results by Carlsson et al. (2009). The aspect ratio of the fibres in the experiments are $r_p \approx 7$ and strictly speaking the present model is not valid for such small aspect ratios. Consequently, it is not expected to get a good quantitative agreement with the experiments. Still, some qualitative trends are reproduced. There is an increased concentration at roughly half a fibre length from the wall due to a pole vaulting like interaction with the wall. There is also an agreement in that the fibres closest to the wall are nearly aligned with the vorticity axis.

References

- ANCZUROWSKI, E. & MASON, S. G. 1968 Particle motions in sheared suspensions. XXIV. Rotation of rigid spheroids and cylinders. *Trans. Soc. Rheology* **12** (2), 209–215.
- BATCHELOR, G. K. 1970 Slender-body theory for particles of arbitrary cross-section in Stokes flow. J. Fluid Mech. 44, 419–440.
- BLAKE, J. R. 1974 Singularities of viscous flow. Part II: Applications to slender body theory. J. Eng. Math. 8 (2), 113–124.
- BLAKE, J. R. & CHWANG, A. T. 1974 Fundamental singularities of viscous flow. Part I: The image systems in the vicinity of a stationary no-slip boundary. *J. Eng. Math.* 8 (1), 23–29.
- Bretherton, F. P. 1962 The motion of rigid particles in a shear flow at low Reynolds number. *J. Fluid Mech.* **14**, 284–304.
- Carlsson, A., Lundell, F. & Söderberg, L. D. 2007 Fiber orientation control related to papermaking. *J. Fluids Eng.* **129** (4), 457–465.
- Carlsson, A., Lundell, F. & Söderberg, L. D. 2009 Orientation of slowly sedimenting fibers in a flowing suspension near a plane wall. Manuscript in preparation.
- Cox, R. G. 1970 The motion of a long slender body in a viscous fluid. Part 1. General theory. J. Fluid Mech. 44, 791–810.
- Cox, R. G. 1971 The motion of a long slender body in a viscous fluid. Part 2. Shear flow. J. Fluid Mech. 45, 625–657.
- DABROS, T. 1985 A singularity method for calculating hydrodynamic forces and particle velocities in low-Reynolds-number flows. J. Fluid Mech. 156, 1–21.
- GAVZE, E. & SHAPIRO, M. 1997 Particles in a shear flow near a solid wall: Effect of nonspherity on forces and velocities. *Int. J. Multiphase Flow* **23** (1), 155–182.
- Gavze, E. & Shapiro, M. 1998 Motion of inertial spheroidal particles in a shear flow near a solid wall with special application to aerosol transport in microgravity. *J. Fluid Mech.* **371**, 59–79.
- GOLDSMITH, H. L. & MASON, S. G. 1962 The flow of suspension through tubes. I. Single spheres, rods and discs. *J. Colloid Sci.* 17, 448–476.

- HARLEN, O. G., SUNDARARAJAKUMAR, R. R. & KOCH, D. L. 1999 Numerical simulations of a sphere settling through a suspension of neutrally buoyant fibres. *J. Fluid Mech.* **388**, 355–388.
- HARRIS, J. B. & PITTMAN, J. F. T. 1975 Equivalent ellipsoidal axis ratios of slender rod-like particles. *J. Coll. Interf. Sci.* **50** (2), 280–282.
- HOLM, R. & SÖDERBERG, D. 2007 Shear influence on fibre orientation. *Rheol. Acta* 46, 721–729.
- HSU, R. & GANATOS, P. 1994 Gravitational and zero-drag motion of a spheroid adjacent to an inclined plane at low Reynolds number. J. Fluid Mech. 268, 267–292.
- Jeffery, G. B. 1922 The motion of ellipsoidal particles immersed in a viscous fluid. *Proc. Roy. Soc. London A* **102** (715), 161–179.
- Moses, K. B., Advani, S. G. & Reinhardt, A. 2001 Investigation of fiber motion near solid boundaries in simple shear flow. *Rheol. Acta* 40, 296–306.
- Petrich, M. P. & Koch, D. L. 1998 Interactions between contacting fibers. ${\bf 10}$ (8), 2111-2113.
- POZRIKIDIS, C. 2005 Orbiting motion of a freely suspended spheroid near a plane wall. J. Fluid Mech. **541**, 105–114.
- RAHNAMA, M., KOCH, D. L. & SHAQFEH, E. S. G. 1995 The effect of hydrodynamic interaction on the orientation distribution in a fiber suspension subject to simple shear flow. *Phys. Fluids* **7**, 487–506.
- Russel, W. B., Hinch, E. J., Leal, L. G. & Tiefenbruck, G. 1977 Rods falling near a vertical wall. *J. Fluid Mech.* 83, 273–287.
- Stover, C. A. & Cohen, C. 1990 The motion of rodlike particles in the pressuredriven flow between flat plates. *Rheol. Acta* 29, 192–203.
- TREVELYAN, J. & MASON, S. G. 1951 Particle motions in sheared suspensions I. Rotations. J. Colloid Sci. 6, 354–367.
- Yang, S.-M. & Leal, L. G. 1984 Particle motion in Stokes flow near a plane fluid-fluid interface. Part 2. Linear shear and axisymmetric straining flows. *J. Fluid Mech.* 149, 275–304.

4

Fibre orientation near a wall of a headbox

By Allan Carlsson † , L. Daniel Söderberg † , ‡ & Fredrik Lundell †

[†]Linné Flow Centre, KTH Mechanics, SE - 100 44 Stockholm, Sweden [‡]STFI-Packforsk AB, SE - 114 86 Stockholm, Sweden

Experimental results on the fibre orientation in a laboratory scale headbox are reported. A steerable filter was used to determine the orientation of bleached unbeaten birch fibres at different distances from one of the inclined walls of the headbox contraction. Due to optical limitations only dilute suspensions were studied. It is shown that the fibre orientation distribution varies with the distance from the wall. Sufficiently far upstream in the headbox a more anisotropic distribution is found closer to the wall as compared to farther away from the wall.

1. Introduction

The mechanical properties of a paper sheet are highly dependent on the orientation distribution of fibres. The fibre orientation in the network structure is determined by the headbox and initial dewatering process, i.e. in the forming section of the paper machine. The main function of the headbox is to transform a pipe flow, with a diameter of about 0.8 m, into a free jet with a width of about 10 m and a thickness of 0.01 m. Due to the contraction in the nozzle of the headbox the suspension is accelerated and the positive rate-of-strain in the machine direction (MD) will tend to align the fibres with the flow direction. This orientation is often reflected in the final paper sheet, where most fibres are oriented in MD. It should be mentioned that the orientation is also affected by the dewatering process after the headbox. The free jet leaving the headbox impinges on one or between two permeable bands called wires. The water is drained through the wires resulting in a rapid increase of the suspensions fibre concentration. In an experimental study by Nordström (2003b) it was shown that the velocity difference between the jet and the moving wires have an effect on the fibre orientation. A larger velocity difference, both positive and negative, results in a more anisotropic paper sheet, i.e. more fibres oriented in MD. A smaller velocity difference, on the other hand, results in a more isotropic orientation distribution.

Some recent attention has been given to the fibre dynamics inside a headbox. The orientation distribution has been measured experimentally at the outlet of a headbox nozzle, Ullmar (1998). It was shown that increasing the headbox contraction rate resulted in higher anisotropy values. Furthermore, it was concluded that the flow rate through the headbox had a very small effect on the orientation distribution. Nordström (2003a) also reported that the effect of the flow rate on the fibre orientation in the final paper sheet was small.

A qualitative agreement with experimental data, concerning the orientation state of fibres in a headbox, was found analytically, Olson (1998), by neglecting effects of turbulence. The change of the orientation distribution in turbulent flows can be modeled with a Fokker-Planck type of equation, e.g. Krushkal & Gallily (1988) and Olson & Kerekes (1998). This has been done with application to headboxes by e.g. Olson et al. (2004), Brown (2005), Parsheh, Brown & Aidun (2005, 2006a,b) and Hyensjö et al. (2007). An accurate reproduction of experimental results has been obtained in these studies. In order to attain good results in these computations knowledge of turbulence quantities, in particular the turbulence intensity level at the inlet, is a prerequisite.

Nordström (2003b) showed that the orientation distribution is non-uniform over the thickness (Z) of the paper sheet. The sheet is generally more anisotropic in the core than on both sheet surfaces. This is also indicated in experimental measurements on the fibre orientation in a headbox jet by Asplund & Norman (2004). Along the centreline of the headbox a solid vane was inserted and in a region behind the vane the anisotropy was reduced. Aidun & Kovacs (1995) made a computational investigation and suggested that the main cause of a non-uniform fibre orientation in the cross direction (CD) is the secondary flows generated in the headbox due to the boundary layer formation along the side walls of the nozzle.

The present study aims at further investigating the wall influence on the fibre orientation. In many industrial headboxes a set of vanes are implemented as solid flow dividers in the headbox, mainly for the reason of damping out large scale motions that can lead to a bad paper formation. Boundary layers will form along all these vanes. The thickness of these boundary layers is of the order of 0.001 m. Considering that the thickness of the jet leaving the headbox is of the order 0.01 m a large fraction of the suspension is influenced by the boundary layers in the headbox. The vanes could therefore potentially have a large impact on the orientation distribution of fibres leaving the headbox and consequently also on the distribution in the final paper sheet.

Some attention has been given to the wall effect on the motion of fibres. For instance numerical studies have been performed by Hsu & Ganatos (1989, 1994), Gavze & Shapiro (1997) and Pozrikidis (2005). Experimental studies have also been done by Stover & Cohen (1990), Moses, Advani & Reinhardt (2001), Holm & Söderberg (2007) and Carlsson, Lundell & Söderberg (2007). These studies all have in common that they have been focusing on laminar viscous flow. There is still a lack of experimental data on near wall fibre

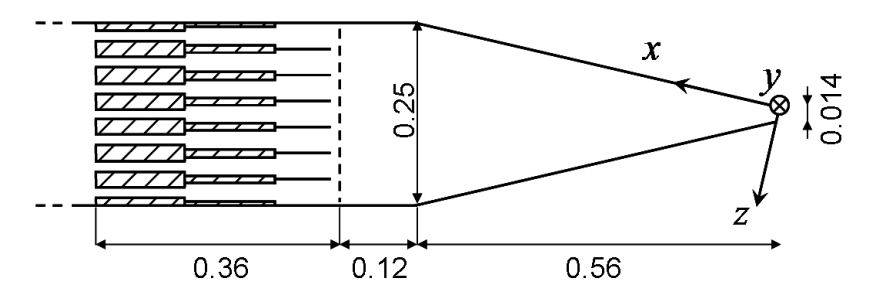


FIGURE 1. Schematic of the headbox with a coordinate system origininating at contraction outlet. Measures are in m.

orientation in flows where intertial effects can not be neglected. In this study the fibre orientation is measured along one of the walls of a laboratory scale headbox. Some preliminary results on practically the same experimental setup have been reported earlier in Carlsson, Söderberg & Lundell (2008).

2. Experimental section

2.1. Apparatus

A schematic of the headbox used is shown in figure 1. The same headbox was used in earlier studies by e.g. Ullmar (1998), Asplund & Norman (2004) and Carlsson et al. (2008), and consists of a tube bank and a contraction. In order to get optical access to the flow the walls are made of acrylic. The tube bank is divided in three sections; two circular and one square section. The contraction ratio R, defined as the ratio between the height at the contraction inlet divided with the height of the channel, is $R \approx 17$ at the outlet. A coordinate system is defined in the figure, where x runs upstream along the direction of the upper wall of the contraction and x=0 where the parallel section begins. The wall normal distance to the upper wall is denoted by z.

To visualize the flow a CCD camera (Prosilica GE680) with a lens of focal length 50 mm (Fujinon HF50HA-1B) was mounted above the wall at fixed x-positions. An extension tube was used in order to limit the field of view to approximately 1 cm². The camera was placed to capture images parallel to the wall in the centre of the channel in the spanwise direction (y), i.e. about 5 cm from both side walls.

To illuminate the field of view a light sheet was generated. The setup is sketched in figure 2. A monochromatic light beam ($\lambda=532$ nm), with an output power of the order 340 mW, is generated by a laser (Laserglow Technologies/Hercules - 325). The beam diameter is less than 1.5 mm and the full angle beam divergence is about 1 mrad which results in a diameter of about 2 mm at the position of the headbox. The beam is traversed to the desired z-position by an adjustable inclination of a 6 mm thick glass plate. A cylindrical

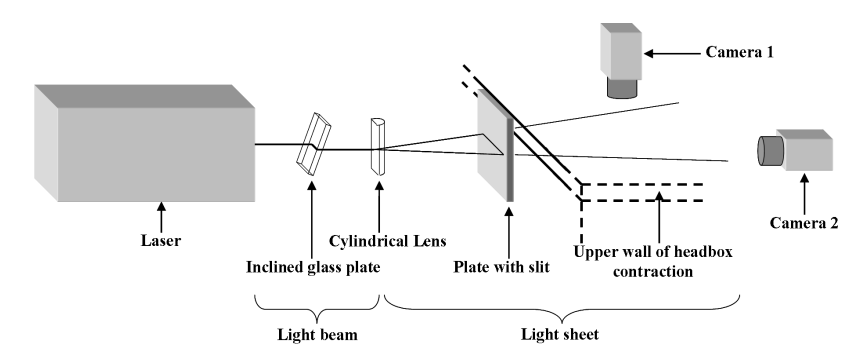


FIGURE 2. Schematic of the light sheet generation and camera positions.

lens of focal length 10 mm transforms the beam into a sheet parallel to the headbox wall. In order to reduce the thickness of the sheet it passes a slit with a thickness of 0.5 mm before entering the headbox. The slit can be traversed in the vertical direction with an accuracy of 0.01 mm. On the other side of the headbox a second camera is mounted in order to determine the centre position of the sheet in relation to the wall. This is done with an accuracy of about 0.1 mm. The thickness of the sheet as it exits the headbox is estimated to be around 2 mm. A linear interpolation gives a thickness of about 1.3 mm in the centre of the channel where the fibre orientation is studied. It should also be mentioned that the light intensity is not constant across the light sheet. The intensity is higher towards the centre of the sheet and as a consequence fibres are more easily detected near the centre of the sheet.

2.2. Suspension

A bleached unbeaten birch suspension was used in the study. A sample of the suspension was analyzed with L&W Fiber Tester. The probability density function (PDF) of the length of fibres is shown in figure 3. The arithmetic mean of the fibre length is $l_m \approx 0.7$ mm and the mean fibre width is $w_m \approx 18~\mu\text{m}$. The mass concentration of fibres was $c_m \approx 3 \cdot 10^{-5}$.

Another way to denote the concentration of a suspension is to use nl^3 , where n is the number density of fibres and l is a typical fibre length. The main reason for using this expression is that it is a better indicator of how frequent fibre-fibre interactions are than the mass concentration. Sometimes a crowding factor N is introduced for the same reason, see Kerekes & Schell (1992), where N only differs from nl^3 by a numerical factor, $N = \pi nl^3/6$. When $nl^3 << 1$ the suspension is generally considered dilute, e.g. Sundararajakumar & Koch (1997), and fibre-fibre interactions can usually be neglected. When $nl^3 = O(1)$ hydrodynamic fibre-fibre interactions occurs more frequently and

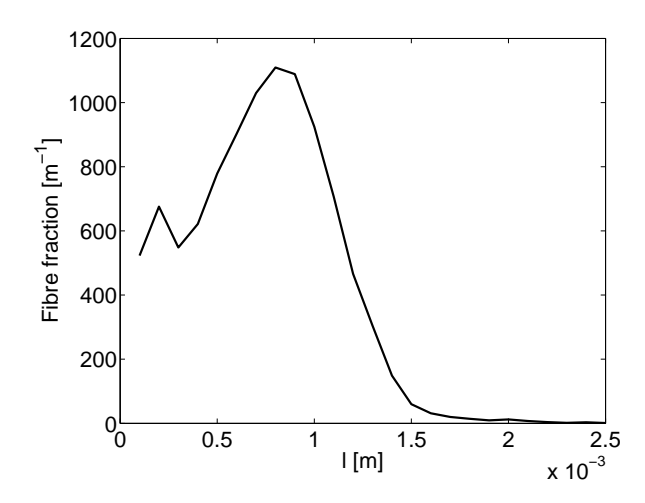


FIGURE 3. Length distribution of fibres in the suspension.

generally cannot be neglected. Eventually, if the concentration is increased even further, mechanical interactions between fibres also have to be considered.

In order to compute nl^3 the approximate relation $nl^3 \approx 1000 c_m l^2/k$ is used, where the density of the suspended fibres is estimated to be about 1000 kg/m³. With a fibre coarseness of $k \approx 100~\mu \rm g/m$ the concentration in the experiments is estimated to be $nl^3 \approx 0.15$. In industrial headboxes the concentration is typically between $c_m = 10^{-3}$ and 10^{-2} or $nl^3 \approx 5$ and 50, for suspensions with similar fibres as used in the present experiments. Consequently fibre-fibre interactions could have an effect on the fibre dynamics in the headbox of a paper machine, but are not expected to significantly influence the results in the present experiments.

2.3. Measuring and analyzing procedure

The fibre orientation and velocity were studied in planes parallel to the upper solid wall of the headbox at three different x-positions ($x=0.09,\ 0.25$ and 0.45 m). These x-positions correspond to contraction ratios of $R=4.9,\ 2.1$ and 1.3. At each x-position the centre of the laser sheet was traversed to five z-positions ($z=0.5,\ 1.0,\ 1.5,\ 2.0$ and 5.0 mm). Analyzing the images from camera 2, showing the light sheet as it exits the headbox, has revealed an unintended offset of 0.25 mm in z for x=0.45 m. This mistake results in that the z-positions, for x=0.45 m, have to be corrected to $z=0.25,\ 0.75,\ 1.25,\ 1.75$ and 4.75 mm. The value of z denotes the centre of the sheet where the light intensity is at its maximum. Recall that the light sheet is slightly thicker than 1 mm. This means that for the z-position closest to the wall a part of the

sheet is cut off by the wall. Consequently, the centre of the remaining light, illuminating only the fluid, will be slightly farther away from the wall than the reported z, where the light intensity is at its maximum. Therefore, the most appropriate value of z to report closest to the wall is not perfectly clear. In this context it should also be kept in mind that since the light intensity is not constant across the sheet it is more likely to detect a fibre close to the actual centre of the sheet, than anywhere else in the sheet, with the image analysis process.

To detect the orientation of the fibres in the images, a ridge detector within the class of steerable filters was used, Freeman & Adelson (1991). The particular detector used in this study was derived by Jacob & Unser (2004). The algorithm has been applied to fibre suspension flows and is described and evaluated in Carlsson *et al.* (2007, 2009). In this study the orientation β is analyzed and is defined as the angle from the x-direction in the plane parallel to the solid wall (xy-plane).

For the orientation measurements a total of 3000 images were captured at each (x,z)-position with a frame rate of the camera set low enough in order to get statistically independent images, *i.e.* low enough so that all of the fibres, which are captured in one image, will leave the field of view before the next image is captured. The frame rate ranges from 6 Hz (far upstream, close to wall) to 50 Hz (far downstream, far from wall). For the velocity measurements the frame rate is set to 200 Hz for all (x,z)-positions. Due to the increased velocity downstream it was not possible to obtain the velocity profile at x=0.09 m.

3. Results and discussion

3.1. Velocity

The volume flow rate during the experiments was $Q \approx 12.5 \cdot 10^{-3}$ m³/s, resulting in a jet velocity of 8.7 m/s (520 m/min). In order to get an estimation of the velocity profile near the wall individual fibres were tracked manually. Initially the intention was to use a particle image velocimetry algorithm (PIV) on seeding particles to measure the velocity field in the sheet. However, it was found difficult to attain a series of images good enough in order to use PIV. This could partly be due to that the concentration of seeding particles was slightly too large, but it is believed that the main source for the troubles using PIV is the large range of velocities within the light sheet. This is due to the high shear rate in the near wall region.

To be able to get some information about the velocity some individual fibres where tracked manually. The procedure to do this was to choose and mark a number of fibres in an image and search for these in the subsequent image. This turns out to be a time consuming method and therefore only 20 fibres per (x,z)-position were tracked. Measurements were conducted at x=0.25 and 0.45 m. Admittedly more fibres would have to be tracked in order to

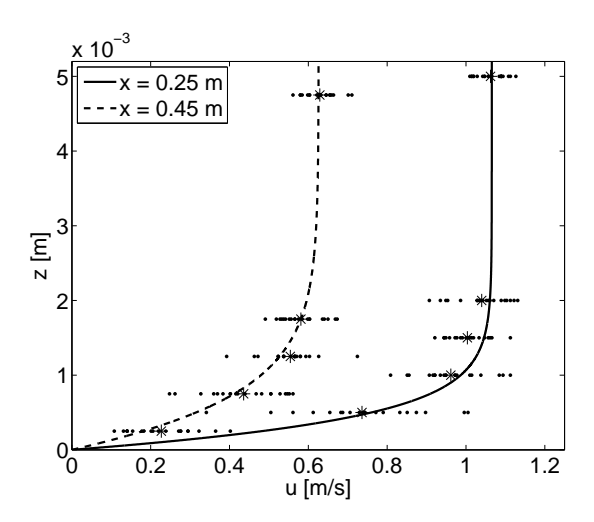


FIGURE 4. Theoretical velocity profiles for x=0.24 m (solid) and x=0.45 m (dashed). The dots and the stars denotes the velocities of individual fibres and the mean of all fibres in each particular serie, respectively.

reach statistical convergence. Still, the velocity measurements are reported to provide an estimation of the velocity gradient and boundary layer thickness near the wall.

The velocity profiles are shown in figure 4. The velocity of each individual fibre is shown as a dot in the figure and the mean value for each (x,z)-position is shown as a star. The solid and dashed lines, denoting the velocity at x=0.25 and 0.45 m, are given by the similarity solution for laminar flow in a two-dimensional convergent channel and can be found in Schlichting (1979). There is a significant scatter in the experimental data. This is in particular seen closest to the wall. It is believed that the scattering mainly reflects the wide range of velocities inside the sheet near the wall. The maximum error in velocity of a tracked fibre is estimated to be ± 0.1 m/s. There are no deviations from the mean value larger than this error for the position farthest away from the wall $(z \approx 5 \text{ mm})$. Consequently, no conclusions can be drawn directly from the data concerning any velocity fluctuations that may be present in the flow.

The measured mean velocity profile coincides surprisingly well with the similarity solution for laminar flow. A turbulent boundary layer subjected to strong acceleration can return to laminar-like conditions. The acceleration is often quantified by a non-dimensional parameter

$$K = \frac{2\nu \tan \psi}{q},\tag{1}$$

where ν is the kinematic viscosity of the fluid, ψ is half the contraction angle and q is the flow rate per unit width in the channel. Some studies have been made to find the critical value of K where the onset to relaminarization begins. Among these are Moretti & Kays (1965) who found an apparent re-transition to a laminar boundary layer for $K > 3.5 \cdot 10^{-6}$ and Parsheh (2001) who found the critical K to be about $3.1 \cdot 10^{-6}$. In the present study $K \approx 3.4 \cdot 10^{-6}$ so a relaminarization process is likely to be present. Since, the boundary layer already seems to have reached a profile close to the similarity solution for laminar flow at x = 0.45 and 0.25 m it is natural to assume that it will stay close to this solution also farther downstream at x = 0.09. From the similarity solution the boundary layer thickness, defined as the distance from the wall where the mean velocity is 0.99 times the velocity far from the wall, is computed to be 0.6, 1.3 and 2.3 mm for x = 0.09, 0.25 and 0.45 m, respectively.

3.2. Fibre orientation distribution

The number of detected fibres at all (x, z)-positions is shown in table 1. For most positions between 20000 and 40000 fibres are detected, *i.e.* roughly 10 fibres per image. The measurements at different x-positions have been conducted at different times. The suspension has been partly replaced in between the measurements. Although the concentration should be about the same for all measurements it is very approximative, so the absolute numbers should not be compared between different x-positions.

There is a trend for x=0.25 and 0.45 m that more fibres are detected as the distance to the wall is increased. This could possibly reflect an effect of migration towards areas with lower velocity gradients. However, the result should be interpreted with some care. Notable from the number of detected fibres at x=0.09 m is that here there is no clear trend and the numbers differ significantly between the z-positions. For x=0.09 m the boundary layer thickness is about 0.6 mm so the mean flow velocity gradient should be about the same for the four z-positions farthest from the wall. It is also noted that the number of detected fibres at x=0.45 m, z=0.25 mm, in comparison to the other positions, is small. Here it should be recalled that part of the light sheet is cut off by the wall and therefore less fibres are expected to be detected. Still, the number is surprisingly small even if the apparent trend of fewer detected fibres at high velocity gradients is taken into account.

A possible explanation for why so few fibres are detected at x=0.45 m and z=0.25 mm is that fibres close to the wall will undergo a pole vaulting like motion as the sheared fluid will tend to make a fibre rotate. In the rotation of a nearly flow aligned fibre one of the fibre ends hit the wall and the centre of the fibre is pushed away to a position of about half a fibre length from the wall. This kind of motion has been observed in viscous flows by for instance Stover & Cohen (1990). We will see later that most of the fibres are oriented close to the flow direction so the presence of a pole vaulting motion would not

Position	x = 0.09 m	x = 0.25 m	x = 0.45 m
$z^* = 0.5 \text{ mm}$	34196	24673	9584
$z^* = 1.0 \text{ mm}$	43142	26542	22354
$z^* = 1.5 \text{ mm}$	33246	27761	25656
$z^* = 2.0 \text{ mm}$	35911	38249	25756
$z^* = 5.0 \text{ mm}$	42340	39568	28033

Table 1. The number of detected fibres at all (x, z)-positions. The values of z is given by z^* apart from when x = 0.45 m for which $z = z^* - 0.25$ mm.

be surprising. This would for fibres with a length of about 0.7 mm generate a void close to the wall between z=0 and 0.35 mm, where there are few fibres present. Since the centre of the sheet, where the light intensity is highest, is located inside this void when z=0.25 mm this could result in a significant drop in the number of detected fibres.

We will now focus on the fibre orientation near the wall. The distribution of β is shown, for all positions, in figure 5. The distributions at $x=0.45,\,0.25$ and 0.09 m are shown in (a), (b) and (c), respectively. The various lines denote different z-positions. The distributions are a bit coarse and more detected fibres would be desired to get a better convergence. Still, some trends, which will be addressed below, can be deduced from the data.

The perhaps most surprising feature is the asymmetric appearance of the distributions at $x=0.45\,\mathrm{m}$ in (a). There is at present no clear explanation for this. Similar distributions have been observed in all pre-studies on the setup and was also reported in Carlsson et~al.~(2008). Measurements have also been made in the spanwise direction at $x=0.45\,\mathrm{m}$, but no clear difference has been seen as a function of y in these results. The distributions have not appeared to change appreciably in the region of $-0.04\,\mathrm{m} < y < 0.04\,\mathrm{m}$ at $x=0.45\,\mathrm{m}$, where y=0 in the centre of the channel. It is believed that the asymmetric distributions arises due to an asymmetry of the incoming flow. The tube package ends at about 0.25 m upstream from the measurements at $x=0.45\,\mathrm{m}$. Farther downstream at $x=0.25\,\mathrm{m}$ the orientations distributions have developed a more symmetric appearance.

Disregarding the asymmetric feature of the distributions, a clear trend is seen for both x=0.45 and 0.25 m. A more anisotropic distribution is found closer to the wall, *i.e.* the fibres tend to adopt orientations closer to the flow direction ($\beta=0$) for lower values of z. Possibly velocity fluctuations of the fluid could be of significance here. Fluctuations are most likely to result in a more isotropic fibre orientation distribution, at least if the velocity fluctuations are fairly isotropic in nature. If there are less fluctuations closer to the wall, in the relaminarizing boundary layer, this could result in a more isotropic distribution

farther from the wall. However, it is emphasized that even though the mean velocity profile is close to the laminar profile, it is still likely that turbulent structures remain in the flow, e.g. Warnack & Fernholz (1998) and Talamelli et al. (2002). Therefore this explanation is not perfectly convincing.

Another possibility that will briefly be presented here is related to the dynamics of fibres in shear flows. As mentioned above a fibre will rotate when the surrounding fluid is sheared. In a viscous flow a fibre is expected to spend most time oriented nearly aligned with the xy-plane during its rotation. It is also likely that most fibres will be relatively close to the flow direction when oriented in this plane. This is what one would expect for fibres rotating in Jeffery orbits, see Jeffery (1922). A fibre will rotate in Jeffery orbits when suspended in a viscous simple shear flow, when all inertial forces are negligible. Clearly it is not straightforward at all to neglect inertial forces in the present study.

Some recent studies have been made on the effect of fluid inertia on the rotation of elongated particles in shear flows, e.g. Ding & Aidun (2000), Qi & Luo (2003) and Subramanian & Koch (2005). Two conclusions from these studies is that a weak, but non-negligible fluid inertia, will tend to increase the period of rotation as compared to fibres rotating in Jeffery orbits and fluid inertia will also introduce an orientation drift towards the flow direction. In the present experiments inertial effects are expected to be larger as the distance to the wall is decreased, since the differences in velocity of the fluid over the fibre surface will be greater when the velocity gradient is large. Both conclusions mentioned from the studies on inertial effects should lead to a more aligned distribution near the wall. It is easily realized that a drift in orientation towards the flow direction would lead to a more aligned orientation distribution. Also an increased period due to inertia should lead to a higher anisotropy, since the increased period appears as an increased fraction of time oriented near the xy-plane, where a fibre is likely to be close to the flow direction even when rotating in a Jeffery-like orbit.

Farther downstream at x=0.09 m, shown in figure 5 (c), no clear difference can be seen for different z. The velocity gradient at the wall is increasing downstream so if the reasoning on inertial effects above is significant one might imagine there should be an even larger effect on the fibre orientation at x=0.09 m. Clearly this is not the case.

It should also be recalled that simultaneously, as the velocity gradient at the wall is increased, the boundary layer thickness is decreased in the downstream direction. According to the similarity solution of a planar converging channel the boundary layer thickness should be close to 0.6 mm at x=0.09 m. Consequently large velocity gradients, in the wall normal direction, are only expected to be present for the z-position closest to the wall. It is also worth noticing that at this x-position the boundary layer is thinner than the mean

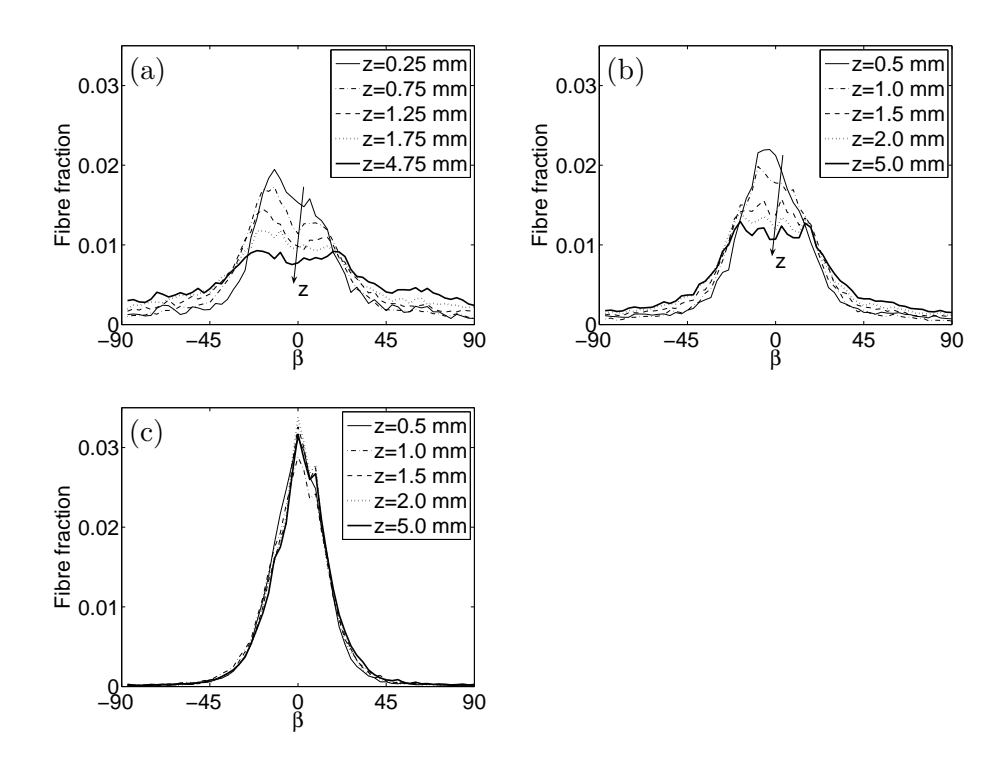


FIGURE 5. The orientation distribution of β for different wall normal positions z at (a) x=0.45 m, (b) x=0.25 m and (c) x=0.09 m.

fibre length and the thickness of the light sheet. Still, also the orientation distribution at z=0.5 mm coincide with the other z-positions. It is possible that the pole vaulting mechanism close to the wall could play a role also here. If the fibres tend to pole vault near the wall few fibres will be located in the region where the shear rate is strongest, but there should still be a small region of high shear in the light sheet where fibres should be present. Therefore this explanation is not completely satisfactorily.

So far attention has only been paid to the shear rate close to the wall and possible intertial effects on the fibre orientation. It was briefly mentioned in the introduction that the main mechanism for the alignment of fibres in a contraction is the streamwise rate-of-strain. The mean streamwise rate-of-strain is not constant in the headbox, but increases downstream. The rate-of-strain in the headbox is the reason for why the orientation distributions turn more anisotropic downstream, which is clearly seen in figure 5. Based on the mean flow velocity, given by the flow rate and geometry of the headbox, the mean

streamwise rate-of-strain is computed to about 1, 4 and 20 s⁻¹ for x = 0.45, 0.25 and 0.09 m, respectively. Since the strain rate increases downstream this means that the strength of the mechanism for fibre alignment with flow will also grow downstream. This could possibly be the reason to why no difference can be seen in the orientation, even for z = 0.5 mm, in figure 5 (c). A speculative explanation would be that the rate-of-strain is now the dominant term influencing the fibre orientation and that other effects, whether it being velocity fluctations, fluid inertia or something else, are small in comparison.

4. Concluding remarks

The fibre orientation has been studied experimentally close to one of the walls of a laboratory scale headbox. The flow rates in the experiments result in jet velocities which are comparable to velocities in industrial paper machines. Only low concentrations were studied due to optical issues and fibre-fibre interactions are therefore likely to have a small effect on the present results. It is concluded, for these low concentrations, that the orientation distribution changes with the distance from the wall for positions in the headbox sufficiently far upstream. The trend is that a more anisotropic distribution is found closer to the wall. This trend was not observed farther downstream at x=0.09 m, where the distribution was seemingly unaffected by presence of the wall. Due to the complexity of the flow only a speculative discussion have been made on possible reasons to why the orientation distribution varies with the wall normal distance. Fluid velocity fluctuations and their dependence on z have been discussed briefly. Also, the fibre dynamics in shear flows and the effect of fluid inertia have been addressed.

References

- AIDUN, C. K. & KOVACS, A. E. 1995 Hydrodynamics of the forming section: the origin of nonuniform fiber orientation. *Tappi J.* **78** (11), 97–106.
- ASPLUND, G. & NORMAN, B. 2004 Fibre orientation anisotropy profile over the thickness of a headbox jet. J. Pulp Paper Sci. 30 (8), 217–221.
- Brown, M. L. 2005 Dynamics of rigid fibres in a planar converging channel. PhD thesis, Georgia Institute of Technology, Atlanta.
- Carlsson, A., Lundell, F. & Söderberg, L. D. 2007 Fiber orientation control related to papermaking. *J. Fluids Eng.* **129** (4), 457–465.
- Carlsson, A., Lundell, F. & Söderberg, L. D. 2009 Evaluation of steerable filter for detection of fibres in flowing suspensions. Manuscript in preparation.
- Carlsson, A., Söderberg, L. D. & Lundell, F. 2008 Fibre orientation in the boundary layers of a planar converging channel. *PaperCon'08 TAPPI/PIMA/Coating Conference, Dallas*.
- Ding, E.-J. & Aidun, C. K. 2000 The dynamics and scaling law for particles suspended in shear flow with inertia. *J. Fluid Mech.* 423, 317-344.
- FREEMAN, W. T. & ADELSON, E. H. 1991 The design and use of steerable filters. *IEEE T. Pattern Anal.* **13** (9), 891–906.
- GAVZE, E. & SHAPIRO, M. 1997 Particles in a shear flow near a solid wall: Effect of nonspherity on forces and velocities. *Int. J. Multiphase Flow* **23** (1), 155–182.
- Holm, R. & Söderberg, D. 2007 Shear influence on fibre orientation. *Rheol. Acta* 46, 721-729.
- HSU, R. & GANATOS, P. 1989 The motion of a rigid body in viscous fluid bounded by a plane wall. *J. Fluid Mech.* **207**, 29–72.
- HSU, R. & GANATOS, P. 1994 Gravitational and zero-drag motion of a spheroid adjacent to an inclined plane at low reynolds number. J. Fluid Mech. 268, 267– 292.
- Hyensjö, M., Dahlkild, A., Krochak, P., Olson, J. & Hämäläinen, J. 2007 Modelling the effect of shear flow on fibre orientation anisotropy in a planar contraction. *Nordic Pulp Paper Res. J.* **22** (3).
- JACOB, M. & UNSER, M. 2004 Design of steerable filters for feature detection using canny-like criteria. IEEE T. Pattern Anal. 26 (8), 1007–1019.

- Jeffery, G. B. 1922 The motion of ellipsoidal particles immersed in a viscous fluid. *Proc. Roy. Soc. London A* **102** (715), 161–179.
- Kerekes, R. J. & Schell, C. J. 1992 Characterization of fibre flocculation regimes by a crowding factor. J. Pulp and Paper Sci. 18 (1), J32–J38.
- Krushkal, E. M. & Gallily, I. 1988 On the orientation distribution function of non-spherical aerosol particles in a general shear flow II. The turbulent case. J. Aerosol Sci. 19 (2), 197–211.
- MORETTI, P. M. & KAYS, W. M. 1965 Heat transfer to a turbulent boundary layer with varying free-stream velocity and varying surface temperature an experimental study. *Int. J. Heat Mass Transfer* 8, 1187–1202.
- Moses, K. B., Advani, S. G. & Reinhardt, A. 2001 Investigation of fiber motion near solid boundaries in simple shear flow. *Rheol. Acta* 40, 296–306.
- NORDSTRÖM, B. 2003a Effects of headbox tube design and flow rate on formation and other sheet properties in twin-wire roll forming. *Nordic Pulp Paper Res. J.* 18 (3), 296–302.
- NORDSTRÖM, B. 2003b Effects of pulp type and headbox design on anisotropy and other sheet properties in twin-wire forming. Nordic Pulp Paper Res. J. 18 (3), 288–295.
- Olson, J. 1998 Analytic estimate of the fibre orientation distribution in a headbox flow. *Nordic Pulp Paper Res. J.* 17 (3), 302–306.
- Olson, J., Frigaard, I., Chan, C. & Hämäläinen, J. P. 2004 Modeling a turbulent fibre suspension flowing in a planar contraction: The one-dimensional headbox. *Int. J. Multiphase Flow* **30**, 51–66.
- Olson, J. & Kerekes, R. 1998 The motion of fibres in turbulent flow. J. Fluid Mech. 17, 47–64.
- Parsheh, M. 2001 Flow in contractions with application to headboxes. PhD thesis, Royal Institute of Technology, Stockholm, Sweden.
- Parsheh, M., Brown, M. L. & Aidun, C. K. 2005 On the orientation of stiff fibres suspended in turbulent flow in a planar contraction. *J. Fluid Mech.* **545**, 245–269.
- Parsheh, M., Brown, M. L. & Aidun, C. K. 2006a Investigation of closure approximations for fiber orientation distribution in contracting turbulent flow. *J. Non-Newtonian Fluid Mech.* **136**, 38–49.
- Parsheh, M., Brown, M. L. & Aidun, C. K. 2006b Variation of fiber orientation in turbulent flow inside a planar contraction with different shapes. *Int. J. Multiphase Flow* 32, 1354–1369.
- POZRIKIDIS, C. 2005 Orbiting motion of a freely suspended spheroid near a plane wall. J. Fluid Mech. **541**, 105–114.
- QI, D. & Luo, L. S. 2003 Rotational and orientational behaviour of threedimensional spheroidal particles in couette flows. J. Fluid Mech. 477, 201–213.
- ${\tt SCHLICHTING,\ H.\ 1979\ Boundary\ layer\ theory,\ 7th\ edn,\ 166-168.\ McGraw-Hill.}$
- Stover, C. A. & Cohen, C. 1990 The motion of rodlike particles in the pressure-driven flow between flat plates. *Rheol. Acta* **29**, 192–203.
- Subramanian, G. & Koch, D. L. 2005 Inertial effects on fibre motion in simple shear flow. *J. Fluid Mech.* **535**, 383–414.

- Sundararajakumar, R. R. & Koch, D. L. 1997 Structure and properties of sheared fiber suspensions with mechanical contacts. *J. Non-Newtonian Fluid Mech.* **73**, 205–239.
- Talamelli, A., Fornaciari, N., Westin, K. J. A. & Alfredsson, P. H. 2002 Experimental investigation of streaky structures in a relaminarizing boundary layer. *J. Turbulence* **3** (018).
- ULLMAR, M. 1998 On fibre alignment mechanisms in a headbox nozzle. Licentiate thesis, Royal Institute of Technology, Stockholm, Sweden.
- Warnack, D. & Fernholz, H. H. 1998 The effects of a favourable pressure gradient and of the reynolds number on an incompressible axisymmetric turbulent boundary layer. Part 2. The boundary layer with relaminarization. *J. Fluid Mech.* **359**, 357–381.

Evaluation of a steerable filter for detection of fibres in flowing suspensions

By Allan Carlsson † , Fredrik Lundell † & L. Daniel Söderberg † , ‡

[†]Linné Flow Centre, KTH Mechanics, SE - 100 44 Stockholm, Sweden [‡]STFI-Packforsk AB, SE - 114 86 Stockholm, Sweden

Steerable filters are concluded to be useful in order to determine the orientation of fibres captured in digital images. The fibre orientation is a key variable in the study of flowing fibre suspensions. Here digital image analysis based on a filter within the class of steerable filters is evaluated for suitability of finding the position and orientation of fibres suspended in flowing suspensions. In sharp images with small noise levels the steerable filter succeeds in determining the orientation of artificially generated fibres with well-defined angles. The influence of reduced image quality on the orientation has been quantified. The effect of unsharpness and noise is studied and the results show that the error in orientation is less than 1° for moderate levels. A set of images with fibres suspended in a shear flow is also analyzed. The fibre orientation distribution is determined in the flow-vorticity plane. In this analysis a comparison is also made to a robust, but computationally more expensive, method involving convolutions with an oriented elliptic filter. A good agreement is found when comparing the resulting fibre orientation distributions obtained with the two methods.

1. Introduction

Flowing fibre suspensions are found in a variety of applications such as fibre-reinforced composites processing and paper manufacturing. The final properties of the products of these applications are often strongly correlated to the fibre orientation. An example image from a flowing fibre suspension is shown in figure 1. In this specific image fibres are suspended in a shear flow over a solid wall and the image plane is parallel to the wall. From images like figure 1 quantities such as local fibre concentration and fibre velocities, both translational and rotational, could be of interest. To obtain these measures it is essential to be able to determine the position and orientation of individual fibres. It is usually preferred to extract this information by digital image analysis.



FIGURE 1. Fibres in a suspension flowing over a solid surface.

A reliable approach of finding the position and orientation of fibres captured in images is to use oriented filters (a short introduction to image filtering is given in section 2). A typical approach is to construct a filter with a shape that resembles the shape of the fibres and compute the convolution of the filter with the images containing fibres. A high value of the convolution at a certain position indicates that the image has a local resemblance with the filter at that position. To find the orientation of the fibres the filter is rotated to different orientations and a convolution is computed for each orientation. This course of action was for instance used by Holm & Söderberg (2007) to find the orientation of fibres in a shear flow. Although the method is reliable it can be expensive from a computational perspective since the angular resolution will be proportional to the number of convolutions performed. From a computational point of view Freeman & Adelson (1991) introduced a more efficient approach, for general feature detection, i.e. not restricted to fibres. The term steerable filter was introduced in order to describe a class of filters in which a filter of arbitrary orientation can be obtained from a linear combination of a limited amount of basis filters. This implies that, instead of computing several convolutions of a filter rotated to different orientations with an image, it is sufficient to compute the convolutions of the basis filters with the image. In this manner the orientation dependency is eliminated from the convolutions and thereby it is possible to cut down on the computational load and still have a good angular resolution.

A method for designing filters, within the class of steerable filters, for 2D feature detection, was proposed by Jacob & Unser (2004). Among others

a filter for ridge detection was designed. This filter was used by Carlsson, Lundell & Söderberg (2007) to find the orientation distribution of fibres in a shear flow. In the present study this ridge detector is evaluated. The ability to find the orientation of fibres as well as the sensitivity to noise and unsharpness is studied. This is done by capturing images of a picture containing printed fibres with well-defined orientations. The paper is finally concluded by a comparison of the method with a more traditional approach, using an elliptic filter, on a case where fibres have been suspended in a shear flow.

2. Image filtering for analysis of fibre images

The image filtering considered in this study will be based on the 2D convolution operator. The discrete convolution of an image f(m,n) with a filter matrix h(x,y) is given by

$$I(m,n) = f(m,n) * h(x,y) = \sum_{x=-\infty}^{\infty} \sum_{y=-\infty}^{\infty} f(m-x, n-y)h(x,y).$$
 (1)

As seen in equation (1) the convolution is given by a sum of products. The convolution I will also be referred to as the intensity throughout this text. The filter matrix can be regarded as a function that transforms the original image by giving some weight to the neighboring pixels for each pixel in the image. Note that the convolution is written as sums over infinite intervals. This can be done since the elements of h(x,y) are essentially zero apart from in a region in the centre of the matrix. However, in practice the sums are computed over finite intervals.

Image filtering can be used for various applications. There are for instance filters to make an image appear more sharp or blurry. There are also filters that emphasize specific features of an image, like for instance rod-like objects such as fibres. These are the kind of filters that are of interest for this study.

2.1. Elliptic Mexican hat for detection of fibres

The perhaps most obvious way to detect fibres in an image is to let h(x,y) in equation (1) resemble a fibre. This can be obtained by an elliptic "Mexican hat" here defined as

$$h(x,y) = \left(4\left[\left(\frac{x}{a\sqrt{2}}\right)^2 + \left(\frac{y}{b\sqrt{2}}\right)^2\right] - 2\right)e^{-\left(\left(\frac{x}{a\sqrt{2}}\right)^2 + \left(\frac{y}{b\sqrt{2}}\right)^2\right)},\tag{2}$$

where a and b are constants defining the shape of the filter. Putting h=0defines the ellipse $(x/a)^2 + (y/b)^2 = 1$. Thus, by letting 2a and 2b be equal to the fibre width and length, respectively, a filter suitable for detection of such fibres is generated. In figure 2 (a) the filter is shown for b/a = 10.

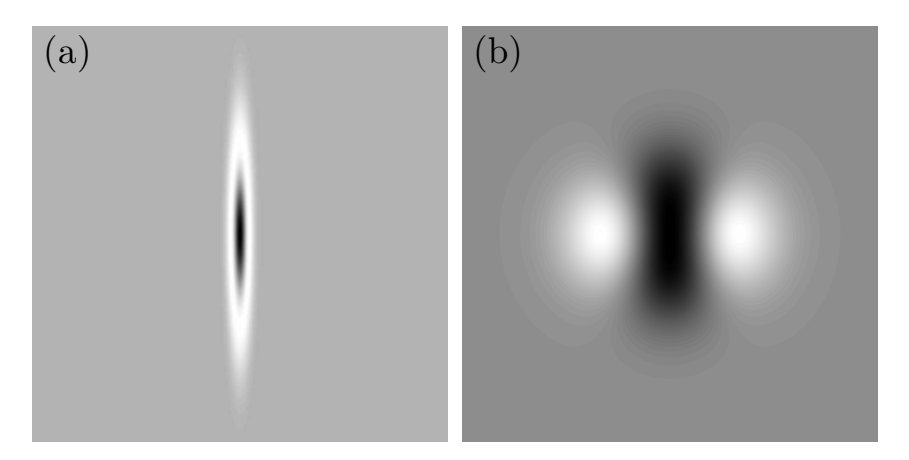


FIGURE 2. (a) The elliptic Mexican hat defined by equation (2) with b/a = 10 and (b) the steerable ridge detector defined by equation (7).

In order to rotate the filter to different orientations θ the rotation matrix \mathbf{R}_{θ} is used

$$\mathbf{R}_{\theta} = \begin{pmatrix} \cos \theta & \sin \theta \\ -\sin \theta & \cos \theta \end{pmatrix}. \tag{3}$$

The convolution of the image with the rotated version of the filter is then given by

$$I(m, n, \theta) = f(m, n) * h(\mathbf{R}_{\theta} \mathbf{x}), \tag{4}$$

where the vector $\mathbf{x} = (x, y)^T$. An elliptic Mexican hat was successfully used by Holm & Söderberg (2007) to determine the position and orientation of fibres. However, a limiting factor is that all the orientations, to be included in the analysis, have to be predefined and a convolution has to be computed for each orientation. This leads to that the method becomes computationally expensive if a good angular resolution is desired.

2.2. Steerable filter for detection of fibres

A way to avoid using predefined orientations of the filter and cut down on the computational load is to use a steerable filter. The class of steerable filters considered in this work can be expressed as

$$h(x,y) = \sum_{\kappa=1}^{M} \sum_{\lambda=0}^{\kappa} \alpha(\kappa,\lambda) \frac{\partial^{\kappa-\lambda}}{\partial x^{\kappa-\lambda}} \frac{\partial^{\lambda}}{\partial y^{\lambda}} g(x,y),$$
 (5)

where g is an arbitrary isotropic window function, *i.e.* a function independent of direction and approximately zero-valued outside some chosen interval. The

derivatives of g with respect to x and y, which are henceforth called $g_{\kappa,\lambda}$, are called basis filters and $\alpha(\kappa, \lambda)$ are constants defining the shape of the steerable filter. Since q is isotropic a rotated version of a steerable filter can be obtained from a linear combination of a limited set of basis filters. For a general $M_{\rm th}$ order detector M(M+3)/2 basis filters $g_{\kappa,\lambda}$, together with their constants $\alpha(\kappa,\lambda)$, are required to define a steerable filter.

The orientations at which the highest intensities will be found, from the convolution of a steerable filter with an image, at all positions in the image, can be obtained through the convolutions of the basis filters with the image. Choosing the window function to be a Gaussian, Jacob & Unser (2004) derived an optimal ridge detector for M=2, using the Dirac delta function to model the ridge. The Gaussian is defined as

$$g(x,y) = e^{-(x^2+y^2)}.$$
 (6)

The resulting steerable filter is shown in figure 2 (b) and is defined by

$$h(x,y) = \sqrt{\frac{3}{4\pi}} \left(\frac{\partial^2 g}{\partial x^2} - \frac{1}{3} \frac{\partial^2 g}{\partial y^2} \right). \tag{7}$$

It can be shown that the convolution of any rotated version of the steerable filter h(x,y), in equation (7), with the image f(m,n) can be written

$$I(m, n, \theta) = f(m, n) * h(\mathbf{R}_{\theta} \mathbf{x})$$

$$= \sqrt{\frac{3}{4\pi}} \left(f_{2,0} - \frac{1}{3} f_{2,2} \right) \cos^2 \theta + \sqrt{\frac{16}{3\pi}} f_{2,1} \cos \theta \sin \theta$$

$$+ \sqrt{\frac{3}{4\pi}} \left(f_{2,2} - \frac{1}{3} f_{2,0} \right) \sin^2 \theta, \tag{8}$$

where θ is the angle by which the filter is rotated and $f_{\kappa,\lambda}$ are the convolutions of the image with the basis filters given by

$$f_{\kappa,\lambda}(m,n) = f(m,n) * \left(\frac{\partial^{\kappa-\lambda}}{\partial x^{\kappa-\lambda}} \frac{\partial^{\lambda}}{\partial y^{\lambda}} g(x,y)\right).$$
 (9)

For each pixel (m, n) there is an orientation maximizing the intensity $I(m, n, \theta)$. This orientation can be found by solving $\partial I/\partial \theta = 0$ with I given by equation (8). The orientation θ that corresponds to the highest intensity is determined by putting both solutions into equation (8). As indicated by equation (8) only 3 convolutions $(f_{2,0}, f_{2,1})$ and $f_{2,2}$ have to be performed, for this specific steerable filter, in order to attain the intensity for all orientations of the filter. Consequently, as compared to the Mexican hat, where the number of convolutions is equal to the number of orientations, the computational load is reduced.

When used for fibre detection the size of the steerable filter is scaled by finding the two x-positions satisfying h(x, y = 0) = 0 and set the difference of the two x-positions to be equal to the fibre width. Note that, in contrast to the Mexican hat, the steerable filter is only scaled with the width and not the length of the fibres. As a result of only scaling with the width of the fibres the convolution of the filter with the image results in high intensities at several positions along the fibres. To determine the orientation of an individual fibre an averaging procedure has been imposed over all high intensity values that correspond to the fibre. A threshold value is introduced, defining how high the intensity has to be in order to belong to a fibre. Based on the orientation of the fibre at the position with the highest intensity a search algorithm is used to find other positions of high intensity which belong to the same fibre. The determined orientation θ_a of the fibre is given by the average of all the angles at the positions, belonging to the fibre, where the intensity exceeds the threshold. Also the intensity I_a of the fibre is given by the average of intensities belonging to these positions.

3. Measurement & analysis procedure

To evaluate if the steerable filter h(x,y) defined in equation (7), is capable to determine the orientation of fibres, two different experiments have been carried out. In the first experiment the filter is used in order to detect fibres, with predefined orientations, in an artificially generated image. In the other experiment fibres suspended in a viscous shear flow is studied. The data is analysed with the steerable filter and for comparison also with the Mexican hat, defined in equation (2).

3.1. Artificial fibres with predefined angles

A picture containing 91 artificial fibres was generated and printed on a top quality printer. The orientations of the artificial fibres are well defined and one degree apart. The orientations are $\theta_k = 0, 1, 2, ..., 90^{\circ}$, where θ_k is the angle taken clockwise from the vertical direction, *i.e.* $\theta_k = 0$ and 90° when a fibre is oriented in the vertical and horizontal direction, respectively.

A test image is acquired by taking photographs of the printout described above. In figure 3 the test image is shown for various degrees of sharpness and noise levels. A CCD-camera (Prosilica GE680) with a lens of focal length 50 mm (Fujinon HF50HA-1B) was used. The relative aperture was set as low as possible to N=2.3. The camera was placed at a distance from the picture of about 2.2 m to obtain sharp images with a width of the fibres w close to 2 pixels, similar to the width of the fibres in figure 1. The actual width of the fibres will depend on the precise distance between the picture and the camera. The steerable filter is scaled to the actual width of the artificial fibres. To generate a test image 100 images are captured and the average is calculated in order to reduce noise. The averaged amplitude of each fibre was also adjusted so that all fibres had the same amplitude. This was done to reduce effects due to light variations.

3.1a. Unsharp images. To investigate how sensitive the method is to unsharpness the test image was gradually traversed out of focus. For each distance, between the picture and the camera, a new set of 100 images was captured to perform the same procedure as explained above, for the original sharp test image. Two measurements (series A & B) were carried out. In serie A the picture was mainly located at distances farther away from the camera lens than the plane of focus and in serie B the picture was mainly closer than the plane of focus. Both series include a total of 24 different distances between the camera and the picture.

To quantify how sharp an image is the term circle of confusion will be introduced. Consider a point light source that is located at some distance from the camera. A fraction of the light rays, from the source, will hit the lens of the camera and ideally, due to the curvature of the lens, the rays will converge to a single point inside the camera. If the point source is located in the plane of focus this single point, inside the camera, will be on the sensor plane. If the point source is located farther away from the camera than the plane of focus the light will still converge to a single point in the camera, although in front of the sensor plane. At the sensor plane it will have diverged to a diffuse circle, generally referred to as the circle of confusion. A similar effect is found for a point source located closer to the camera than the plane of focus. However, in this case a circle of confusion is generated since the light has yet to converge when it reaches the sensor plane.

In this study the diameter d of the circle of confusion is used to characterize how sharp the test images are. By using trigonometric relations and the thin lens formula, see for instance Meyer-Arendt (1995), it is possible to derive an analytical expression for d given by

$$d_j = \frac{F^2 (s_j - s_0)}{N s_j (s_0 - F)},\tag{10}$$

where F is the focal length of the lens and N = F/D is the relative aperture with the entrance pupil diameter given by D. Furthermore, s_0 and s_i is the distance from the lens to the plane of focus and to the picture, respectively. The significance of d should be coupled to how large it is in comparison to the fibre width w. Therefore d is normalized with w in the analysis.

3.1b. Images with noise. The method has also been evaluated for its sensitivity to noise. This was done by adding noise to the images. If the original test image is denoted by f'(m,n) the resulting image f(m,n) is given by the relation

$$f(m,n) = f'(m,n) + \eta(m,n),$$
 (11)

where $\eta(m,n)$ is the noise. A random zero-mean Gaussian distribution has been used to model the noise, i.e. the probability density function of the added

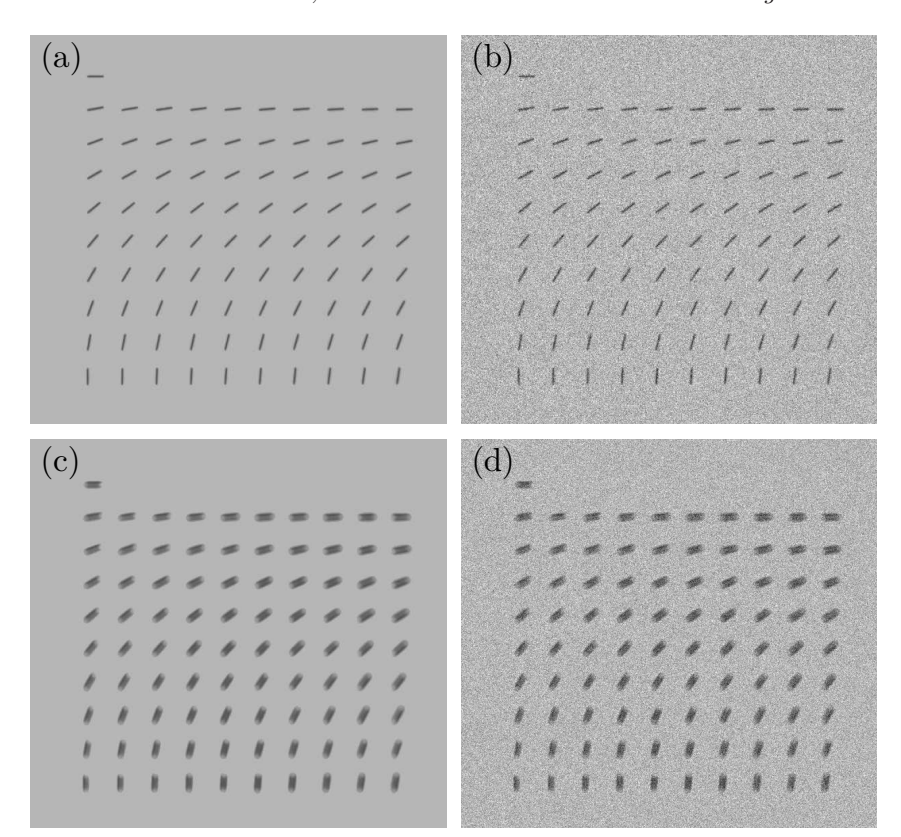


FIGURE 3. Test image with different noise levels and degrees of sharpness: (a) $\sigma_s=0$ and d/w=0, (b) $\sigma_s=1/4$ and d/w=0, (c) $\sigma_s=0$ and d/w=-0.15 and (d) $\sigma_s=1/4$ and d/w=-0.15.

noise amplitude is given by

$$P(\eta) = \frac{1}{\sigma\sqrt{2\pi}}e^{\left(-\frac{\eta^2}{2\sigma^2}\right)}.$$
 (12)

The generated noise is uncorrelated over the image. The variable σ_s quantifies the noise level and is defined as the standard deviation σ of the Gaussian noise, normalized with the difference in amplitude between the fibres and its surroundings. A total of 500 images were generated for each noise level under study and analyzed with the steerable filter algorithm.

3.2. Fibres suspended in a shear flow

A fibre suspension with black-dyed cellulose acetate fibres with a length to diameter ratio of $r_p = 10$, suspended in a viscous shear layer, has been studied experimentally, see Carlsson, Lundell & Söderberg (2007) for details. The fibre suspension, driven by gravity, was flowing down a slightly inclined plane to generate the shear layer. To visualize the fibres a CCD-camera (SONY DFW-X700) was mounted to capture images in a plane parallel to the solid wall. In the present study 100 statistically independent images is analyzed, using two different feature detection algorithms. The fibre orientation distribution is calculated with the Mexican hat and the steerable filter, defined in the previous section.

4. Results & Discussion

The steerable filter described in section 2 is evaluated to find the artificially generated fibres shown in figure 3 and the sensitivity to unsharpness and noise is quantified. Furthermore the method is compared to a robust, but more time consuming, method by analyzing measurements performed on a flowing fibre suspension.

4.1. Artificial fibres with predefined angles

In figure 4 results from analyzing the test image, with $\sigma_s = 0$ and d/w = 0, for series A and B are shown. In (a) the angular deviation $\theta_d = \theta_a - \theta_k$ is presented. Again, θ_a is the determined angle of a fibre and θ_k is the predefined angle in the test image of the corresponding fibre. In 4 (b) the intensity, normalized with the maximum value among the fibres, I_a is shown as a function of θ_k . The solid and dashed line represents the results from series A and B, respectively. The steerable filter detects all of the fibres with a maximum angular deviation less than 1 degree. In figure 4 (b) it is seen that the intensity fluctuations are moderate. The difference between the maximum and minimum intensity differs with less than 10%. There seem to be a periodicity of I_a in θ_k of about 10 degrees. This is most likely a remaining effect of light variations due to the fact that there are 10 fibres in each row of the test image. Since the light settings are similar in series A and B there is a correlation between the intensities found in these measurements. Going back to figure 4 (a) it is noted there is no strong correlation between the results of series A and B indicating that there are no preferred orientations of the steerable filter.

4.1a. Sensitivity to noise and unsharpness. In figure 5 (a) the probability density function (PDF) of θ_d is shown for various σ_s with d/w = 0 and in (b) the corresponding standard deviation Σ , skewness Λ and excess kurtosis Γ defined

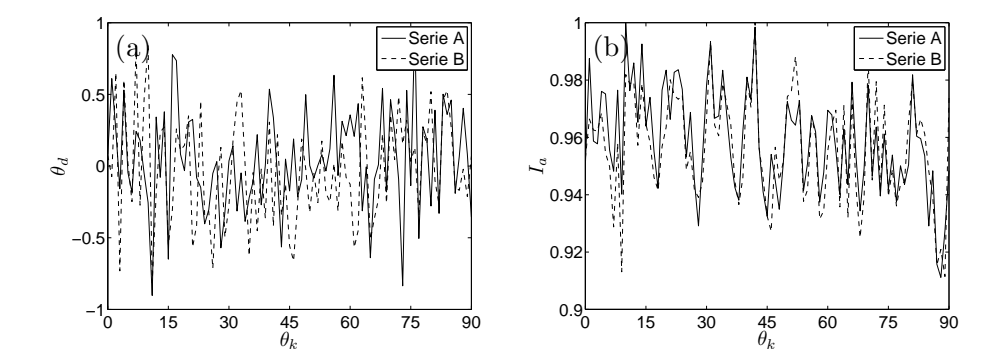


FIGURE 4. (a) The angular deviation θ_d as a function of θ_k for $\sigma_s = 0$ and d/w = 0, (b) The intensity variation I_a with θ_k for $\sigma_s = 0$ and d/w = 0. In both (a) and (b) the solid and dashed line corresponds to results from series A and B, respectively.

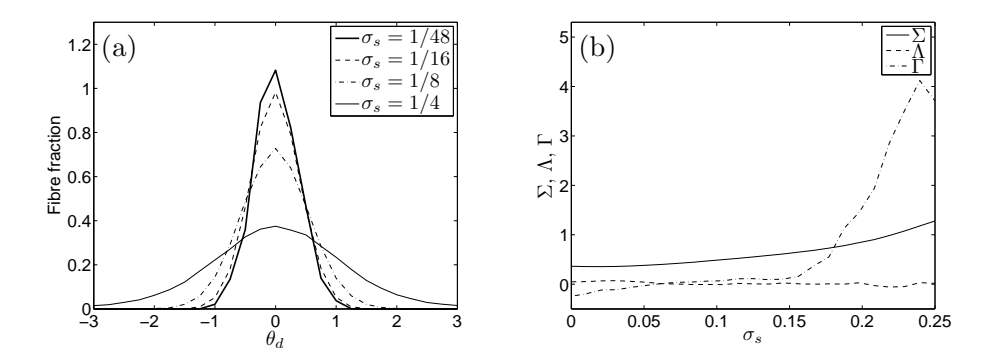
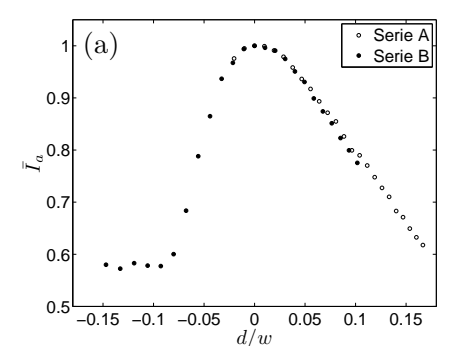


FIGURE 5. The fraction of fibres detected at different angular deviations θ_d for various σ_s in (a) and Σ , Λ and Γ as a function of σ_s in (b). In both (a) and (b) d/w = 0 (sharp images).

by

$$\Sigma = \sqrt{\frac{1}{X_k X_i} \sum_{k=1}^{X_k} \sum_{i=1}^{X_i} \left[\theta_d(k, i) - \bar{\theta}_d \right]^2},$$
(13)

$$\Lambda = \frac{1}{X_k X_i \Sigma^3} \sum_{k=1}^{X_k} \sum_{i=1}^{X_i} \left[\theta_d(k, i) - \bar{\theta}_d \right]^3, \tag{14}$$



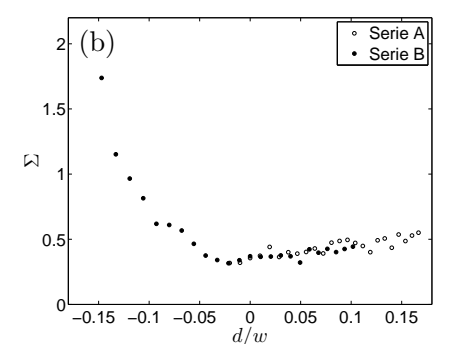


FIGURE 6. (a) The normalized mean intensity \bar{I}_a and (b) the standard deviation Σ for different degrees of sharpness d/w. In both (a) and (b) $\sigma_s = 0$.

$$\Gamma = \frac{1}{X_k X_i \Sigma^4} \sum_{k=1}^{X_k} \sum_{i=1}^{X_i} \left[\theta_d(k, i) - \bar{\theta}_d \right]^4 - 3 \tag{15}$$

are shown as a function of σ_s . In equations (13), (14) and (15) the number of fibres per image is $X_k = 91$ and the number of images is $X_i = 1$ and 500 for $\sigma_s = 0$ and $\sigma_s \neq 0$, respectively. Furthermore, $\theta_d(k,i)$ denotes the computed angular deviation of fibre k in image i and $\bar{\theta}_d$ is the angular deviation averaged over both the X_k fibres and the X_i images. When $\sigma_s = 0$ the mean angular deviation $\bar{\theta}_d = 0.04$ and -0.03° for series A and B, respectively. This could be due to a small angular offset imposed when capturing the test images or due to that 91 fibres are not sufficient to ensure a convergence to $\theta_d = 0$. Since the results from series A and B are similar, the results in figure 5 are based on data from both series. It is seen, in figure 5, that the PDF of θ_d is symmetrical around $\theta_d = 0$, which is also verified by Λ being close to zero for all σ_s . For small σ_s , Σ grows slowly with σ_s and remains below one degree for σ_s less than about 0.2. The growth of Σ is however increasing with σ_s and is larger than one degree for the higher σ_s under study. For $\sigma_s < 0.15$ the excess kurtosis Γ is close to zero. A more rapid increase of Γ is found for higher σ_s as the PDF

In figure 6 (a) the mean intensity \bar{I}_a is shown for various degrees of sharpness. In these results $\sigma_s = 0$. The intensity has been averaged over all X_k fibres and normalized to be equal to one at d=0. The intensity has also been used to determine the position of the plane of focus, i.e. the curves have been translated to have a maximum intensity at d=0. It is noted that the results are not symmetric around d/w=0. This is most likely due to the pixelization of the filter, i.e. when the filter is transformed from a continuous to a discrete form in order to compute the convolutions numerically. Recall that the fibre

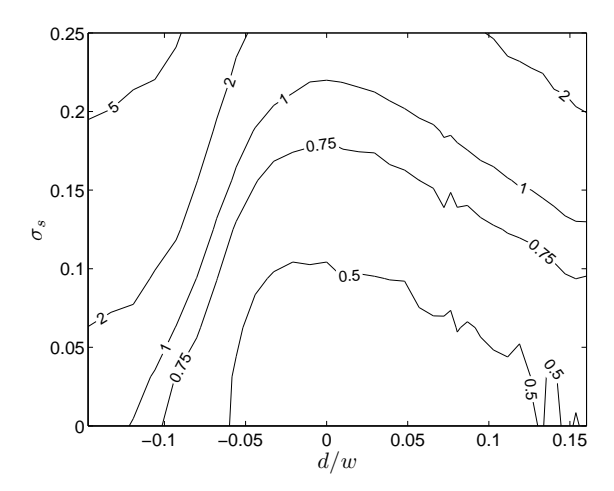


FIGURE 7. Contours showing Σ , the standard deviation of θ_d , for different degrees of sharpness and noise levels.

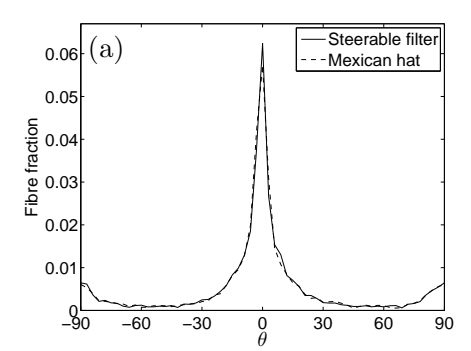
width is a function of the distance between the image and the camera lens. For the studied degrees of sharpness the fibre width w ranges from about 1.6 to 2.4 in pixels. It is possible that the number of points to describe the filter are too few for d/w = -0.15, where $w \approx 1.6$ pixels, in order to get accurate results. This could result in the more rapid decrease of \bar{I}_a , seen in figure 6 (a), for negative values of d/w.

In figure 6 (b) the standard deviation of θ_d , given by equation (13) with $\sigma_s = 0$, *i.e.* $X_k = 91$ and $X_i = 1$, is shown. The deviation only exceeds one degree for d/w less than approximately -0.13.

In figure 7 the standard deviation of the angular deviation Σ is shown in a region where noise has been added to images which are out of focus. The standard deviation is larger than one degree in parts of the studied region, where the generated image is out of focus and the added noise is large. However, in a relatively large fraction of the studied region Σ is less than one degree.

4.2. Fibres suspended in a shear flow

The measurements performed on a sheared fibre suspension were analyzed with the steerable filter in equation (7) and the Mexican hat in equation (2). The pixel width and length of sharp fibres, contained in the images, was approximately 2 and 20 pixels, respectively. The noise level of the captured images was $\sigma_s \approx 0.05$. The angular resolution of the Mexican hat was chosen to be one degree, *i.e.* the filter was rotated to $\theta_a = 0, 1, 2, ..., 179^{\circ}$ and the convolution with the images was computed for each angle.



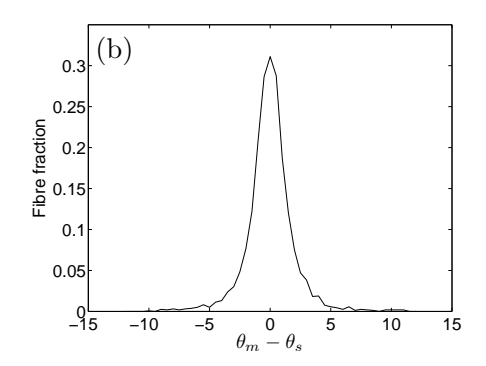


FIGURE 8. (a) Fibre orientation distribution based on analysis with a steerable filter (solid line) and with an elliptic Mexican hat (dashed line), (b) the distribution of the angular difference $\theta_m - \theta_s$, where θ_m and θ_s are the orientations obtained by the Mexican hat and the steerable filter, respectively.

The fibre orientation θ is analyzed in a plane parallel to a wall and is defined to be zero in the flow direction. The number of detected fibres, by the two different filters, depends on arbitrarily predefined threshold values of intensity and will generally not be the same. The thresholds are adjusted so that the same number of fibres is found in each image.

In figure 8 (a) a total of 6644 detected fibres is collected into bins with a range of 3 degrees and are presented as a function of the fibre orientation θ . Approximately the same orientation distribution is obtained with both methods. In figure 8 (b) a distribution of the angular difference of individual fibres are shown. For most fibres the orientation, determined with the different methods, is almost the same, but occasionally the angular difference is as much as 5 degrees. The experimental measurements and results are discussed in detail by Carlsson et al. (2007). For this study it is concluded that there is a good agreement between the two different algorithms and that steerable filters is an efficient method to detect and determine the orientation of fibres in flowing suspensions.

5. Conclusions

A ridge detector within the class of steerable filters has been shown to be an accurate and computationally efficient method of locating and determining the orientation of fibres suspended in flowing suspensions. In an image containing 91 artificially generated sharp fibres the orientation of the fibres was determined, with a standard angular deviation Σ well below one degree. A zero-mean Gaussian noise was added to the image. The standard deviation remained below one degree for $\sigma_s < 0.2$, whereas a more rapid increase of Σ was seen for larger σ_s . The method was also evaluated for sensitivity to unsharpness. Also here Σ was smaller than one degree for reasonable levels.

The steerable filter was compared to an oriented elliptic Mexican hat on a set of data from measurements on fibres suspended in a shear flow. Approximately the same orientation distribution was obtained with both methods and for the majority of fibres the angular difference was small, also for individual fibres. It is noted that to obtain these results the number of convolutions per image were 3 and 180 for the steerable filter and the Mexican hat, respectively. Thus, compared to the Mexican hat, the steerable filter is a very time efficient method.

Another feature of the steerable filter, which could be of use, is that it is only scaled with the width of the fibres. The angle θ is given for all positions along the fibres and in principle this makes it possible to determine the curvature of deformed fibres.

References

- Carlsson, A., Lundell, F. & Söderberg, L. D. 2007 Fiber orientation control related to papermaking. *J. Fluids Eng.* **129** (4), 457–465.
- FREEMAN, W. T. & ADELSON, E. H. 1991 The design and use of steerable filters. $IEEE\ T.\ Pattern\ Anal.\ 13\ (9),\ 891–906.$
- HOLM, R. & SÖDERBERG, D. 2007 Shear influence on fibre orientation. Rheol. Acta ${\bf 46}, 721-729.$
- Jacob, M. & Unser, M. 2004 Design of steerable filters for feature detection using Canny-like criteria. $IEEE\ T.\ Pattern\ Anal.\ 26\ (8),\ 1007-1019.$
- MEYER-ARENDT, J. R. 1995 Introduction to classical and modern optics., 4th edn. Prentice-Hall.